ABSTRACT

MUN, SUNGHO. Nonlinear Finite Element Analysis of Pavements and Its Application to Performance Evaluation. (Under the direction of Dr. Y. Richard Kim and Dr. Murthy N. Guddati.)

This research documents the findings from the study of failure mechanisms of fatigue cracking in asphalt pavements using the finite element program that employs the viscoelastic continuum damage model for asphalt layer and a nonlinear elastic model for unbound layers. Both bottom-up and top-down cracks are investigated by taking several important variables into account, such as asphalt layer thickness, layer stiffnesses, pressure distribution under loading, and load levels applied on the pavement surface. The crack initiations in different pavement structures under different loading conditions are studied by monitoring a damage contour. The developed finite element code, called VECD-FEP++, employs the viscoelastic continuum damage model as the constitutive model of asphalt concrete and the universal model (or so-called Uzan-Witczak resilient modulus model) for unbound materials. The finite element analysis of various pavement-load combinations showed significantly different failure mechanisms. Details on the VECD-FEP++ and the findings are given in the following chapters.

NONLINEAR FINITE ELEMENT ANALYSIS OF PAVEMENTS AND ITS APPLICATION TO PERFORMANCE EVALUATION

by

SUNGHO MUN

A dissertation submitted to the Graduate Faculty of
North Carolina State University
in partial fulfillment of the
requirements for the Degree of
Doctor of Philosophy

DEPARTMENT OF CIVIL ENGINEERING

Raleigh

2003

APPROVED BY:

Y. Richard Kim
(Chair of Advisory Committee)

Murthy N. Guddati
(Co-chair of Advisory Committee)

Tasnim Hassan

Mansoor Haider

BIOGRAPHY

Sungho Mun was born on December 23, 1968 in Busan, South Korea. He has two younger brothers. He received his Bachelor of Science degree in civil engineering at Myong Ji University in 1995. He joined Korea Land Corporation on January 4, 1995 as an assistant or project manger for nearly four years. He participated in several projects, including Korea-Russia Industrial Complex Construction and Milrock and Songan Land Development in Kyung-Gi Province. He was admitted to North Carolina State University for graduate study in August, 1998 and he received Mater of Science in Civil Engineering. In December 2000, he continuously stayed for his study at the Department of Civil, Construction, and Environmental Engineering of North Carolina State University.

ACKNOWLEDGMENTS

I owe an immeasurable debt to many individuals who contributed greatly to completing this dissertation. This research reported in this dissertation has been carried out at the Department of Civil, Construction, and Environmental Engineering of North Carolina State University.

My sincere thanks and gratitude go to my supervisor, Professor Y. Richard Kim, for his invaluable guidance, support, and interest in the research throughout my study. I also wish to express deep appreciation to my co-advisor, Dr. Murthy N. Guddati, for his guidance and help on my numerical work of finite element analysis and encouragement over the courses of my studies. I am grateful to Dr. Mansoor Haider for his advice and lecture on boundary integral analysis as well as on fast multipole methods, and to Dr. Tasnim Hassan for serving on my advisory committee and his sincere interest in my research. Great appreciation goes to Professor Roy H. Borden for his advice and concerns related to the behavior of inelastic soils as well as for his spiritual relationship, sharing his experience of God's love. Special thanks are also given to Dr. Ghassan R. Chehab for his experimental data used for the evaluation of this study.

Finally, I would like to thank God for his love and guidance, my wife, Minjeong, daughter, Irene, and parents for their love, support and understanding.

TABLE OF CONTENTS

LIST OF TABLES

LIST OF FIGURES

CHAPTER 1

INTRODUCTION

Fatigue cracking is one of the major distresses affecting the performance of asphalt pavements. Fatigue cracks can initiate at the bottom of the asphalt concrete layer due to tensile stresses developed because of flexure and propagate to the pavement surface under repeated load applications. Recent research also suggests that fatigue cracks can also initiate at the pavement surface due to tensile stresses resulting from the interaction between truck tires and the pavement surface. These fatigue cracks propagate through the asphalt concrete layer under repetitive loading. The tensile stress-strain behavior of the material appears to be the major factor of material characterization that needs to be understood to address both bottom-up and top-down fatigue cracking (Daniel and Kim 2002).

There has been a considerable amount of research in developing, verifying, and calibrating fatigue performance models. Historically, much of the work in this area has been empirical in nature. Most of these models relate asphalt mixture properties and responses measured from a representative volume element (RVE) to the number of cycles to failure. Due to their empirical nature, these models require a large amount of laboratory testing to cover the wide range of conditions encountered in the field.

A more fundamental approach to the prediction of fatigue damage growth in asphalt pavements is two-fold. First, material constitutive models need to be developed. These models should be able to describe stress-strain behavior of layer materials in pavement structures under realistic loading and environmental conditions. Well-

established theories in the discipline of material mechanics are available for this task. The second step is to incorporate the material constitutive models into a structural model that computes stresses and strains in pavement structures. This structural model accounts for the effects of boundary conditions (such as layer thicknesses, pavement edges, bedrock, etc.) for the pavement in question.

As discussed by Huang (1993), the classical approach to fatigue cracking performance prediction employs the relationship between the allowable number of load repetitions and the tensile strain at the bottom of the asphalt layer. However, Myers et al. (2001) showed the traditional bottom-up crack of the cumulative damage concept fails to predict the damage due to longitudinal surface cracking found in the field. They used the linear elastic model for all the layers in pavement structures and incorporated fracture mechanics into a finite element analysis to evaluate top-down cracking mechanisms. For more realistic modeling however, the viscoelastic nature of asphalt concrete needs to be accounted for in the analysis. Additionally, many researchers have found that the nonlinear elastic behavior of base and subgrade materials is important in accurately estimating stresses and strains in pavements.

The principal objective of this study is to study the fatigue cracking mechanisms of asphalt pavements by evaluating stress and damage contours determined from a finite element analysis that employs a viscoelastic continuum damage model for asphalt layer and a stress-state dependent nonlinear elastic model for aggregate base and subgrade. Effects of various pavement and load factors on the cracking mechanisms are also investigated using the same approach. Findings from this parametric study are expected

to shed some light on identifying conditions that are more susceptible to either bottom-up cracking or top-down cracking.

Chapter 2 describes the research effort made to implement the viscoelastic continuum damage model into VECD-FEP++ on the foundation of FEP++ developed by Guddati (2001). Methods of conversion among the linear viscoelastic functions and numerical formulations for the implementation of the convolution integral are discussed. Results from constant-crosshead-rate monotonic tests in tension at varying temperatures and strain rates are used to verify the resulting finite element program. In Chapter 3, the stress-state dependent nonlinear elastic model is included in the framework of VECD-FEP++. The developed methodology was verified by comparing the results from VECD-FEP++ with an analytical solution in a simple boundary condition and with the results from laboratory resilient modulus tests of granular materials and fine-grained soils. In Chapter 4, the finite element (FE) mesh discretization technique is treated in detail for the analysis of multilayered pavement structures. Chapter 5 describes the investigation of the fatigue failure modes by monitoring the stress and damage contours computed from VECD-FEP++ with the viscoelastic continuum damage model and the nonlinear elastic model. This chapter also presents findings from the parametric study in which the effects of asphalt layer thickness, base/subgrade moduli, contact pressure distribution, and load level are evaluated systematically. Finally, a summary of findings and recommendations for future research are given in Chapter 6.

CHAPTER 2

MODELING OF ASPHALT LAYER IN PAVEMENT STRUCTURE

Top layer in a flexible pavement structure is made of asphalt concrete that is viscoelastic and undergoes damage under repeated loadings. In this chapter, the asphalt layer is modeled using a viscoelastic continuum damage (VECD) model embedded into finite element (FE) discretization. This is performed using the following steps:

1) Obtaining the linear viscoelastic properties from experimental data (Section 2.1).
2) Incorporation of viscoelastic material properties into FE methods (Section 2.2).
3) Expansion of the material model to include damage and its implementation into FE framework (Section 2.3).

2.1 LINEAR VISCOELASTIC MATERIAL MODELING

Linear viscoelastic material property of asphalt concrete is represented by a generalized Maxwell model, which can be viewed as a Prony series expansion of the relaxation modulus. The Prony series coefficients are estimated from the experimental data using the following material modeling procedure:

1) Obtain complex moduli as a function of loading frequency using a frequency sweep test and smoothening experimental data.
2) Convert the frequency domain data into time domain data (Prony series representation) with the positive sign control of the Prony series coefficients.

In this section, this methodology is explained based on the above steps.

2.1.1 Techniques for Obtaining Material Properties

Frequency Sweep Test

The frequency sweep test (FST) is performed by applying a sinusoidal load to an asphalt concrete specimen to obtain the linear viscoelastic material properties of asphalt mixtures. The loading amplitude is adjusted based on the material stiffness, temperature, and frequency to keep the strain response within the linear viscoelastic range. Typically, a micro-strain level of 50 to 75 is targeted as the limit for the linear viscoelasticity. The loading is applied until steady-state response is achieved, at which point several cycles of data are collected. After each frequency, a five-minute rest period is allowed for specimen recovery before the next loading block is applied. The frequencies are applied from the fastest to the slowest ranging from 1 to 20 Hz.

From the FST, the complex modulus, E^*, which includes the dynamic modulus ($|E^*|$) and the phase angle (ϕ), can be determined. The complex modulus can also be viewed as a composition of storage (E') and loss moduli (E'') as follows:

$$E^* = E' + iE'' \tag{2.1}$$

where i is the $\sqrt{-1}$. The dynamic modulus is the amplitude of the complex modulus and is defined as:

$$|E^*| = \sqrt{(E')^2 + (E'')^2}\ . \tag{2.2}$$

The values of the storage and loss moduli, which are shown in Fig. 2.1, are related to the dynamic modulus and phase angle as follows:

$$E' = |E^*| \cos\phi \ \text{ and } \ E'' = |E^*| \sin\phi\ . \tag{2.3}$$

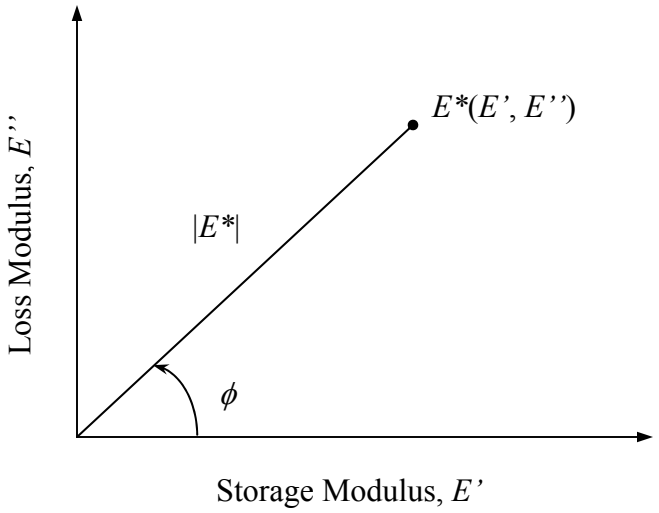

Figure 2.1 Complex Modulus Schematic Diagram

As the material becomes more viscous, the phase angle increases and the loss component of the complex modulus increases. Conversely, a decreasing phase angle indicates more elastic behavior and a larger contribution from the storage modulus. The dynamic modulus at each frequency is calculated by dividing the steady state stress amplitude, σ_{amp}, by the strain amplitude, ε_{amp}:

$$|E^*| = \frac{\sigma_{amp}}{\varepsilon_{amp}}. \tag{2.4}$$

The phase angle, ϕ, is associated with the time lag, Δt, between the strain input and stress response at the corresponding frequency, f:

$$\phi = 2\pi f \Delta t. \tag{2.5}$$

As the testing temperature decreases or the loading rate increases, the dynamic modulus will increase and the phase angle will decrease indicating decreased history dependence or the viscoelasticity of the material.

Fitting Data to Log-Sigmoid Function

The storage modulus, $E'(\omega)$, can be obtained from Eq. (2.3) where ω represents a reduced frequency at a given temperature. Fitting this data to a log-sigmoid function is used to smoothen and average the oscillating data. The following equation, $f(\omega)$, is defined as the log-sigmoid function:

$$f(\omega) = a_1 + \frac{a_2}{\left\{ a_3 + \frac{a_4}{\exp\left[a_5 + a_6 \log_{10}(\omega)\right]} \right\}} \tag{2.6}$$

where $a_{1,2,\ldots,6}$ are the coefficients determined by the iterative Levenberg-Marquardt algorithm (Fletcher, 1987), which minimizes the error in the approximation.

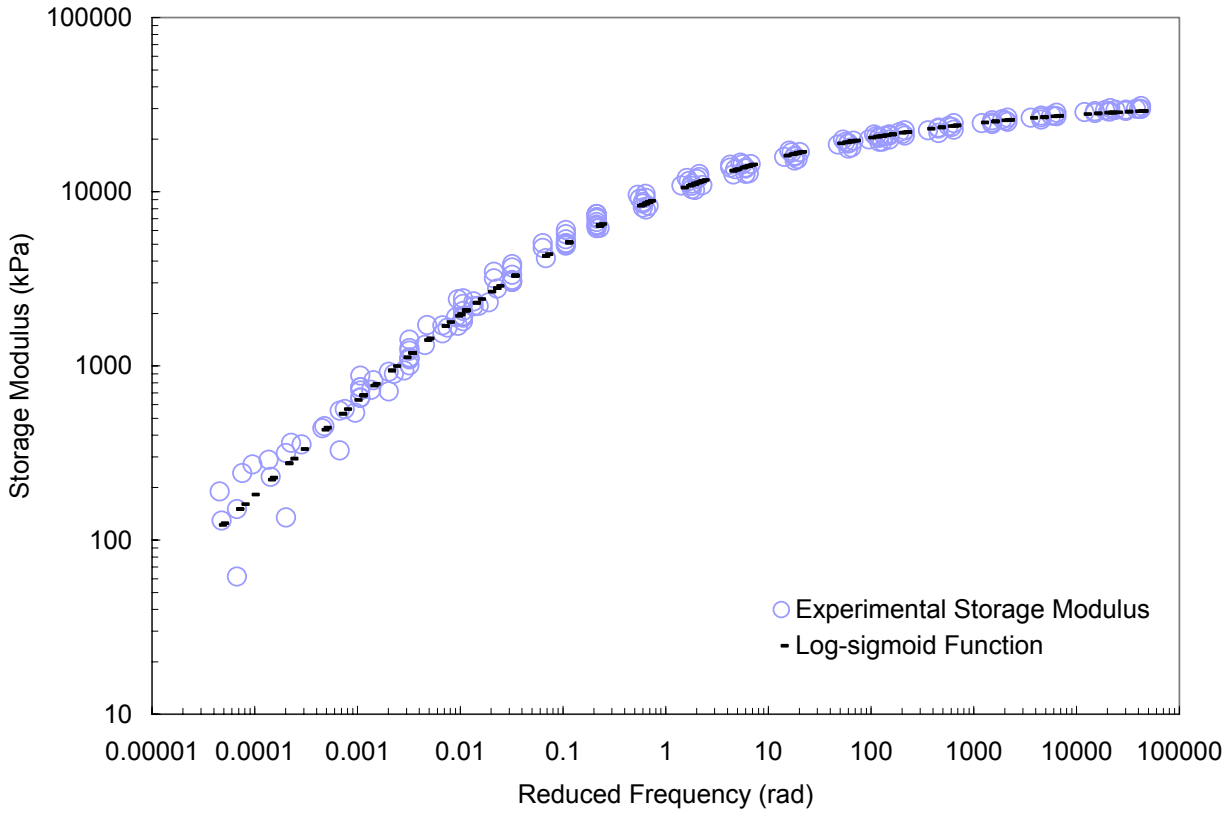

Figure 2.2 Fitting Experimental Data to Log-sigmoid Function

The Levenberg-Marquardt optimization is performed using the nonlinear-least-squares program in MATLAB. To obtain the best fit, the initial values of coefficients defined by Eq. (2.6) are iteratively changed until the log-sigmoid curve satisfactorily represents the experimental storage data shown in Fig. 2.2. The smoothened storage moduli, fitted with the log-sigmoid function, are used for the following interconversion between frequency-domain modulus and time-domain (relaxation) modulus.

Frequency Domain Modulus to Time Domain (Relaxation) Modulus

The interconversion of linear viscoelastic material functions between frequency-domain and time-domain relaxation can be performed through either an approximate method or an exact method. Schapery and Park (1999) proposed the following approximate analytical method, which is given by:

$$E(t) \cong \frac{1}{\lambda'} E'(\omega)\,|_{\omega=(1/t)} \tag{2.7}$$

where ω, t, $E'(\omega)$, and $E(t)$ are reduced frequency, reduced time, storage modulus, and relaxation modulus at a reference temperature respectively. The adjustment function, λ', is defined as follows:

$$\lambda' = \Gamma(1-n)\cos(n\pi/2) \tag{2.8}$$

where Γ is a gamma function and n is the local log-log slope of the storage modulus given by:

$$n = \frac{d\log E'(\omega)}{d\log \omega}\,. \tag{2.9}$$

The time-domain modulus can be used to determine the Prony series shown as:

$$E(t) = E_\infty + \sum_{m=1}^{M} E_m \exp(-t/\rho_m) \tag{2.10}$$

where E_∞, ρ_m, and E_m are infinite relaxation modulus, relaxation time, and Prony coefficients respectively. E_∞ can be determined by $E'(\omega)|_{\omega->0^+}$ using a very small non-negative value of frequency. It is assumed that the collocation points of time (t) and ρ_m are separated by decades (Schapery, 1961). Eq. (2.10) can then be viewed in the following matrix form:

$$\underbrace{E(t_n) - E_\infty}_{\{A\}} = \underbrace{\sum_{m=1}^{M} \exp(-t_n/\rho_m)}_{[B]} \underbrace{E_m}_{\{C\}}, \; n=1,\ldots,N. \tag{2.11}$$

Note that the vector **{C}** is subjected to an additional constraint $E_m > 0$. This constraint converts the parameter estimation problem into the following linear programming problem:

$$\text{MINIMIZE } |\mathbf{[B]\{C\}-\{A\}}| \qquad \text{SUCH THAT } \mathbf{\{C\}} > 0. \tag{2.12}$$

The above problem is solved by MATLAB.

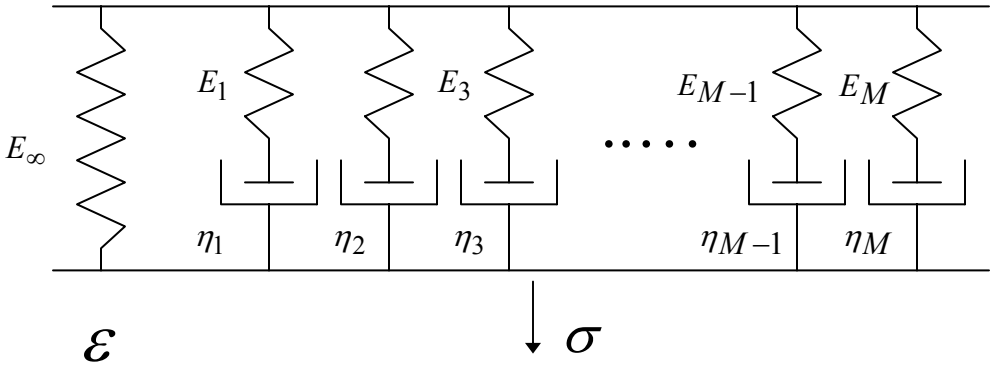

Figure 2.3 Wiechert Model (or Generalized Maxwell Model)

An alternative to the above approximate method is an "exact" method outlined below. The interconversion between frequency-domain and time-domain material properties can be solved based on the following relations. As shown in Fig. 2.3, from a given strain, ε, the stress in the left spring, σ_∞, is:

$$\sigma_\infty = E_\infty \varepsilon \,. \tag{2.13}$$

The stress, σ_m, in each of the Maxwell components combining a spring with a dashpot is governed by the differential equation:

$$\frac{d\varepsilon}{dt} = \frac{1}{E_m}\frac{d\sigma_m}{dt} + \frac{\sigma_m}{\eta_m} \tag{2.14}$$

where η_m is the coefficient of viscosity, and E_m is the relaxation modulus in the m^{th} term or Prony coefficient. Due to the linearity of the material components, the total stress on the Wiechert model is obtained by the following summation form:

$$\sigma = \sigma_\infty + \sum_{m=1}^{M} \sigma_m \,. \tag{2.15}$$

Fourier transformation converts the differential equation into the following algebraic equation:

$$\breve{\sigma} = \left(E_\infty + \sum_{m=1}^{M} \frac{i\omega_n \rho_m E_m}{i\omega_n \rho_m + 1} \right) \breve{\varepsilon} \,, \; n=1,\ldots,N \tag{2.16}$$

where $\breve{\sigma}$ and $\breve{\varepsilon}$ are Fourier-transforms of stress and strain respectively, and the relaxation time of the m^{th} Maxwell element is as follows:

$$\rho_m \equiv \frac{\eta_m}{E_m} \,. \tag{2.17}$$

Therefore, the complex modulus can be obtained from the constitutive equation shown in Eq. (2.16) as follows:

$$E^* = E_\infty + \sum_{m=1}^{M} \frac{i\omega_n \rho_m E_m}{i\omega_n \rho_m + 1},\ n=1,\ldots,N. \tag{2.18}$$

The storage modulus is obtained by taking the real part of the complex modulus:

$$E'(\omega_n) = E_\infty + \sum_{m=1}^{M} \frac{\omega_n{}^2 \rho_m^2 E_m}{\omega_n{}^2 \rho_m^2 + 1},\ n=1,\ldots,N. \tag{2.19}$$

The parameters E_∞, ρ_∞, and E_m are obtained by fitting the above expression with the experimental storage modulus. E_∞ can be found by $E'(\omega)|_{\omega->0^+}$. E_m can be obtained based on matching the log-sigmoid function-fitted data with analytical expression in Eq. (2.19) at discrete values of frequency ω_n.

$$\mathbf{\{D\} = [E]\{F\}} \tag{2.20}$$

where the column vectors, **{F}** and **{D}**, are E_m and $E'(\omega_n)$- E_∞ respectively; the matrix, **[E]**, is as follows:

$$E_{n,m} = \sum_{m=1}^{M} \frac{\omega_n{}^2 \rho_m^2}{\omega_n{}^2 \rho_m^2 + 1},\ n=1,\ldots,N. \tag{2.21}$$

However, the solution of Eq. (2.20) does not guarantee the positive coefficients of E_m. Obtaining the positive coefficients of E_m can be done by introducing the constraints that force them to be non-negative and minimizing the error of the fit. The problem is then the linear programming problem, which is solved by MATLAB.

$$\text{MINIMIZE } |\mathbf{[E]\{F\}-\{D\}}| \qquad \text{SUCH THAT } \mathbf{\{F\}} > 0. \tag{2.22}$$

2.1.2 Evaluation of Material Property Estimation Techniques

The above-described methods are tested using experimental data. The possible combinations of experimental data and conversion methods are provided in Table 2.1.

Table 2.1 Five Sets Chosen in This Study

Combination	Dynamic Modulus	Phase Angle	Conversion Method
1	Raw	Raw	Exact
2	Average	Adjusted	Exact
3	Average	Average	Exact
4	Average	Adjusted	Approximate
5	Average	Average	Approximate

The experimental dynamic moduli can be chosen by using them as they are or by averaging them. The phase angles are chosen as the *raw* phase angles, *averaged* phase angles or they can be *adjusted* to be decreasing function of the frequency (see Fig. 2.4).

Two asphalt concrete specimens were subject to eight FSTs at five different temperatures (e.g., targeted –10°, 5°, 15°, 25°, and 35°C). Using time-temperature superposition principle, all the data are translated to a reference temperature of 5°C for the further comparison using raw data and processed data. The Prony-series representation curves determined from the suggested combinations are shown in Fig. 2.5. Since all the combinations perform equally well, Combination 3 is chosen based on its simplicity because it requires the least amount of computation time.

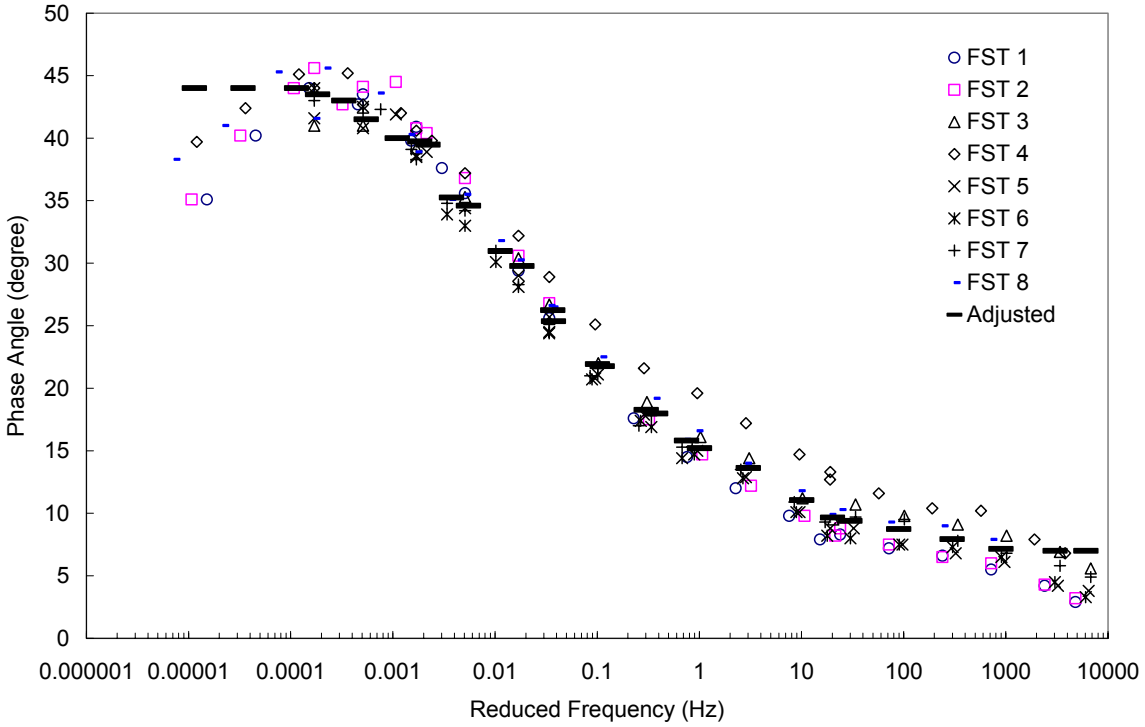

Figure 2.4 Adjusted Phase Angle at Temperature 5°C

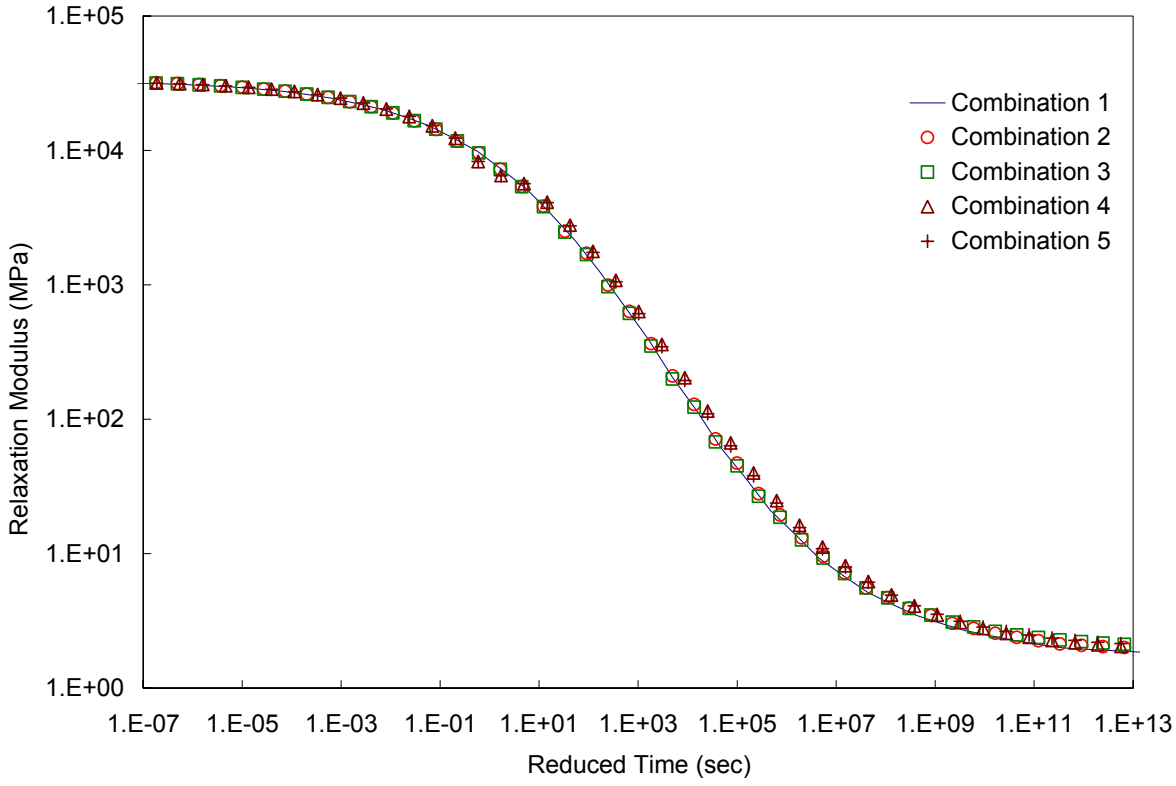

Figure 2.5 Relaxation Modulus Generated by Prony-Series Representation at 5°C

2.2 NUMERICAL INTEGRATION OF LINEAR VISCOELASTICITY

To solve the initial-boundary value problem involving linear viscoelasticity, the constitutive equation between stress and strain expressed in the convolution integral form of the relaxation modulus needs to be numerically integrated. Three techniques of numerical integration are evaluated here: composite trapezoidal integration, parabolic algorithm, and internal state variable approach.

The trapezoidal rule of convolution integral is employed based on the simple numerical procedure given by Linz (1985). The parabolic algorithm is implementing forward Euler, Crank-Nicolson, and backward Euler methods for the time-discretization as discussed by Hughes (2000). The numerical integral formulation of the internal state variable method for the constitutive modeling of viscoelastic materials is implemented based on the approach presented in Simo and Hughes (1998).

2.2.1 Numerical Integration Schemes

Composite Trapezoidal Rule

The relaxation modulus for a viscoelastic material is determined by stress responses from a strain history input; the following constitutive relation can be defined using the relaxation modulus in the form of the convolution integral:

$$\sigma(t) = \int_{-\infty}^{t} E(t-\tau)\frac{d\varepsilon(\tau)}{d\tau}d\tau \tag{2.23}$$

where $\sigma(t)$ is the stress, $E(t)$ is the relaxation modulus, and $\varepsilon(t)$ is the strain.

The constitutive equation for the considered viscoelastic materials in this work is derived using the Prony series of the relaxation modulus in Eq. (2.10). The following Volterra equation is resulted from integrating Eq. (2.23) by parts:

$$\varepsilon(t) = g(t) + \int_0^t k(t-\tau)\varepsilon(\tau)d\tau \tag{2.24}$$

where,

$g(t) = \sigma(t) / E(0)$,

$k(t-\tau) = \frac{1}{E(0)}\frac{d}{d\tau}E(t-\tau) = \frac{1}{E(0)}\sum_{m=1}^{M}\frac{E_m}{\rho_m}\exp(-(t-\tau))$, and

$E(0) = E_\infty + \sum_{m=1}^{M} E_m$.

The approximate solution $\varepsilon_h(t)$ of the Volterra equation can be computed by replacing the integral on the right hand side of Eq. (2.24) by a numerical trapezoidal rule using values of the integrand at t_i, $i = 0,1,...,n$ including the known equation of $\sigma(t)$. Since $\varepsilon(t_0=0) = g(t_0=0)$, the linear numerical solution of strain $\varepsilon_h(t_n)$ can be found in the following step-by-step scheme:

$$\varepsilon_h(t_n) = g(t_n) + \Delta t\left\{\frac{1}{2}k(t_n - t_0)\varepsilon(t_0) + \sum_{i=1}^{n-1}k(t_n - t_i)\varepsilon(t_i) + \frac{1}{2}k(t_n - t_n)\varepsilon(t_n)\right\}; \tag{2.25}$$

$$\left[1 - \frac{\Delta t}{2}k(0)\right]\varepsilon_h(t_n) = g(t_n) + \Delta t\left\{\frac{1}{2}k(t_n - t_0)\varepsilon(t_0) + \sum_{i=1}^{n-1}k(t_n - t_i)\varepsilon(t_i)\right\}. \tag{2.26}$$

In Box (2.1) the algorithm for the numerical trapezoidal rule is outlined. To perform semi-discrete time error analysis, the following theorem is applied to obtain the order of accuracy.

Box 2.1 Numerical Trapezoidal Algorithm

With known $\varepsilon(t_i,\ i=1,..,n-1)$, Δt, and $g(t_n)$ at n^{th} step

Compute $A_0 = 1 - \frac{\Delta t}{2} k(0)$ and

$$A_n = \Delta t \left\{ \frac{1}{2} k(t_n - t_0)\varepsilon(t_0) + \sum_{i=1}^{n-1} k(t_n - t_i)\varepsilon(t_i) \right\}$$

Obtain $\varepsilon_h(t_n) = \frac{g(t_n) + A_n}{A_0}$

Next step

Theorem 2.1. Let $K(t,\tau,\varepsilon(\tau))$ be second-order differentiable with respect to time with $\Delta t = t_n / n$ and $t_i = i\Delta t$ for each $i = 0,1,...,n$. The composite trapezoidal rule for n^{th} subinterval is:

$$\int_0^t K(t,\tau,\varepsilon(\tau))d\tau = \Delta t \left\{ \frac{1}{2} K(t_n,t_0,\varepsilon(t_0)) + \sum_{i=1}^{n-1} K(t_n,t_i,\varepsilon(t_i)) + \frac{1}{2} K(t_n,t_n,\varepsilon(t_n)) \right\}$$

$$- \frac{t_n \Delta t^2}{12} \ddot{K}(t_n,t_s,\varepsilon(t_s))$$

for some $t_s \in (0,t_n)$, where double overdot denotes double time derivative.

Proof.

If P_n is the Lagrange interpolating polynomial, $P_n(t,\tau,\varepsilon(\tau)) = \sum_{i=0}^{n} K(t_n,t_i,\varepsilon(t_i))L_i(t)$

where $L_i(t) = \prod_{\substack{j=0 \\ j\neq i}}^{n} \frac{(t - t_j)}{(t_i - t_j)}$.

Now, P_n and its truncation error term are integrated over [*0*, t_n] to obtain

$$\int_0^t K(t,\tau,\varepsilon(\tau))d\tau = \int_0^t \sum_{i=0}^{n} K(t_n,t_i,\varepsilon(t_i))L_i(t)dt + \int_0^t \prod_{i=0}^{n} \frac{(t_n - t_i)}{(n+1)!} K^{(n+1)}(t_n,t_s,\varepsilon(t_s))dt$$

$$= \sum_{i=0}^{n} a_i K(t_n,t_i,\varepsilon(t_i)) + \frac{1}{(n+1)!}\int_0^t \prod_{i=0}^{n} (t_n - t_i)\, K^{(n+1)}(t_n,t_s,\varepsilon(t_s))dt$$

where $a_i = \int_0^t L_i(t)dt$.

Let's consider the example of $P_1 = \frac{(t-t_1)}{(t_0-t_1)} K(t_1,t_0,\varepsilon(t_0)) + \frac{(t-t_0)}{(t_1-t_0)} K(t_1,t_1,\varepsilon(t_1))$.

Therefore,

$$\int_{t_0}^{t_1} K(t_n,t_i,\varepsilon(t_i))dt = \frac{(t_1-t_0)}{2}[K(t_1,t_0,\varepsilon(t_0)) + K(t_1,t_1,\varepsilon(t_1))] - \frac{(t_1-t_0)^3}{12}\ddot{K}(t_1,t_s,\varepsilon(t_s)).$$

This integration between t_0 and t_1 can be extended to multi-time discrete trapezoidal rule such as $t_i, i = 0,1,...,n$ by induction.

The error estimate related to time discretization can be easily obtained based on Theorem 2.1. Subtracting Eq. (2.25) from Eq. (2.24) gives:

$$\left|\varepsilon(t) - \varepsilon_h(t)\right| \le C\Delta t^2 \tag{2.27}$$

where C is a positive constant independent of ε.

Parabolic Algorithm

The parabolic equation can be constructed based on using Eqs. (2.13) to (2.15). First, Eq. (2.15) is differentiated with respect to time and then the differentiated Eq. (2.15) is multiplied by –1 to obtain the following matrix relation:

$$\underbrace{\begin{bmatrix} -E_\infty & -1 & . & . & -1 \\ -1 & 1/E_1 & 0 & 0 & 0 \\ . & 0 & . & 0 & 0 \\ . & 0 & 0 & . & 0 \\ -1 & 0 & 0 & 0 & 1/E_M \end{bmatrix}}_{[P]} \frac{d}{dt} \underbrace{\begin{bmatrix} \varepsilon(t) \\ \sigma_1 \\ . \\ . \\ \sigma_M \end{bmatrix}}_{\{d\}} + \underbrace{\begin{bmatrix} 0 & . & . & . & 0 \\ . & 1/\eta_1 & 0 & 0 & 0 \\ . & 0 & . & 0 & 0 \\ . & 0 & 0 & . & 0 \\ 0 & 0 & 0 & 0 & 1/\eta_M \end{bmatrix}}_{[Q]} \underbrace{\begin{bmatrix} \varepsilon(t) \\ \sigma_1 \\ . \\ . \\ \sigma_M \end{bmatrix}}_{\{d\}} = \underbrace{\begin{bmatrix} -\frac{d}{dt}\sigma(t) \\ 0 \\ . \\ . \\ 0 \end{bmatrix}}_{\{F\}}$$

or

$$[P]\{\dot{d}\} + [Q]\{d\} = \{F\} \tag{2.28}$$

where overdot denotes time derivative.

The initial value problem consists of finding a function $\{d\} = \{d(t)\}$, which satisfies Eq. (2.28) and the initial condition $\{d(t_0 = 0)\} = \{d_0\}$. The initial condition can be determined from Eq. (2.24) at t_0, which is $\varepsilon(t_0)=g(t_0)$, and the values σ_m ($m=1,\ldots,M$) being all zeros at t_0. For the discretization in time, the classical methods such as forward Euler, Crank-Nicolson, and backward Euler can be considered. These methods can be considered as special cases of the following general scheme (Hughes, 2000):

$$[P]\{v\}_{n+1} + [Q]\{d\}_{n+1} = \{F\}_{n+1} \tag{2.29}$$

$$\{d\}_{n+1} = \{d\}_n + \Delta t \{v\}_{n+\alpha} \tag{2.30}$$

$$\{v\}_{n+\alpha} = (1-\alpha)\{v\}_n + \alpha\{v\}_{n+1} \tag{2.31}$$

where $\{d\}_n$ and $\{v\}_n$ are the approximate solutions to $\{d(t_n)\}$ and $\{\dot{d}(t_n)\}$ respectively; Δt is a constant time increment; $\{F\}_{n+1} = \{F(t_{n+1})\}$. Forward Euler, Crank-Nicolson, and backward Euler methods can be obtained by choosing the value α = 0, ½, or 1 respectively. The implementation of the parabolic algorithm is shown in Box 2.2.

Box 2.2 Numerical Parabolic Algorithm

With the known $\{d\}_n$ and $\{v\}_n$

Compute the predictor value of d_{n+1}:

$$\{\hat{d}\}_{n+1} = \{d\}_n + (1-\alpha)\Delta t\{v\}_n$$

Using Eqs. (2.38) and (2.39), obtain the corrector value:

$$\{d\}_{n+1} = \{\hat{d}\}_{n+1} + \alpha\Delta t\{v\}_{n+1}$$

To obtain v_{n+1}, the above equation substituted into Eq. (2.37)

$$\{v\}_{n+1} = ([P] + \alpha\Delta t[Q])^{-1}(\{F\}_{n+1} - [Q]\{\hat{d}\}_{n+1})$$

Update $\{d\}_{n+1}$

Next step

Before the order of accuracy in parabolic algorithm is determined, the required property is the stability, which depends on the choice of α value. To find the appropriate indication of the stability, the homogeneous equation of Eq. (2.28) can be changed into modal representation:

$$\{\dot{d}\} + \lambda\{d\} = 0 \tag{2.32}$$

where λ is eigenvalue of $[Q]$ with respect to $[P]$. The above equation, when discretized in time, results in a relation between d_{n+1} and d_n as follows:

$$d_{n+1} = \frac{(1-(1-\alpha)\Delta t\lambda}{(1+\alpha\Delta t\lambda)} d_n \tag{2.33}$$

which implies that $\|d_{n+1}\| \le |A_m| \|d_n\|$. The amplification factor $|Am| = \left| \frac{(1-(1-\alpha)\Delta t\lambda)}{(1+\alpha\Delta t\lambda)} \right|$ should be less than one for stability of the time-integration. It can be seen that Crank-Nicolson and backward Euler methods are unconditionally stable; however, the forward Euler method has the following stability condition:

$$\Delta t < \frac{2}{\lambda}. \tag{2.34}$$

Considering an example with $E(t) = 1 + \exp(-t)$, two eigenvalues, $\lambda_1 = 0$ and $\lambda_2 = 0.5$, can be obtained. For stability, Δt should be less than 4. Figs. 2.6 and 2.9 show the results for various values of Δt (e.g., $\Delta t = 3$, 4 and 5). It can be clearly seen that when the time step size is larger than the stability limit ($\Delta t = 4$), the solution is unstable.

The order of accuracy in time discretization is evaluated based on Taylor series analysis of the truncation error. We expand the function values of $\{d\}$ in a Taylor series about t as follows:

$$\{d\}_{n+1} = \{d(t+\Delta t)\} = \{d(t)\} + \Delta t\{\dot{d}(t)\} + \frac{1}{2}\Delta t^2\{\ddot{d}(t)\} + \frac{1}{6}\Delta t^3\{\dddot{d}(t)\} + O(\Delta t^4); \tag{2.35}$$

$$\{d\}_{n-1} = \{d(t-\Delta t)\} = \{d(t)\} - \Delta t\{\dot{d}(t)\} + \frac{1}{2}\Delta t^2\{\ddot{d}(t)\} - \frac{1}{6}\Delta t^3\{\dddot{d}(t)\} + O(\Delta t^4), \tag{2.36}$$

which results in the following relations:

$$\frac{\{d\}_{n+1} - \{d\}_n}{\Delta t} - \{\dot{d}\}_n = \frac{1}{2}\Delta t\{\ddot{d}\}_n + \frac{1}{6}\Delta t^2\{\dddot{d}\}_n + O(\Delta t^3); \tag{2.37}$$

$$\frac{\{d\}_n - \{d\}_{n-1}}{\Delta t} - \{\dot{d}\}_n = -\frac{1}{2}\Delta t\{\ddot{d}\}_n + \frac{1}{6}\Delta t^2\{\dddot{d}\}_n + O(\Delta t^3). \tag{2.38}$$

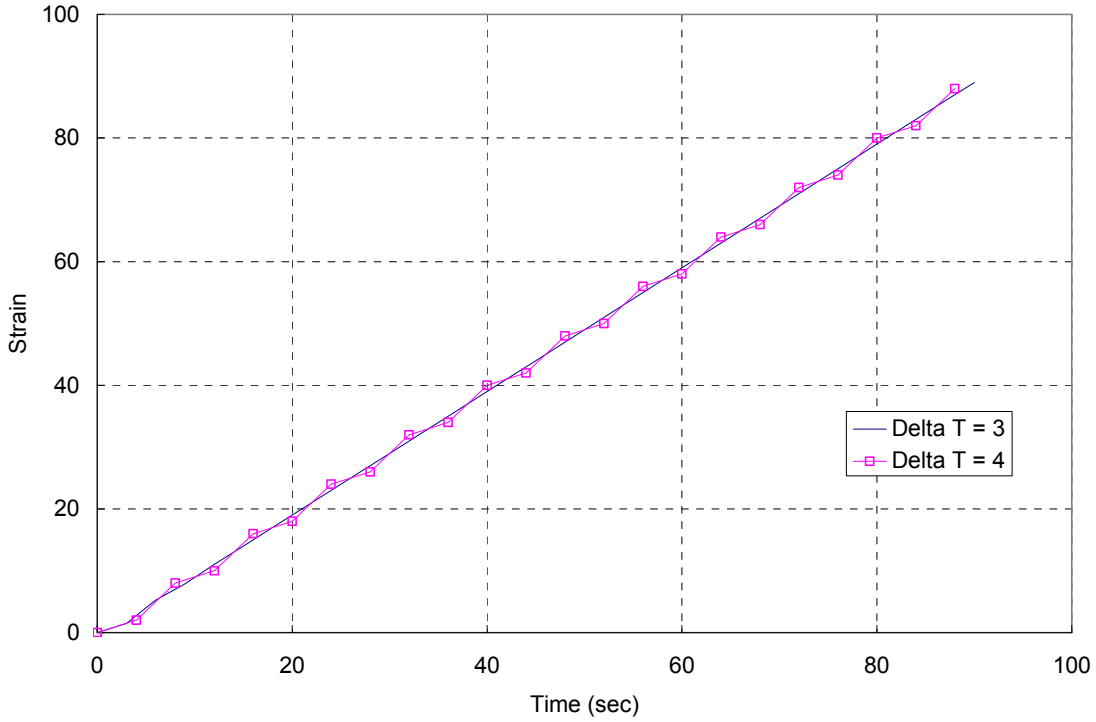

Figure 2.6 Instability at $\Delta t = 4$

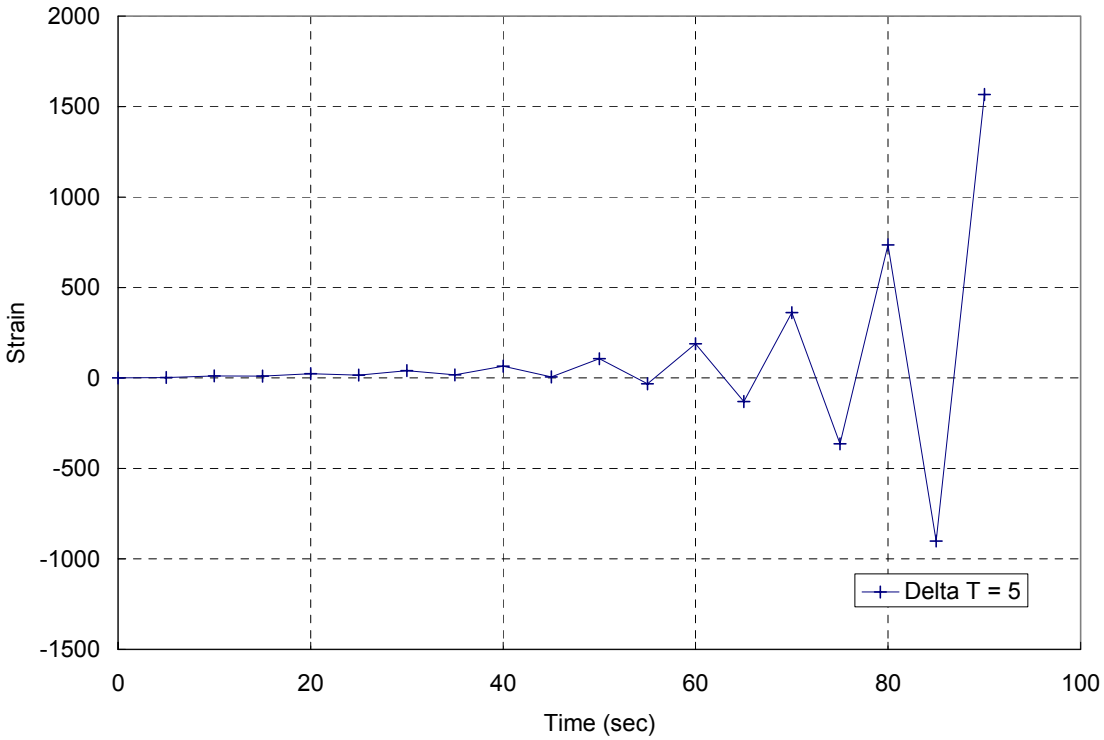

Figure 2.7 Instability at $\Delta t = 5$

Eq. (2.37) indicates the first order of accuracy in the forward Euler method. Similar argument can also be applied to backward Euler method. On the other hand, Crank-Nicolson method results in second order accuracy, which is based on the following observation:

$$\frac{\{d\}_{n+1}-\{d\}_n}{\Delta t}-\left\{\dot{d}\right\}_{n+\frac{1}{2}}=\frac{1}{6}\Delta t^2\left\{\dddot{d}\right\}_{n+\frac{1}{2}}+O(\Delta t^3). \tag{2.39}$$

Internal State Variable Approach

The internal state variable approach is based on the time discrete problem of the left hand side of Eq. (2.14), which is $(\varepsilon^{n+1}-\varepsilon^n)/\Delta t$, with the known initial state variable $\sigma_m = \sigma_m{}^n$ at $t=t_n$. The Δt can be chosen to be constant in this study. The solution of the discrete Eq. (2.14) is an exponential form as follows:

$$\sigma_m = a + b\exp\left[-(t-t_n)/\rho_m\right] \tag{2.40}$$

where a and b are constants. Based on the assumption of linearity between ε^{n+1} and ε^n, substituting Eq. (2.40) into Eq. (2.14) is carried out to obtain the constant a as follows:

$$\frac{b}{E_m}(-\frac{1}{\rho_m})\exp\left[-(t-t_n)/\rho_m\right]+\frac{1}{\eta_m}\left\{a+b\exp\left[-(t-t_n)/\rho_m\right]\right\}=\frac{\varepsilon^{n+1}-\varepsilon^n}{\Delta t}. \tag{2.41}$$

Because η_m equals to $E_m\rho_m$, the above exponential terms are canceled out and then, the constant a is found in the following form:

$$a=\eta_m\frac{\varepsilon^{n+1}-\varepsilon^n}{\Delta t}. \tag{2.42}$$

The initial state variable, which $\sigma_m=\sigma_m{}^n$ at $t=t_n$, is substituted into Eq. (2.40) for determining the finial constant value b as shown below:

$$b = \sigma_m^n - a \,. \tag{2.43}$$

According to the constitutive equation of Eq. (2.15), the determined constants, *a* and *b*, are used to obtain the following state variable expression at $t = t_{n+1}$:

$$\sigma_m^{n+1} = \underbrace{\exp(-\Delta t / \rho_m)\sigma_m^n}_{\sigma_m^{res}} + \underbrace{\frac{\eta_m}{\Delta t}(1 - \exp(-\Delta t / \rho_m)}_{Mod_m} \cdot (\varepsilon^{n+1} - \varepsilon^n) \,; \tag{2.44}$$

and therefore,

$$\sigma(t_{n+1}) = E_\infty \varepsilon^{n+1} + \sum_{m=1}^{M} \sigma_m^{res} + \sum_{m=1}^{M} Mod_m (\varepsilon^{n+1} - \varepsilon^n) \,. \tag{2.45}$$

The implementation of internal state variable algorithm is illustrated in the following Box 2.3.

Box 2.3 Numerical Internal State Variable Algorithm

With the known $\sigma(t_{n+1})$, ε^n, and σ_m^n at $t=t_n$

Obtain $Mod = \sum_{m=1}^{M} Mod_m$ and $\sigma^{res} = \sum_{m=1}^{M} \sigma_m^{res}$

Compute $\varepsilon^{n+1} = \dfrac{\sigma(t_{n+1}) - \sigma^{res} + Mod \cdot \varepsilon^n}{(E_\infty + Mod)}$

Update $\sigma_m^{n+1} = \sigma_m^{res} + Mod_m (\varepsilon^{n+1} - \varepsilon^n)$

Next step

For the error estimate of the state variable approach, the following second-order accuracy is determined based on the linearity between ε^{n+1} and ε^n:

$$\left| \frac{\varepsilon_{n+1} - \varepsilon_n}{\Delta t} - \dot{\varepsilon}_{n+1/2} \right| \le C\Delta t^2 \tag{2.46}$$

where C is a positive constant independent of ε.

2.2.2 Numerical Tests for Time Integration

Two examples (see Table 2.2) are used to evaluate the performance of the three different numerical integration algorithms.

Table 2.2 Relaxation Modulus and Creep Compliance Used in Numerical Examples

Example	Relaxation Modulus	Creep Compliance
I	$E(t) = 1 + \exp(-t)$	$1 - 0.5 \cdot \exp(-t/2)$
II	$E(t) = 1 + \exp(-t) + 2 \cdot \exp(-t/2)$	$1 - 0.125 \cdot \exp[-0.25(2+\sqrt{2})t] \cdot [3 - 2\sqrt{2} + (3+2\sqrt{2}) \cdot \exp(t/\sqrt{2})]$

In order to get the exact solutions in terms of calculating strain components, creep compliance, $D(t)$, is required to construct the following constitutive relationship between strain and stress:

$$\varepsilon(t) = \int_0^t D(t-\tau) \frac{d\sigma}{d\tau} d\tau \,. \tag{2.47}$$

Therefore, an elastic-viscoelastic correspondence principle is adopted. The correspondence principle reveals that the static elastic solutions can be converted to quasi-static viscoelastic solutions. The procedure involves replacing elastic moduli by the Carson transform of the moduli. Using this property, multiplying relaxation modulus,

E, by creep compliance, D, can be expressed in terms of the Carson or Laplace transformation in the following form:

$$\tilde{E}\tilde{D} = 1 \text{ or } \overline{ED} = \frac{1}{s^2} \tag{2.48}$$

where $\tilde{}$ and $\bar{}$ denote the Carson and Laplace transforms respectively, and s represents Laplace parameter. Using Eq. (2.48), the creep compliances corresponding to relaxation moduli can be obtained from solving the Laplace-transformation and -inversion problems. Table 2.2 shows the calculated creep compliances related to relaxation moduli used in this study.

The example constitutive relations are numerically integrated using the composite trapezoidal integration, parabolic algorithm, and internal state variable approach. The time history of stress in both examples is chosen as $t \cdot H(t)$ where $H(t)$ is a Heaviside step function. The time step sizes are chosen as 0.1, 0.05, 0.025, 0.0125, and 0.00625. The resultant strains are compared with the exact strains and the errors are examined in Figs. 2.8 and 2.9. Fig. 2.8 shows that the forward and backward Euler approaches provide first-order accuracy; other methods have second-order accuracy. In particular, both internal state variable and Crank-Nicolson can obtain more accuracy when compared to the composite trapezoidal rule; however, the internal state variable approach loses some accuracy in example II, which is shown in Fig. 2.9.

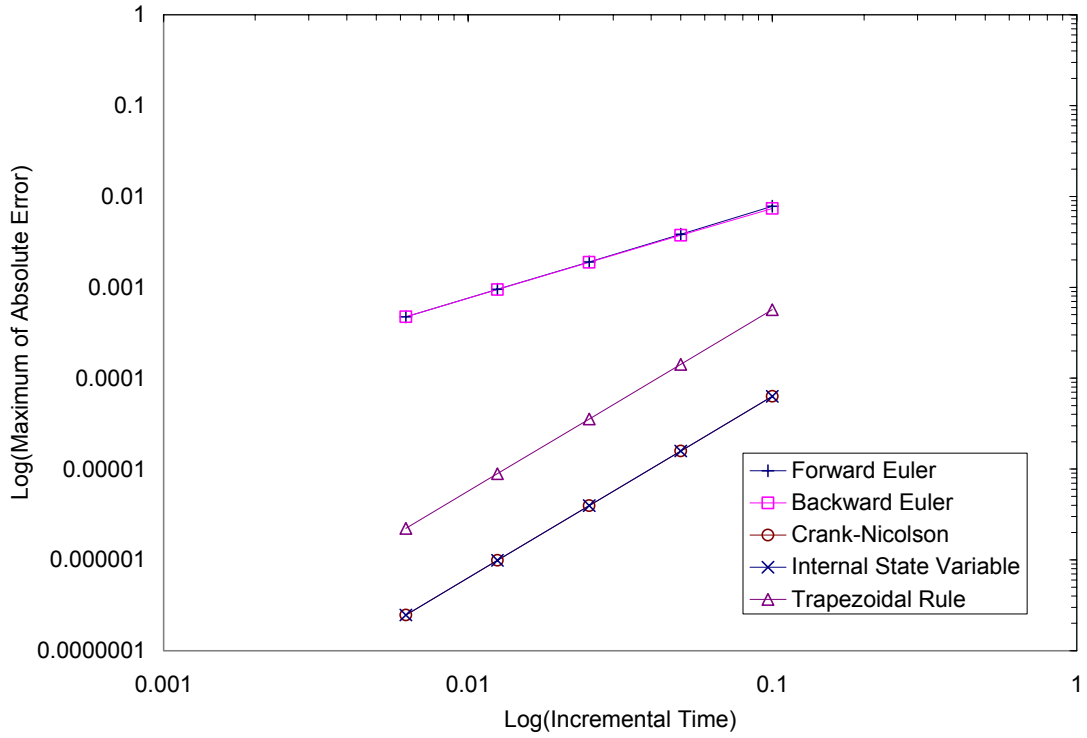

Figure 2.8 The Maximum of Absolute Errors in the Numerical Methods of Example I

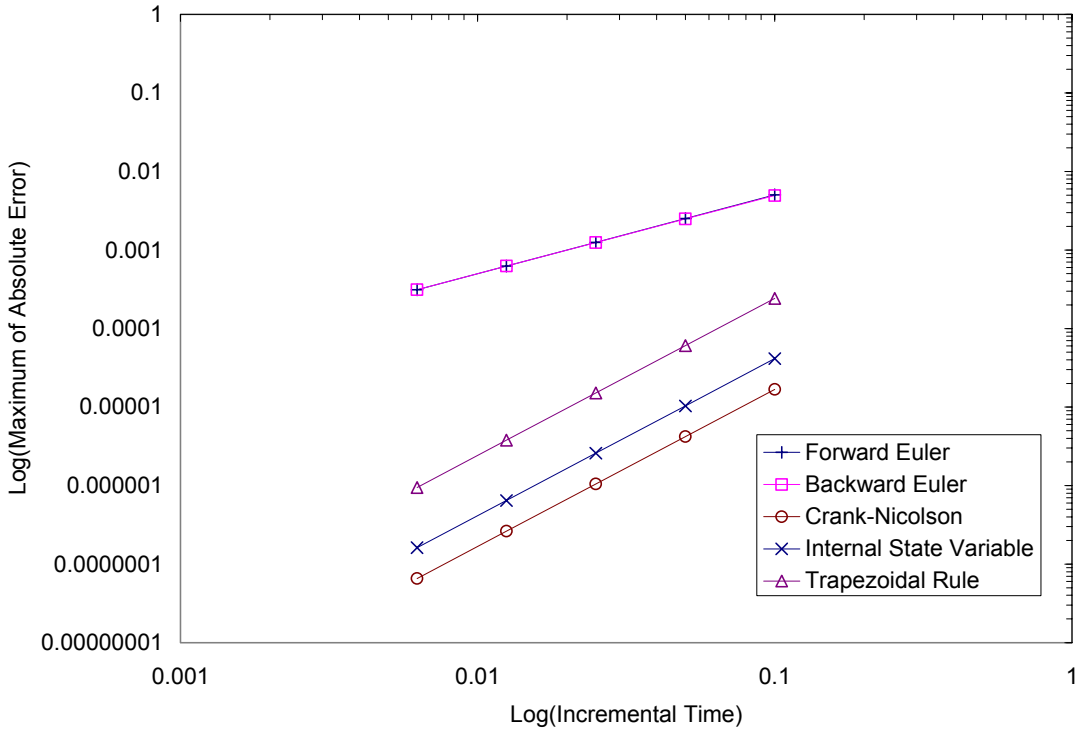

Figure 2.9 The Maximum of Absolute Errors in the Numerical Methods of Example II

2.3 VISCOELASTIC CONTINUUM DAMAGE MODEL

2.3.1 Material Modeling

Asphalt concrete is modeled as a thermorheologically simple material undergoing damage that is characterized with the help of the work potential theory. In this section, the work potential theory for viscoelastic damage mechanics is discussed in the framework of elastic damage mechanics coupled with the viscoelastic correspondence principle. The rest of the section describes: (a) the time-temperature superposition arising from thermorheological simplicity; (b) the work potential theory for damage in elastic solids; (c) the viscoelastic correspondence principle facilitating the link between the elastic damage theory and viscoelastic damage theory; and finally, (d) the complete viscoelastic damage theory.

All these theories are discussed using experimental results presented in Fig. 2.10, which contains the stress-strain relationships obtained using constant crosshead displacement rate tests.

Time-Temperature Superposition

The time temperature superposition states that the stress-strain behavior at a particular temperature at a given strain rate is identical to the stress-strain behavior at another temperature at a modified strain rate. This modified strain rate is obtained by simply scaling the time with a function of the temperature (a_T) using the following law:

$$t = a_T \cdot t_R \tag{2.49}$$

where t_R is the (reduced) time at the reference temperature (chosen to be 5ºC for this study), t is the time at the given temperature, and a_T is the time-temperature shift factor. For the given data, the shift factor is observed to be:

$$a_T = 10^{-0.0002(Temp.)^2 - 0.1308(Temp.) + 0.6582}.$$

Note that Fig. 2.10 contains experimental results at several temperatures, but the rates given in the figure are reduced rates at the reference temperature of 5ºC (see Table 2.3 for details). The magnified stress-strain curves in Fig. 2.11 clearly indicate the rate-dependent behavior of asphalt concrete – the material is generally stiffer and stronger at faster rates. For the remainder of this dissertation, all the experimental data will be viewed in the context of the reduced strain rates at the reference temperature.

Table 2.3 Reduced Strain Rate and Material Parameters of the Damage Function

Strain Rate	Reduced Strain Rate at a Reference Temp. 5ºC	Initial Pseudo Stiffness (I)	$C(S)$
0.00003/sec at 5ºC	0.00003/sec	0.81	$0.81\cdot\hat{C}(S)$
0.000056/sec at 5ºC	0.000056/sec	0.80	$0.80\cdot\hat{C}(S)$
0.000012/sec at 5ºC	0.000012/sec	1.02	$1.02\cdot\hat{C}(S)$
0.0135/sec at 25ºC	0.000026/sec	1.10	$1.10\cdot\hat{C}(S)$
0.0045/sec at 25ºC	0.0000086/sec	1.08	$1.08\cdot\hat{C}(S)$
0.0005/sec at 25ºC	0.000001/sec	1.15	$1.15\cdot\hat{C}(S)$
$\hat{C}(S) = \exp(-0.00228\cdot S^{0.506})$			

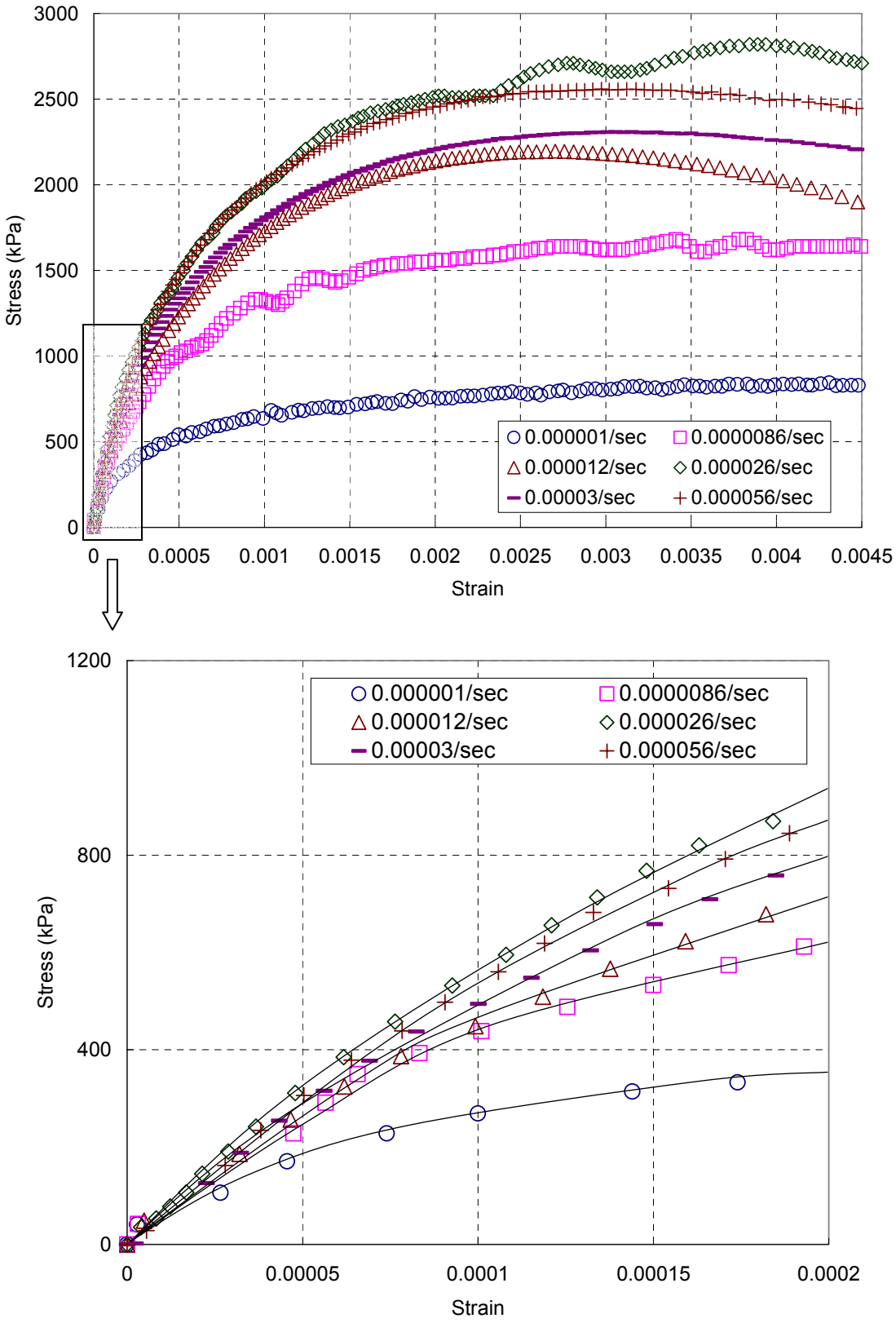

Figure 2.10 Stress/Strain Curves for Reduced Strain Rates in Tension

Elastic Damage Models

Schapery (1990, 1991) proposed a simple model for viscoelastic composites with growing damage that is based on replacing the physical displacements by quantities called pseudodisplacements. An elastic material's thermodynamic state is a function of independent generalized displacements, q_j ($j=1,2...J$), and internal state variables, S_m ($m=1,2...M$), where the inelastic behavior is captured from changes in S_m. Generalized forces, Q_j, are defined for each virtual displacement, δq, and virtual energy, δW, in the following form:

$$Q_j = \partial W / \partial q_j \,. \tag{2.50}$$

In isothermal conditions, the virtual energy, W, is the Helmholz free energy. Therefore, W can be viewed as the strain energy depending on the strain tensor, ε_{ij}, and internal state variables, S_m. In a standard physical setting of stress and strain, Eq. (2.50) becomes

$$\sigma_{ij} = \frac{\partial W}{\partial \varepsilon_{ij}} \qquad (i; j = 1,2,3) \tag{2.51}$$

where σ_{ij} are the stress components of the constitutive equation in the form of tensor notation.

The internal state variables are chosen to account for changes in the structure such as micro- or macrocracking based on the following damage evolution laws:

$$-\frac{\partial W}{\partial S_m} = \frac{\partial W_S}{\partial S_m} \tag{2.52}$$

where $W_S=W_S(S_m)$ is the dissipated energy due to damage growth. The left side of Eq. (2.52) is the available thermodynamic force for damage growth while the right side is the required force.

The above work potential theory is used as a guide to develop a three-dimensional constitutive relationship from the axisymmetric damage model. As suggested by Schapery, the elastic strain energy density for a locally transversely isotropic composite material can be written in the following form:

$$W = \frac{1}{2}\left[A_{11}e_V^2 + A_{22}e_d^2 + 2A_{12}e_d e_V + A_{44}(\gamma_{13}^2 + \gamma_{23}^2) + A_{66}(\gamma_{12}^2 + e_S^2)\right] \tag{2.53}$$

where x_3 is the axis of material symmetry and

$$\begin{gathered} e_V = \varepsilon_{11} + \varepsilon_{22} + \varepsilon_{33} \quad e_d = \varepsilon_{33} - e_V/3 \quad e_S = \varepsilon_{22} - \varepsilon_{11} \\ \gamma_{12} = 2\varepsilon_{12} \qquad \gamma_{13} = 2\varepsilon_{13} \qquad \gamma_{23} = 2\varepsilon_{23} \end{gathered} \tag{2.54}$$

and the five coefficients (e.g., A_{11}, A_{22}, A_{12}, A_{44}, and A_{66}) are the elastic moduli depending on the state of damage. When a uniaxial stress state is taken into account with a maximum strain direction to the axis of x_3 (e.g., $\varepsilon_{11} = \varepsilon_{22}$, $e_S = 0$, $\gamma_{12} = 0$, $\gamma_{13} = 0$, and $\gamma_{23} = 0$), the strain energy density Eq. (2.53) can be reduced to W' independent of A_{44}, in the form:

$$W' = \frac{1}{2}(A_{11}e_V^2 + A_{22}e_d^2 + 2A_{12}e_d e_V + A_{66}e_S^2)\,. \tag{2.55}$$

The derivative of Eq. (2.55) with respect to the principal strains (e.g., ε'_{11}, ε'_{22}, and ε'_{33}) provides the principal stresses. Thus:

$$\sigma'_{11} = (A_{11} - \frac{1}{3}A_{12})e_V + (A_{12} - \frac{1}{3}A_{22})e_d - A_{66}e_S$$
$$\sigma'_{22} = (A_{11} - \frac{1}{3}A_{12})e_V + (A_{12} - \frac{1}{3}A_{22})e_d + A_{66}e_S \quad (2.56)$$
$$\sigma'_{33} = (A_{11} + \frac{2}{3}A_{12})e_V + (A_{12} + \frac{2}{3}A_{22})e_d .$$

The relationship between the strains, ε_{jk} ($j, k = 1, 2, 3$) in the reference coordinate system, and the principle strains, ε'_{ii} ($i = 1, 2, 3$), is given by the general second order tensor transformation below:

$$\varepsilon'_{ii} = \Omega_{ij}\Omega_{ik}\varepsilon_{jk} \quad (2.57)$$

where the above transformation matrix Ω_{ij} is cosine(x'_i, x_j), which is the direction cosine of the axes between x'_i and x_j. A similar transformation law applies for stresses:

$$\sigma_{jk} = \Omega^T_{ik}\Omega^T_{ij}\sigma'_{ii} . \quad (2.58)$$

where $\bullet^T$ denotes the transpose of a matrix and σ'_{ii} is a diagonal tensor containing the principal stresses.

According to Schapery (1991) and Ha et al. (1998), the five coefficients, A_{11} to A_{66}, in Eq. (2.53), can be determined in terms of a damage function, $C(S)$, Poisson's ratio υ, and Young's modulus E:

$$A_{11} = \frac{1}{9}\left[C(S) + E\cdot\frac{2(1+\upsilon)}{(1-2\upsilon)}\right],\ A_{22} = C(S) + E\cdot\frac{(1-2\upsilon)}{2(1+\upsilon)},$$
$$A_{12} = \frac{1}{3}\left[C(S) - E\right],\ A_{44} = A_{66} = \frac{E}{2(1+\upsilon)}. \quad (2.59)$$

Viscoelastic Correspondence Principle

Correspondence principles in linear viscoelasticity theory usually refer to elastic-viscoelastic relationships involving Laplace or Fourier transformed stresses and strains. Instead, Schapery (1984) constructed a stress-strain constitutive equation for viscoelastic materials represented by an elastic-like relationship through the use of so-called pseudovariables. The correspondence principles developed by Schapery for time-dependent, quasi-static solutions to nonlinear viscoelastic boundary value problems can be used to enable a viscoelastic solution to be easily constructed from the elastic solution described in the above section. For linear viscoelastic materials, the stress-pseudostrain relationships take a form similar to elastic stress-strain relationships:

$$\sigma_{ij} = C^R_{ijkl}\varepsilon^R_{kl} \tag{2.60}$$

where

$$C^R_{ijkl} = \lambda\delta_{ij}\delta_{kl} + \mu(\delta_{ik}\delta_{jl} + \delta_{il}\delta_{jk}), \text{ and}$$

$$\varepsilon^R_{kl} = \frac{1}{E_R}\int_0^t E(t-\tau)\frac{\partial\varepsilon_{kl}}{\partial\tau}d\tau. \tag{2.61}$$

C^R_{ijkl} is the material constant, $\varepsilon_{kl}{}^R$ is the pseudostrain tensor, E_R is the reference modulus, $E(t)$ is the relaxation modulus, and λ and μ are Lamé constants in the following form:

$$\lambda = \frac{\upsilon E_R}{(1+\upsilon)(1-2\upsilon)}, \quad \mu = \frac{E_R}{2(1+\upsilon)}. \tag{2.62}$$

Furthermore, υ is a constant Poisson's ratio, and δ_{ij} is the Kronecker delta:

$$\delta_{ij}\begin{cases} = 1; & i = j \\ = 0; & i \neq j \end{cases}. \tag{2.63}$$

Note that all the hereditary effects of the viscoelastic material are accounted for through the convolution integral in Eq. (2.61).

Viscoelastic Damage Models

Schapery further extended his elastic damage theory to viscoelastic materials with the help of the correspondence principle (Schapery, 1984). To include the viscoelastic effects of microcracking, he proposed the following rate-type damage evolution law:

$$\dot{S}_m = \left(-\frac{\partial W^R}{\partial S_m} \right)^{\alpha_m} \tag{2.64}$$

where the overdot represents the derivative with respect to time, $W^R = W^R(\varepsilon_{ij}^R, S_m)$ is the pseudostrain energy density function, α_m is a material-dependent constant, and m is not summation. The available thermodynamic force, $-\partial W^R/\partial S_m$, is similar to a crack growth equation presented by Park el al. (1996). The form of the evolution law was adequate for describing the multiaxial behavior of particulate composites with growing damage (Park and Schapery, 1997). In this study, this approach is applied to asphalt concrete materials.

In order to determine the damage model parameter of the rate-type damage evolution, the stress responses at given strain rates and temperatures were measured, as shown in Fig. 2.14, under constant crosshead strain rate tests conducted on the cylindrical specimens (Ghehab, 2002). Furthermore, LVDTs were mounted on the specimen surface to measure displacements with respect to time, and the displacement was converted into the effective strain applied to the specimen. However, the lab results obtained from experimental tests show a discrepancy between the linear strains controlled by a closed-

loop servo-hydraulic MTS testing machine and the effective strains measured from the LVDT. In an attempt to ensure consistency in applying the viscoelastic theory with growing damage, the realistic strains from the LVDT were used for the analysis.

The experimental stress-strain constitutive relationship obtained from the above uniaxial tests was incorporated into the one-dimensional pseudostrain energy density function of the material in the following form:

$$W^R = \frac{1}{2} C(S)(\varepsilon^R)^2 \tag{2.65}$$

where the damage function, $C(S)$, depends on a single damage parameter, S. Then, the stress of Eq. (2.51) can be obtained based on Schapery's correspondence principle, as follows:

$$\sigma \equiv \frac{\partial W^R}{\partial \varepsilon^R} = C(S)\varepsilon^R \text{ or } C(S) = \frac{\sigma}{\varepsilon^R}. \tag{2.66}$$

Therefore, the damage function, $C(S)$, can be determined using the experimental stress, σ, and the pseudostrain, ε^R .

The pseudostrain is to be calculated using Eq. (2.61). Due to the expensive nature of the convolution integral, several authors have proposed efficient integration techniques (Taylor et al., 1970, Zocher et al., 1997, Kaliske et al., 1997, Poon et al., 1998, and Simo et al., 1998), based on the following Prony series approximation of the relaxation modulus:

$$E(t) = E_\infty + \sum_{m=1}^{M} E_m e^{-t/\rho_m} \tag{2.67}$$

where $E_{¶}$, E_m, and ρ_m are all constants. Using the above expression, it is shown that the convolution in Eq. (2.61) can be replaced by the following recursive computation (Hinterhoelzl, 2000):

$$\varepsilon_{kl}^{R,n+1} = \frac{1}{E_R}\left(E_0 \varepsilon_{kl}^{n+1} - \sum_{m=1}^{M} E_m \varepsilon_{kl}^{m,n+1} \right)$$

with $E_0 = E_\infty + \sum_{m=1}^{M} E_m$, and

$$\varepsilon_{kl}^{m,n+1} = \varepsilon_{kl}^{n} + e^{-\Delta t_{n+1}/\rho_m}(\varepsilon_{kl}^{m,n} - \varepsilon_{kl}^{n}) + \frac{\Delta \varepsilon_{kl}^{n+1}}{\Delta t_{n+1}}\left[\Delta t_{n+1} - \rho_m\left(1 - e^{-\Delta t_{n+1}/\rho_m}\right)\right]. \qquad (2.68)$$

In the above, the pseudostrain is split into M component pseudostrains based on the Prony series expansion of Eq. (2.67).

For uniaxial loading conditions, a single damage variable (S) is used along with the associated power, α . The value of α is obtained using the experimental data and by the following incremental relationship obtained by combining Eqs. (2.64) and (2.65):

$$\Delta S = \left[\left\{ -\frac{1}{2} \Delta C (\varepsilon^R)^2 \right\}^{\alpha} \Delta t \right]^{1/(1+\alpha)} \quad \text{then,}$$

$$S \cong \sum_{n=1}^{N} \left[\frac{1}{2} (C_{n-1} - C_n)(\varepsilon_n^R)^2 \right]^{\alpha/(1+\alpha)} (t_n - t_{n-1})^{1/(1+\alpha)}. \qquad (2.69)$$

Using optimization search techniques and the data from the first two cases in Table 2.3, the value of α is found to be equal to 2.5. Furthermore, a relationship is constructed between C and S, as shown in Fig. 2.11. Note that the specimen-to-specimen variation is taken into account by assuming that all the results scale by the initial pseudostiffness (see

Fig. 2.12). From Figs. 2.11 and 2.12, it can be observed that the stiffness scale factor, C(S), can be fit into the normalized functional form $\hat{C}(S) = \exp(-0.00228 \cdot S^{0.506})$.

The three-dimensional continuum damage viscoelastic model is similarly obtained by simply using the correspondence principle in the framework of three-dimensional elastic damage mechanics. Using this idea, the pseudostrain energy density function is defined as:

$$W^R = \frac{1}{2}\left\{A_{11}\left(e_V^R\right)^2 + A_{22}\left(e_d^R\right)^2 + 2A_{12}e_d^R e_V^R + A_{44}\left[\left(\gamma_{13}^R\right)^2 + \left(\gamma_{23}^R\right)^2\right]\right.$$

$$\left. + A_{66}\left[\left(\gamma_{12}^R\right)^2 + \left(e_S^R\right)^2\right]\right\} \tag{2.70}$$

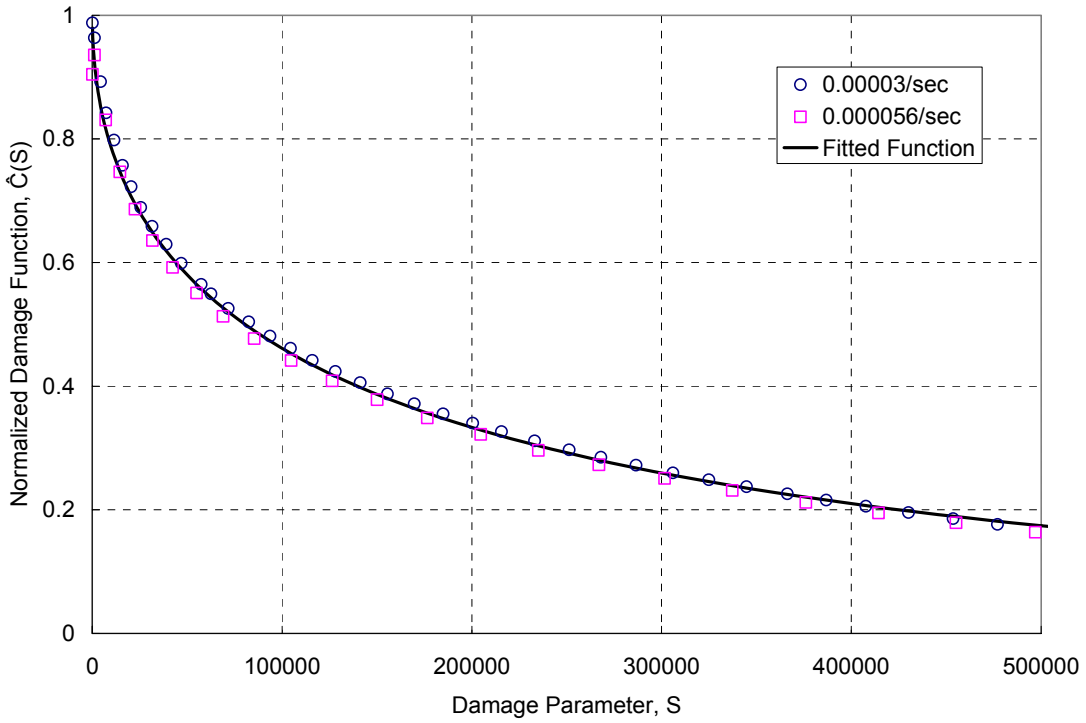

Figure 2.12 Normalized Damage Function/Parameter Curves for Two Fast-Reduced Strain Rates

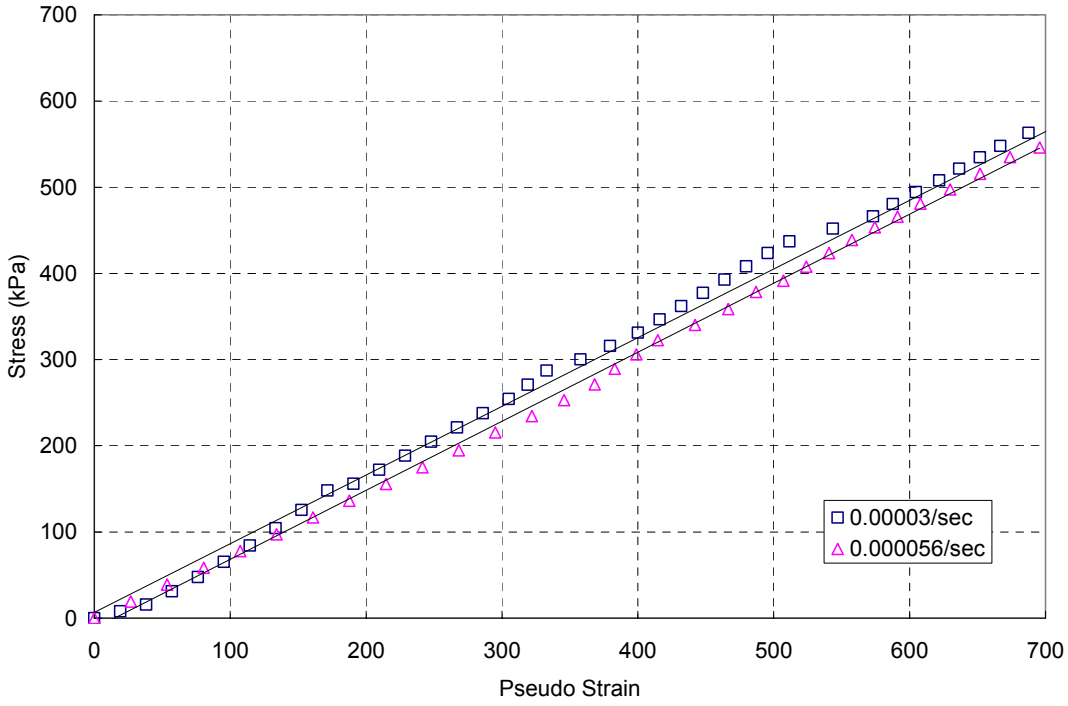

Figure 2.13 Stress vs. Pseudostrain Plot to Obtain Initial Pseudostiffness

where $\begin{matrix} e_V^R = \varepsilon_{11}^R + \varepsilon_{22}^R + \varepsilon_{33}^R & e_d^R = \varepsilon_{33}^R - e_V^R/3 & e_S^R = \varepsilon_{22}^R - \varepsilon_{11}^R \\ \gamma_{12}^R = 2\varepsilon_{12}^R & \gamma_{13}^R = 2\varepsilon_{13}^R & \gamma_{23}^R = 2\varepsilon_{23}^R. \end{matrix}$ (2.71)

In terms of principal pseudostrains,

$$W'^R = \frac{1}{2}\left[A_{11}\left(e_V^R\right)^2 + A_{22}\left(e_d^R\right)^2 + 2A_{12}e_d^R e_V^R + A_{66}\left(e_S^R\right)^2\right], \tag{2.72}$$

that results in the following constitutive relationships between stress and pseudostrain:

$$\begin{aligned} \sigma'_{11} &= (A_{11} - \frac{1}{3}A_{12})e_V^R + (A_{12} - \frac{1}{3}A_{22})e_d^R - A_{66}e_S^R \\ \sigma'_{22} &= (A_{11} - \frac{1}{3}A_{12})e_V^R + (A_{12} - \frac{1}{3}A_{22})e_d^R + A_{66}e_S^R \\ \sigma'_{33} &= (A_{11} + \frac{2}{3}A_{12})e_V^R + (A_{12} + \frac{2}{3}A_{22})e_d^R. \end{aligned} \tag{2.73}$$

2.3.3 Finite Element Implementation

Due to the nonlinear nature of damage, Newton-type iterative methods are needed to solve the equilibrium equations. The tangent stiffness matrix needed in the solution procedure is obtained using the tangent modulus relating the infinitesimal increase in the stress to the infinitesimal increase in the strain. For damaged viscoelastic solids, the tangent modulus is obtained using the following chain rule resulting from the ideas of the correspondence principle:

$$C_{ijkl} = \frac{\partial \sigma_{ij}}{\partial \varepsilon_{kl}} = \frac{\partial \sigma_{ij}}{\partial \varepsilon_{pq}^R} \cdot \frac{\partial \varepsilon_{pq}^R}{\partial \varepsilon_{kl}} \tag{2.74}$$

For linear Viscoelasticity, the terms in the right side of the above equation are given by:

$\frac{\partial \sigma_{ij}}{\partial \varepsilon_{pq}^R} = C_{ijpq}^R$ and

$$\frac{\partial \varepsilon^R_{pq}}{\partial \varepsilon_{kl}} = \frac{\partial \varepsilon^R_{kl}}{\partial \varepsilon_{kl}} = \frac{1}{E_R}\left\{E_\infty + \frac{1}{\Delta t_{n+1}}\left[\sum_{m=1}^{M} \rho_m E_m (1 - e^{-\frac{\Delta t_{n+1}}{\rho_m}})\right]\right\} \tag{2.75}$$

where C^R_{ijpq} is defined by Eq. (2.61). Noting that in Eq. (2.61), E_∞, E_m, and ρ_m are all constants, it is observed that the tangent modulus for linear viscoelastic solids is dependent only on the time step size Δt_{n+1}.

To obtain the tangent modulus for growing damage, the chain rule (Eq. (2.74)) is modified in terms of the work potential as follows:

$$\begin{aligned} C_{pprr} &= \frac{\partial \sigma'_{pp}}{\partial \varepsilon^R_{rr}} \cdot \frac{\partial \varepsilon^R_{rr}}{\partial \varepsilon_{rr}} = \frac{\partial^2 W^R}{\partial^2 \varepsilon^R_{rr}} \cdot \frac{\partial \varepsilon^R_{rr}}{\partial \varepsilon_{rr}} \\ C_{1212} &= \frac{\partial^2 W^R}{\partial^2 \gamma^R_{12}} \cdot \frac{\partial \gamma^R_{12}}{\partial \gamma_{12}},\ C_{1313} = \frac{\partial^2 W^R}{\partial^2 \gamma^R_{13}} \cdot \frac{\partial \gamma^R_{13}}{\partial \gamma_{13}},\ C_{2323} = \frac{\partial^2 W^R}{\partial^2 \gamma^R_{23}} \cdot \frac{\partial \gamma^R_{23}}{\partial \gamma_{23}} \end{aligned} \tag{2.76}$$

The terms $\partial \varepsilon_{rr}{}^R/\partial \varepsilon_{rr}$, $\partial \gamma_{12}{}^R/\partial \gamma_{12}$, $\partial \gamma_{13}{}^R/\partial \gamma_{13}$, and $\partial \gamma_{23}{}^R/\partial \gamma_{23}$ are all related to the definition of the pseudostrain, which is identical to the pseudostrain in the linear viscoelastic case; Eq. (2.75) can be readily used to compute these terms. The pseudostiffness, $\partial^2 W^R / \partial^2 \varepsilon^R_{rr}$, is obtained by using an incremental form of Eq. (2.70). Note that the pseudostiffness will be in terms of the coefficients A_{11}, A_{12}, A_{22}, and A_{66}, which are functions of the damage function, $C(S)$ (see Eq. (2.59)).

Once the tangent stiffness is obtained from Eq. (2.76) in the principal stress directions, a standard fourth order tensor transformation can be used to obtain the tangent stiffness in the original coordinate system:

$$C_{ijkl} = \Omega_{ip}\Omega_{jq}\Omega_{kr}\Omega_{ls}C_{pqrs} \tag{2.77}$$

where Ω_{nm} is the rotation tensor given in Eq. (2.57).

The procedure described above is implemented in ABAQUS with the help of the user-defined subroutine capability, UMAT. Essentially, ABAQUS solves the equilibrium equations with the help of a Newton-type iterative method. UMAT provides the user with the flexibility of computing the unbalanced force as well as the tangent modulus at the numerical integration points. In addition, UMAT should update the damage state variables. Keeping these requirements in mind, the implementation of UMAT involves the following steps:

1. Calculate the pseudostrain using the numerical integration scheme in Eq. (2.68). Using these strains, determine the principal pseudostrains as well as the transformation matrix in Eq. (2.57).

2. Calculate principal stresses, which are functions of material coefficients (e.g., A_{11}, A_{22}, A_{12}, and A_{66}) and the pseudostrain. Transform the principal stresses back to the stresses in the reference Cartesian coordinate (x_1, x_2, x_3) system using the transformation matrix. These stresses are used to compute the residual needed for the Newton iteration performed by ABAQUS.

3. Determine the 36 components of the incremental tangent modulus using an incremental form of Eq. (2.77).

4. Update the damage parameter, S, using an incremental form of the rate-type evolution law (Eq. (2.64)) and the definition of pseudostrain energy density (Eq. (2.72)). The resulting updated procedure is given below:

$$\Delta S_{n+1}^{update} = \left\{ -\frac{\left[W'^{R}(S_n + \Delta S_{n+1}^{assumed}) - W'^{R}(S_n) \right]}{\Delta S_{n+1}^{assumed}} \right\}^{\alpha} \Delta t_{n+1}$$
$$S_{n+1} = S_n + \Delta S_{n+1}^{update} \tag{2.78}$$

The above steps are embedded in the equilibrium solution process of ABAQUS that gradually increases the loading to obtain the incremental response of the system.

2.3.3 Verification with Experimental Data and FEP++ Implementation

The material modeling approach presented in Section 2.3.1 and the finite element implementation in Section 2.3.2 are verified with the use of the experimental results presented in Fig. 2.10. The cylindrical test specimen is modeled with the help of 8-node three-dimensional brick finite elements. To reduce computational time, only a quarter of the cylinder is modeled by considering the symmetry of the specimen as well as the loading. As discussed before, the experimental data corresponding to 0.00003/sec and 0.000056/sec reduced strain rates are used to characterize the viscoelastic damage parameters. The resulting damage parameters are, in turn, used in the finite element analysis to obtain the response of the cylindrical specimen. The computed results are compared with the experimental results in Fig. 2.14. The close match between the computed and observed results verifies the accuracy of the finite element implementation.

In order to verify the effectiveness of the material modeling procedure, the finite element analysis is conducted on the same specimen, but at different reduced strain rates varying from 0.000012/sec down to 0.000001/sec (see Table 2.3). The computed results are compared with observed experimental results in Figs. 2.15-2.18. It can be clearly seen that for faster reduced strain rates (Figs. 2.15 and 2.16), the prediction is excellent.

On the other hand, Figs. 2.17 and 2.18 indicate that there is a significant error in the prediction when the reduced strain rate is decreased. This discrepancy is attributed to the fact that the presented material model does not include viscoplasticity, which has a significant effect on the deformation behavior at low strain rates (Park el al., 1996). Nevertheless, for higher strain rates, where viscoplasticity is negligible, the viscoelastic damage model and its finite element implementation are accurate.

Based on the successful implementation of ABAQUS, the continuum damage model is implemented in a general-purpose finite element program VECD-FEP++ in an axisymmetric setting. The VECD-FEP++ implementation is verified via the comparison with the result from ABAQUS. A simple axisymmetric problem subject to a tension loading and a uniaxial boundary condition is set up for both of VECD-FEP++ and ABAQUS. In Fig. 2.19, the comparison shows an excellent agreement.

2.3.4 Summary

In this study, the viscoelastic continuum damage model has been implemented in the context of the finite element method. Both the finite element implementation and the applicability of the damage model for asphalt concrete were tested with the help of experimental data. The finite element implementation is verified to be accurate, and the damage model is accurate for reduced strain rates greater than approximately 0.000012/sec. For lower rates, viscoplastic deformation appears to be significant, necessitating the inclusion of viscoplasticity into the material model. Viscoplastic model development and its implementation into the finite element framework are the subjects of future study.

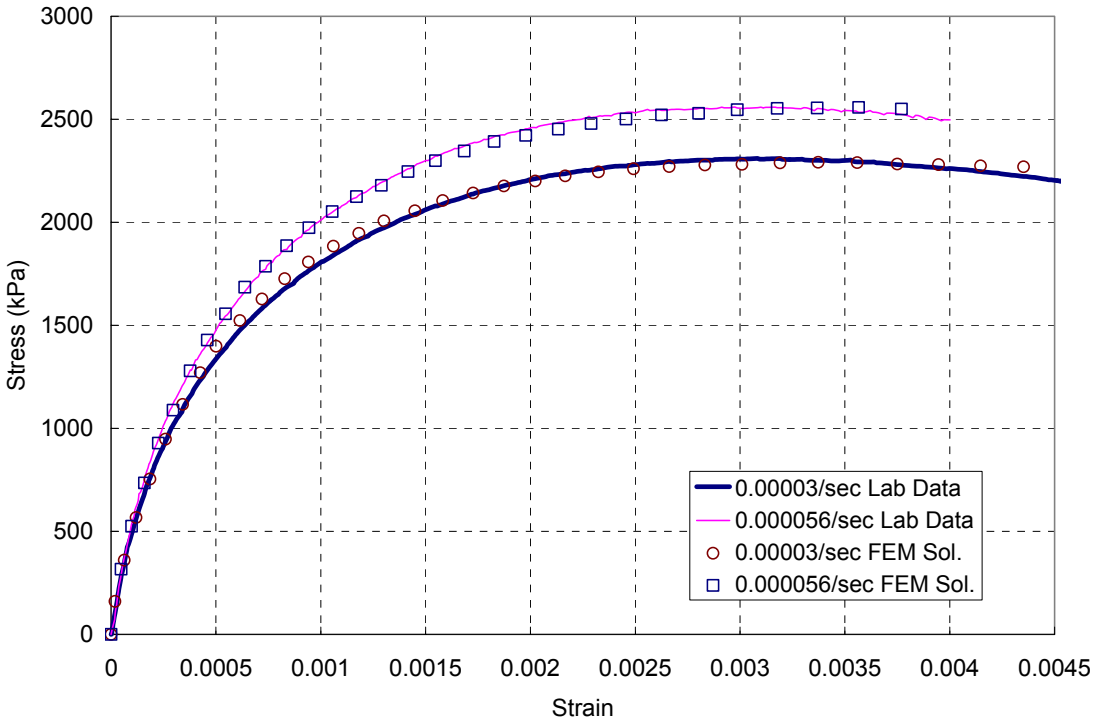

Figure 2.14 Stress Prediction of 0.00003/sec and 0.000056/sec Reduced Strain Rates Used for Constructing Master Damage Function

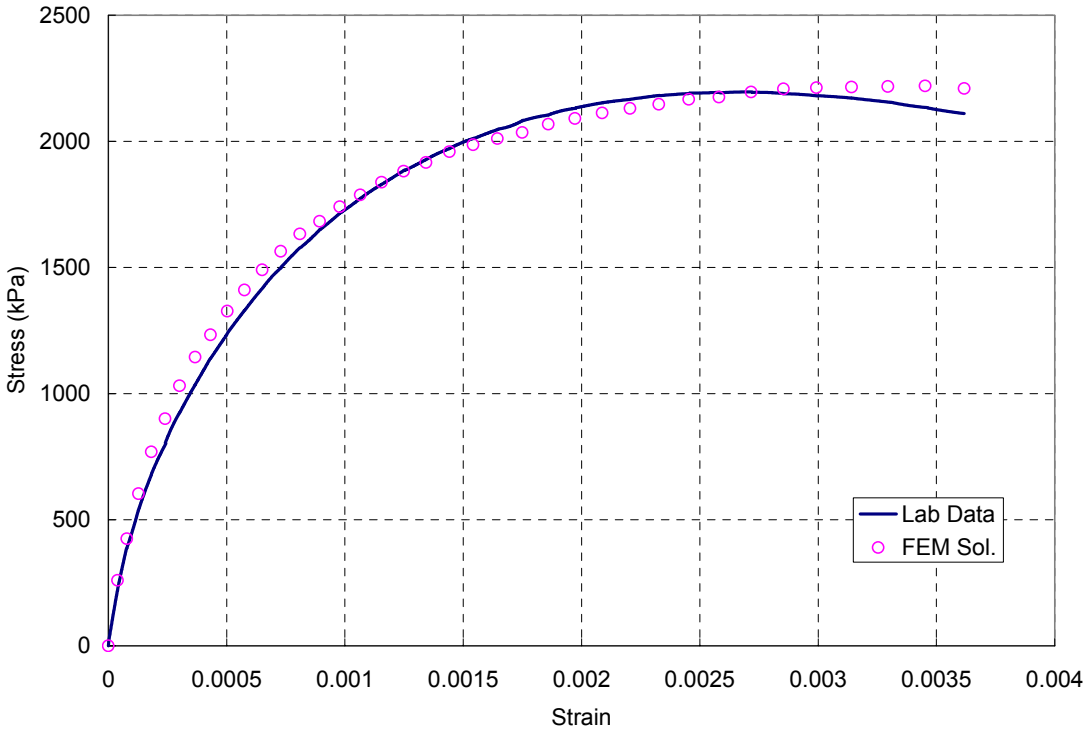

Figure 2.15 Stress Prediction of 0.000012/sec Reduced Strain Rate

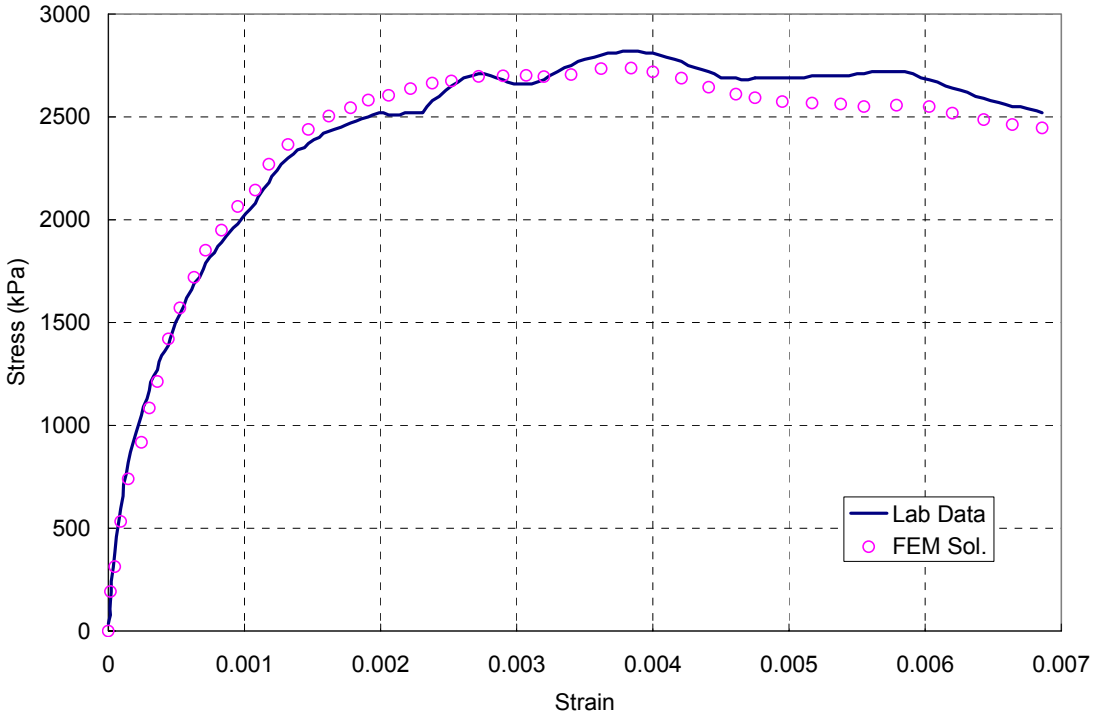

Figure 2.16 Stress Prediction of 0.000026/sec Reduced Strain Rate

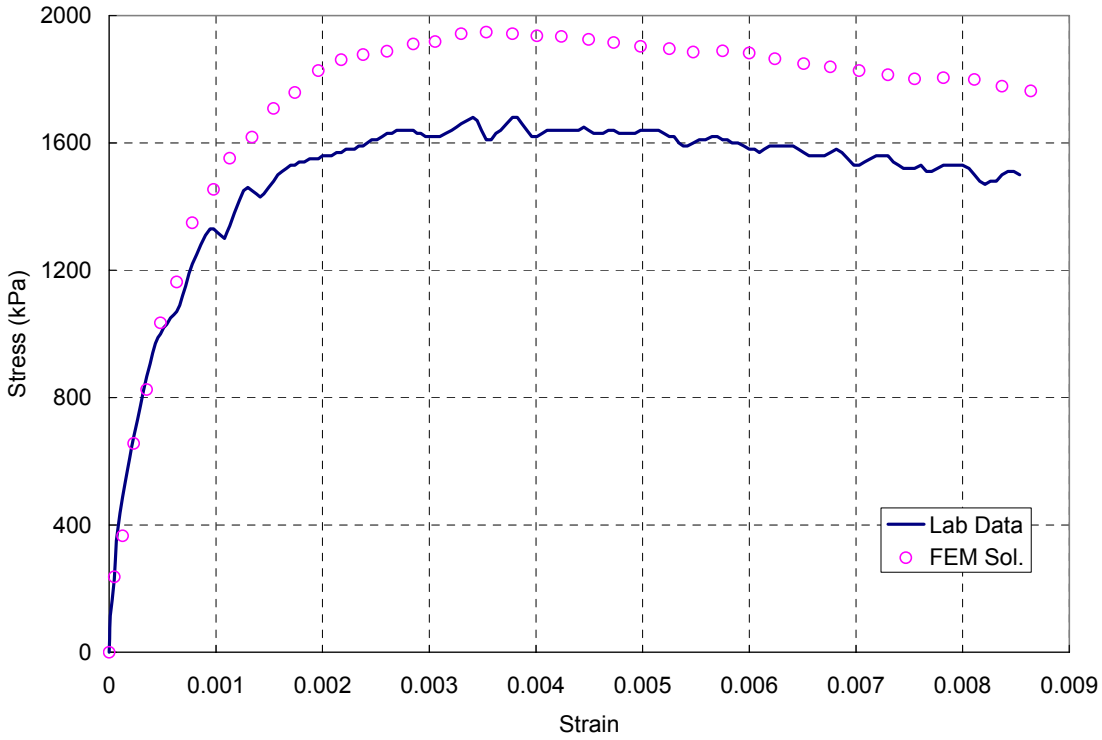

Figure 2.17 Stress Prediction of 0.0000086/sec Reduced Strain Rate

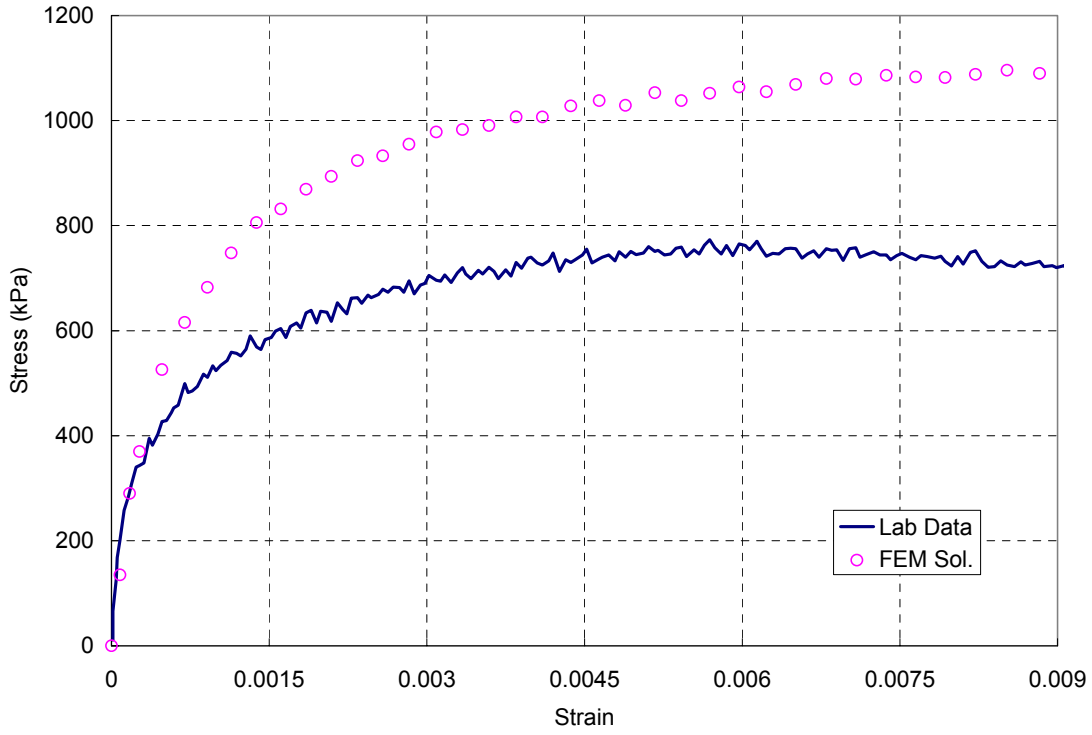

Figure 2.18 Stress Prediction of 0.000001/sec Reduced Strain Rate

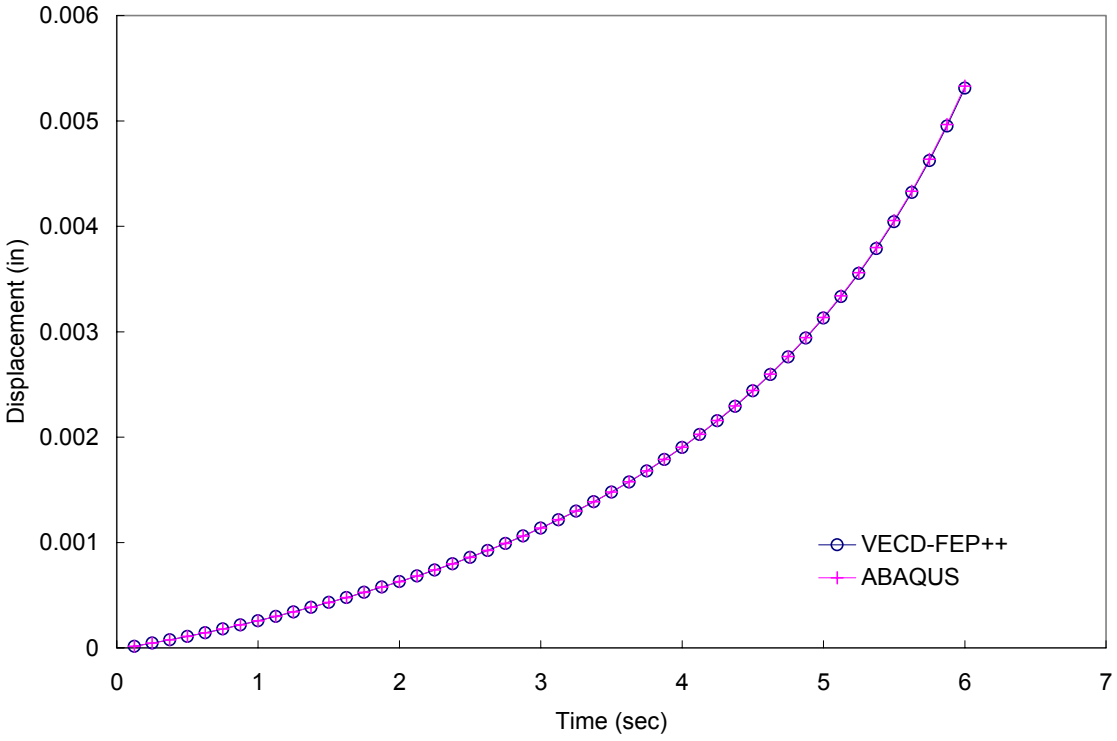

Figure 2.19 Comparison between ABAQUS and VECD-FEP++

CHAPTER 3

MODELING OF AGGREGATE BASE AND SUBGRADE

One of the most typical structures in asphalt pavements is aggregate base pavement. Aggregate base pavement is composed of asphalt surface layer, aggregate base course, and compacted subgrade on top of the natural subgrade. The deformation response of the aggregate base and subgrade materials is modeled in this study using a stress state dependent nonlinear elastic material model (or so called the universal model). The universal model is stress-based and is not amenable to displacement-based FEM. In this chapter, a procedure to include the universal model into the displacement-based finite element formulation is described.

3.1 RESILIENT MODULUS OF UNBOUND MATERIALS

The resilient modulus is determined under cyclic triaxial tests as the ratio of the cyclic axial stress to recoverable axial strain after a certain number of cycles. Many nonlinear elastic models have been proposed by researchers in order to incorporate the stress dependent effects of granular and fine-grained soils through the resilient modulus (e.g., Brown and Pappin (1981); Witczak and Uzan (1988); Elliot and David (1989)). The universal model, selected for this study, was suggested by Witczak and Uzan (1988). The original form of the model can be expressed as:

$$M_r = k_1 P_a \left(\frac{\theta}{P_a} \right)^{k_2} \left(\frac{\sigma_d}{P_a} \right)^{k_3} \tag{3.1}$$

where k_1 to k_3 are the material parameters, P_a is the atmospheric pressure, θ is the bulk stress, and σ_d is the deviator stress. A strain-based formulation is performed by replacing σ_d in Eq. (3.1) with the octahedral shear stress, τ_{oct}, using the following relationship:

$$\tau_{oct} = (\sqrt{2}/3)\sigma_d \tag{3.2}$$

This replacement results in:

$$M_r(\theta, \tau_{oct}) = k_4 \theta^{k_2} \tau_{oct}^{k_3} \tag{3.3}$$

where $k_4 = k_1 P_a \left(1/P_a\right)^{k_2} \left(2.12/P_a\right)^{k_3}$, τ_{oct} is the octahedral shear stress defined as $\sqrt{\frac{2}{3} J_2}$, and J_2 is the second invariant of the stress deviatoric tensor ($= \frac{1}{2} S_{ij} S_{ij}$) through the following expression:

$$S_{ij} = \sigma_{ij} - \tfrac{1}{3}\theta\delta_{ij} \tag{3.4}$$

where δ_{ij} is the Kronecker delta. The model including the influence of octahedral shear stress reduces to the bulk stress model in the case of $k_3 = 0$. Additionally, the stress state dependent model often used to describe the behavior of fine-grained soils can be obtained by setting k_2 to zero.

The finite element methods of the nonlinear elastic models have been implemented using iterative search techniques. ILLI-PAVE (Raad and Figueroa (1980)) and MICH-PAVE (Harichandran et al. (1989)) are costly due to the need for a large number of iterations. The current numerical implementation is based on the more efficient Newton-type method suggested by Hjelmstad et al. (2000). They remodeled the stress-dependent resilient modulus into the strain-dependent modulus via relating stress

invariants to strain invariants. The resulting model is amenable to implementation in standard displacement-based finite element framework.

3.2 CONSTITUTIVE MODELS

The constitutive equation of the universal resilient modulus, which gives the stress as a function of the deformation history of a solid body, is used for characterizing the granular material and fine-grained soil responses. Using the index notation, the stress-strain expression of an isotropic material is given by:

$$\sigma_{ij} = K\varepsilon_V \delta_{ij} + 2G\varepsilon'_{ij} \tag{3.5}$$

where K is bulk modulus equal to $E/3(1-2\upsilon)$, G is shear modulus equal to $E/2(1+\upsilon)$, E is Young's modulus, υ is Poisson's ratio, ε_V is volumetric strain ($=\varepsilon_{kk}$), and ε'_{ij} are deviatoric components ($=\varepsilon_{ij} - \varepsilon_V \delta_{ij}/3$). For resilient modulus models, the Young's modulus, E, can be replaced by the universal material modulus, M_r. Hjelmstad et al. (2000) adopted the notational convenience of defining $C = M_r/(1+\upsilon)$. They showed the nonlinear elastic constitutive equations of the resilient modulus in the following form:

$$\sigma_{ij} = C(\sigma)(\delta_{ijkl} + \alpha\delta_{ij}\delta_{kl})\varepsilon_{kl} \tag{3.6}$$

where $\alpha = \upsilon/(1-2\upsilon)$, and $\delta_{ijkl} = 1$ if $ij = kl$ or $\delta_{ijkl} = 0$ if $ij \neq kl$. The secant modulus is then obtained as the following stress-dependent form:

$$D_{ijkl} = C(\sigma)(\delta_{ijkl} + \alpha\delta_{ij}\delta_{kl}). \tag{3.7}$$

The bulk stress and the octahedral shear stress components in Eq. (3.5) are separately expressed in terms of volumetric strain, ε_V, and octahedral shear strain, ε_{oct}

(= $\sqrt{\frac{1}{3}\varepsilon'_{ij}\varepsilon'_{ij}}$), respectively. Taking the absolute value of the volumetric strain (because of the compression notation to be negative sign in solid mechanics) gives the following decomposed expressions:

$$\theta = K\left|\varepsilon_V\right|;\ \tau_{oct} = 2G\varepsilon_{oct}\,. \tag{3.8}$$

The above equations can be reformulated by replacing Young's modulus with the resilient modulus. The final forms are expressed in terms of $C(\theta,\tau_{oct})$.

$$\theta = \hat{\alpha}C(\theta,\tau_{oct})\left|\varepsilon_V\right|;\ \tau_{oct} = C(\theta,\tau_{oct})\varepsilon_{oct} \tag{3.9}$$

where $\hat{\alpha} = \alpha + \frac{1}{3}$. Substituting Eq. (3.3) into the above equations results in:

$$\theta^{k_2-1}\tau_{oct}^{k_3} = \frac{1}{k\hat{\alpha}\left|\varepsilon_V\right|};\ \theta^{k_2}\tau_{oct}^{k_3-1} = \frac{1}{k\varepsilon_{oct}} \tag{3.10}$$

where $k = k_4/(1+\upsilon)$. These two equations in Eq. (3.10) can be used for solving for θ and τ_{oct} in terms of $\left|\varepsilon_V\right|$ and ε_{oct} to get:

$$\theta = k^{\mu}(\hat{\alpha}\left|\varepsilon_V\right|)^{\mu(1-k_3)}\varepsilon_{oct}^{\mu k_3};\ \tau_{oct} = k^{\mu}(\hat{\alpha}\left|\varepsilon_V\right|)^{\mu k_2}\varepsilon_{oct}^{\mu(1-k_2)} \tag{3.11}$$

where $\mu = 1/(1-k_2-k_3)$. Substituting the above equations into the resilient modulus model in Eq. (3.3) results in $C(\theta,\tau_{oct}) = \hat{C}(\left|\varepsilon_V\right|,\varepsilon_{oct}) = \hat{k}\left|\varepsilon_V\right|^{\mu k_2}\varepsilon_{oct}^{\mu k_3}$ where $\hat{k} = (k\hat{\alpha}^{k_2})^{\mu}$. Therefore, the resulting strain-based modulus formulation is equivalent to the original stress dependent resilient modulus model. It is noted that displacement finite element methods can be easily implemented based on the modified universal model in terms of the strain invariants.

The above nonlinear elastic problem is solved using the robust Newton method. The tangent stiffness required for Newton iteration is obtained as follows:

Starting from Eq. (3.6),

$$\frac{\partial \sigma_{ij}}{\partial \varepsilon_{kl}} = \hat{C}(\delta_{ijkl} + \alpha\delta_{ij}\delta_{kl}) + (\alpha\varepsilon_V \delta_{ij} + \varepsilon_{ij})\frac{\partial \hat{C}}{\partial \varepsilon_{kl}}. \tag{3.12}$$

Via a chain rule,

$$\frac{\partial \hat{C}}{\partial \varepsilon_{kl}} = \frac{\partial \hat{C}}{\partial |\varepsilon_V|}\frac{\partial |\varepsilon_V|}{\partial \varepsilon_{kl}} + \frac{\partial \hat{C}}{\partial \varepsilon_{oct}}\frac{\partial \varepsilon_{oct}}{\partial \varepsilon_{kl}} = \mu\hat{C}(\frac{k_2}{\varepsilon_V}\delta_{kl} + \frac{k_3}{3\varepsilon_{oct}^2}\varepsilon'_{kl}). \tag{3.13}$$

By defining $N_{ij} = \varepsilon'_{ij} / \varepsilon_{oct}$, the final form of the tangent stiffness can be expressed as:

$$\frac{\partial \sigma_{ij}}{\partial \varepsilon_{kl}} = \hat{C}[\delta_{ijkl} + (\mu k_2\hat{\alpha} + \alpha)\delta_{ij}\delta_{kl} + \frac{\mu k_3}{3}N_{ij}N_{kl} + \frac{\mu\hat{\alpha}k_3\varepsilon_V}{3\varepsilon_{oct}}\delta_{ij}N_{kl}$$

$$+ \frac{\mu k_2\varepsilon_{oct}}{\varepsilon_V}N_{ij}\delta_{kl}]. \tag{3.14}$$

In the case of axially symmetric analysis, δ_{ijkl}, δ_{ij}, and N_{ij} can be replaced by [1], 4×4 identity matrix of $\{\mathrm{I}\} = [1 \;\; 1 \;\; 1 \;\; 0]^T$, and $\{N\} = 1/\varepsilon_{oct}[\varepsilon'_r \;\; \varepsilon'_\theta \;\; \varepsilon'_z \;\; \varepsilon'_{rz}]^T$ respectively. The Eq. (3.14) can be rewritten as the following simple matrix form:

$$\hat{C}\Big\{[1] + (\mu k_2\hat{\alpha} + \alpha)\{\mathrm{I}\}\{\mathrm{I}\}^T + \frac{\mu k_3}{3}\{N\}\{N\}^T + \frac{\mu\hat{\alpha}k_3\varepsilon_V}{3\varepsilon_{oct}}\{\mathrm{I}\}\{N\}^T$$

$$+ \frac{\mu k_2\varepsilon_{oct}}{\varepsilon_V}\{N\}\{\mathrm{I}\}^T\Big\}. \tag{3.15}$$

3.3 FINITE ELEMENT IMPLEMENTATION

The constitutive equations shown in the previous section can be used for the following finite element formulation. Multiplying a governing differential equation by an arbitrary function and integrating it, the governing differential equation can be converted to the variation form. Letting $\nabla^s \bullet = \frac{1}{2}(\frac{\partial \bullet_i}{\partial x_j} + \frac{\partial \bullet_j}{\partial x_i})$ and denoting : contraction,

$$\int_{\Omega} \nabla^s v : \sigma d\Omega = \int_{\Omega} f \cdot v d\Omega - \int_{\Gamma} g \cdot v d\Gamma \tag{3.16}$$

where f , g , and v are external force, traction on the boundary, and virtual displacement respectively; Ω and Γ are open set in $\Re^d$ (e.g., d=2 or 3) and boundary on Ω respectively. The weak form in Eq. (3.16) can be equivalently expressed in matrix notation as:

$$\underbrace{\int_{\Omega} [B]^T [D][B] d\Omega \{u\}}_{[K]} = \underbrace{\int_{\Omega} [N]^T \{f\} d\Omega - \int_{\Gamma} [N]^T \{g\} d\Gamma}_{\{F\}} \text{ or } [K]\{u\} = \{F\} \tag{3.17}$$

where $[B]$ is the strain-displacement matrix, $[D]$ is the secant matrix in Eq. (3.7), $\{u\}$ is the nodal displacement column vector, $[N]$ is the shape function matrix, $\{f\}$ is the force column vector, and $\{g\}$ is the traction column vector. The nonlinear elastic problem can be solved based on computing the displacement state associated with known loads at $t + \Delta t$.

$$\left[\frac{\partial P}{\partial u}\right]_{t+\Delta t}^{i} \{\Delta u\}^{i+1} = \{F\}_{t+\Delta t} - \{P\}_{t+\Delta t}^{i}$$

$$\{u\}_{t+\Delta t}^{i+1} = \{u\}_{t+\Delta t}^{i} + \{\Delta u\}^{i+1} \tag{3.18}$$

where $[\partial P / \partial u]_{t+\Delta t}^{i}$ is the tangent stiffness equivalent to Eq. (3.14). The above equations used in the Newton-type iteration, for i =1, 2, 3,…, are updated until a tolerance, $\{F\}_{t+\Delta t} - \{P\}_{t+\Delta t}^{i} \le tol.$, is satisfied.

To verify the implementation of the nonlinear universal model for axial compression of an element, an example problem shown in Fig. 3.1 is chosen. As the cylindrical specimen is axisymmetric, the element represents the cross-section in the r-z plane. The element is subjected to the vertical stress, g_z , is incrementally increased. It

is easy to derive an analytical solution in this case by utilizing MATLAB software based on the nonlinear elastic constitutive equation of the universal model. In Figs. 3.2.a, 3.2.b, and 3.2.c, the finite element results are compared with the analytical solutions. The finite element prediction and the analytical solution are almost identical, thus verifying the correct implementation of the universal model.

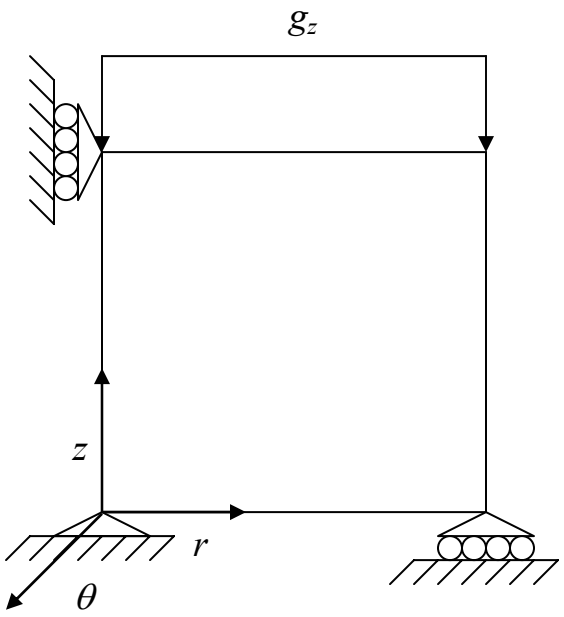

Figure 3.1 An Example for Validation ($k_1 = 200.0$ and $k_3 = -0.43$)

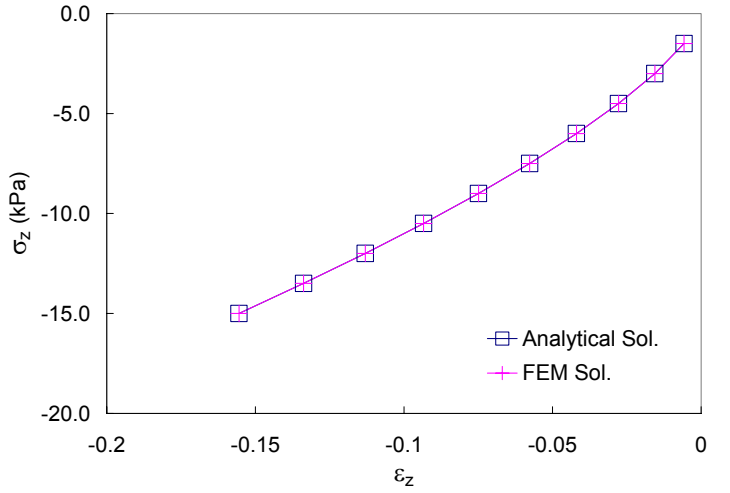

(a)

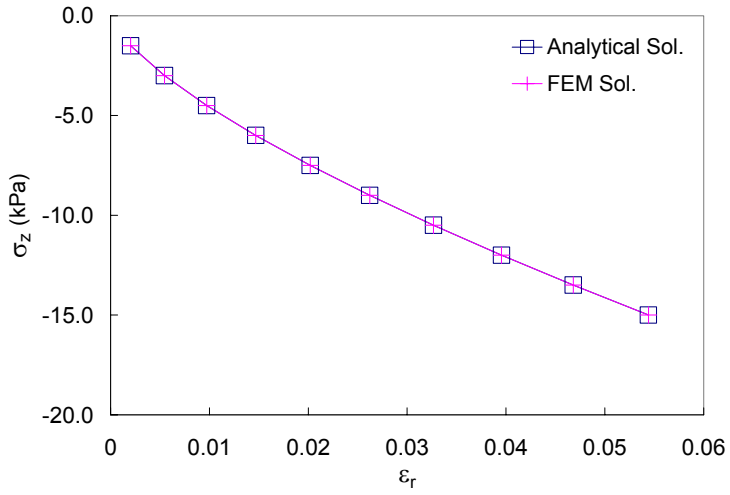

(b)

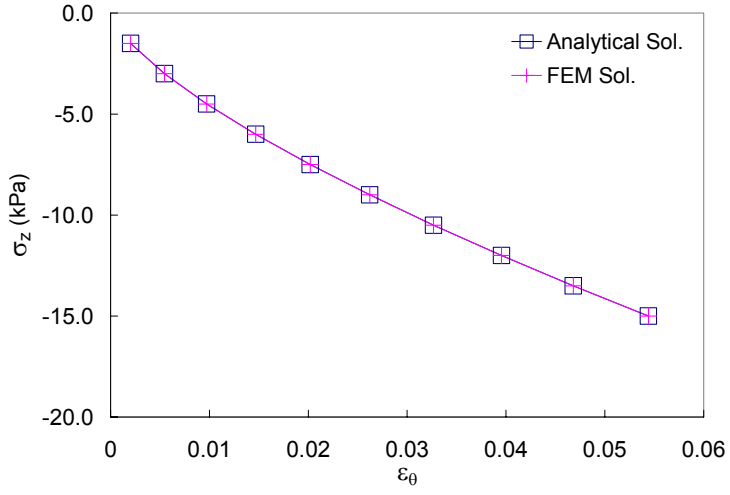

(c)

Figure 3.2 Axial Stress History and Strain Responses: (a) Axial, (b) Radial, and (c) Circumferential Strain

3.4 FINITE ELEMENT SIMULATION

The finite element program with the universal model is used in this section to simulate the stress-strain behavior of various soils under the laboratory triaxial resilient modulus tests. Two types of soils are evaluated, granular soils and fine-grained soils.

For granular soils, the resilient modulus data reported by Santha (1994) are used. He tested samples having a diameter of 73 mm and a height of 142.2 mm according to AASHTO T 274-82 and reported the coefficients in the universal model for numerous types of soils. In addition to the triaxial data, Santha reported California Bearing Ratio (CBR) as an indicator for the stiffness of granular soils.

For fine-grained soils, the triaxial resilient modulus data from Thompson and Elliott (1985) were used. They determined the value of resilient modulus using a bilinear method discussed in Huang (1993). This method describes the relationship between deviatoric stress and resilient modulus and can be regressed using the universal model to obtain the required material parameters. As the soils are cohesive the value for k_2 (related to the bulk stress influence) is taken as zero. The regression curves are shown in Fig. 3.3 as a function of soil stiffness categories (e.g., soft, medium and stiff).

Table 3.1 presents the parameters selected from the work of Santha for granular materials and the regression analyses shown in Figure 3.3 based on the work of Thompson and Elliott for the fine-grained soils. Incrementally increasing the vertical stress and assuming that the increase in the horizontal stress is 25% of that value, these coefficients are used in the finite element program to simulate the stress-strain behavior of specimens monotonically loaded with confining stresses from 6.89 to 135.75 kPa and deviatoric stresses from 24.7 to 494.25 kPa. The resulting compressed stress-strain

behavior of the three granular soils and three fine-grained soils are shown in Figs. 3.4 and 3.5 respectively.

In both figures, the stiffnesses of different soils estimated from the slope of the stress-strain curves are in good agreement with the stiffness characteristics (e.g., CBR) of those soils reported by Santha and Thompson and Elliott. The curvatures of the granular and fine-grained soils observed in Figs. 3.4 and 3.5 are also consistent with the material properties summarized in Table 3.1. Thus, the stronger negative values of k_3 in the fine-grained soils cause the resilient modulus to decrease as the deviator stress increases and are the reason for the decreasing slope of the curves in Fig. 3.5. However, this effect is lessened in Fig. 3.4 with the granular soils because k_3 coefficients are smaller in an absolute term and also positive k_2 coefficients cancel the effect of k_3 term.

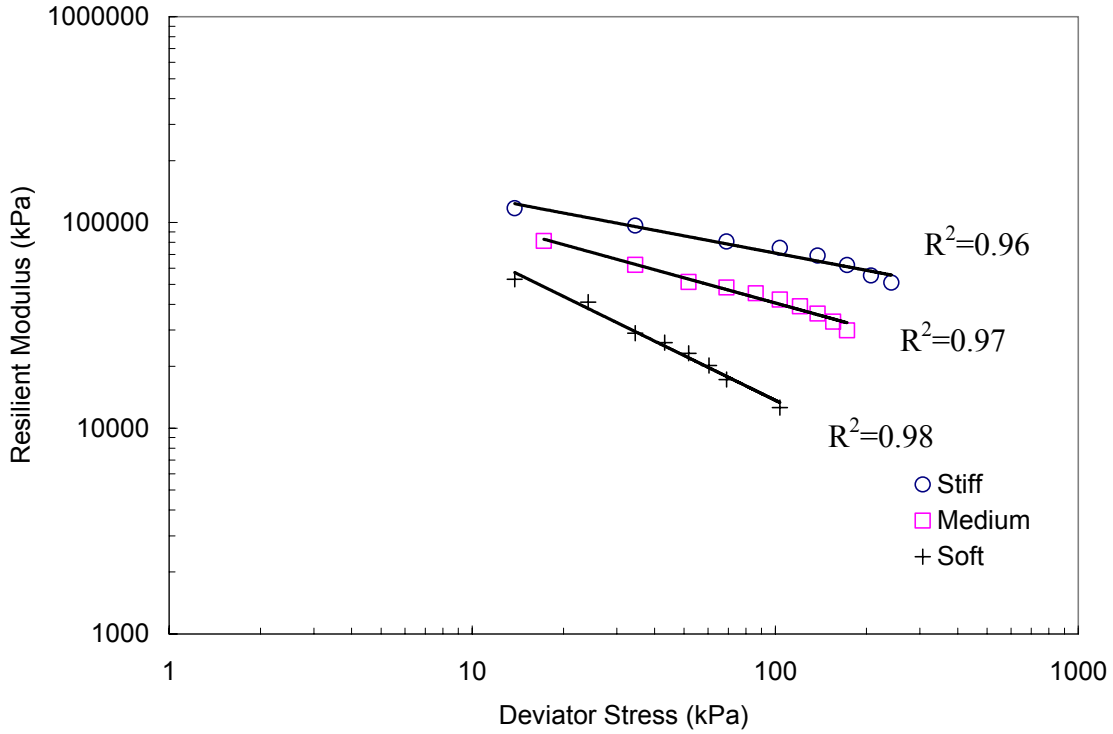

Figure 3.3 Resilient Modulus-Deviator Stress Relationship for Three Types of Fine-Grained Soils

Table 3.1 Chosen Properties of Granular Materials and Fine-Grained Soils

Granular Materials				Fine-Grained Soils		
CBR	k_1	k_2	k_3	Type	k_1	k_3
4.3	173	0.412	-0.403	Soft	134	-0.722
9.8	241	0.379	-0.319	Medium	398	-0.406
13.5	354	0.484	-0.403	Stiff	697	-0.278

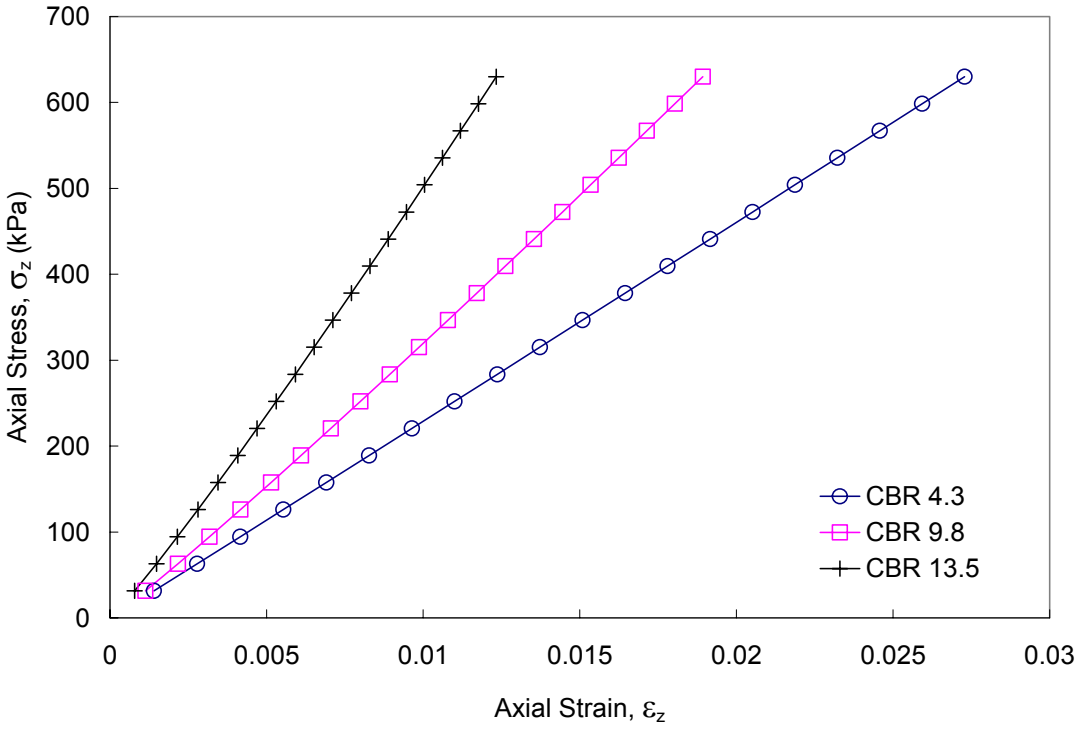

Figure 3.4 Computed Stress-Strain Curves of Granular Soils under Incremental Loads

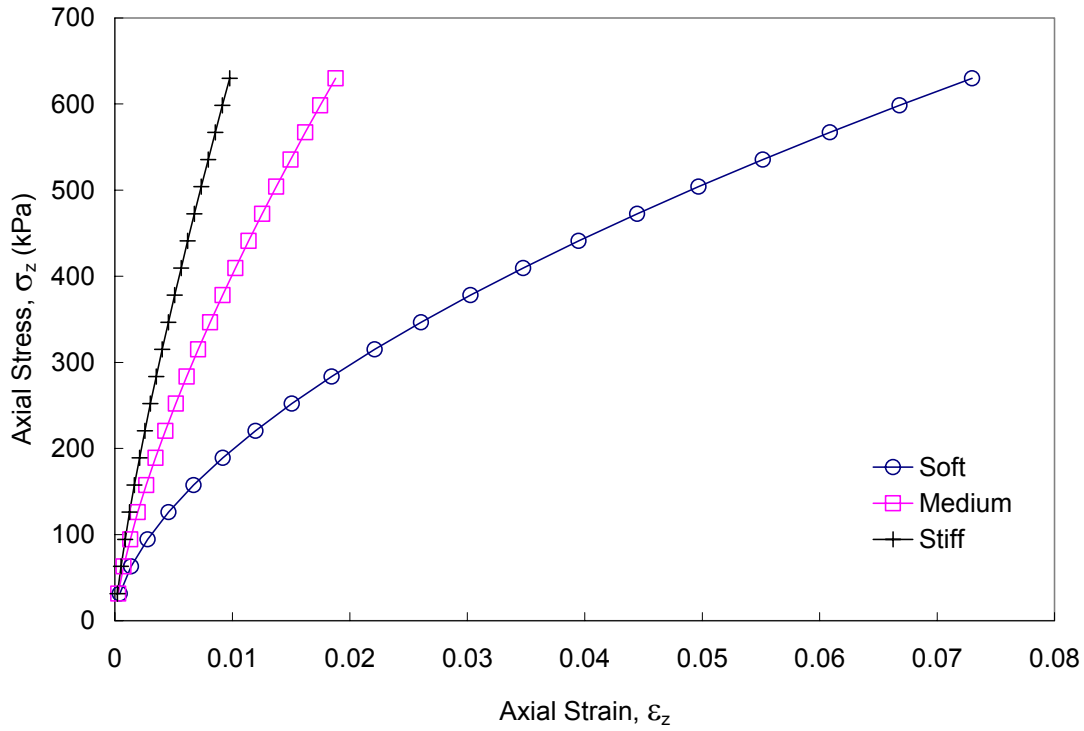

Figure 3.5 Computed Stress-Strain Curves of Fine-Grained Soils under Incremental Loads

CHAPTER 4

FINITE ELEMENT DISCRETIZATION OF PAVEMENT STRUCTURE

This chapter contains a finite element (FE) mesh discretization procedure for a multi-layered pavement structural analysis. With the aim of obtaining economic FE models that result in acceptable accuracy, an error estimator was developed that gives a guidance in refining the mesh until the desired accuracy is achieved. This estimator is based on the works of Zienkiewicz and Zhu (1987, 1992, 1995) that utilize the stress recovery (smoothing) technique. They introduced a measure of the solution error as the difference between unsmooth stresses obtained from FE analysis and smoothened stresses after post processing. In this work, the stress-smoothing technique and Z-Z estimator was implemented into VECD-FEP++. In addition to considering that Z-Z estimator in its original form, which is not valid for heterogeneous materials, the error estimator was extended to layered pavement system that involves discontinuous stresses at interfaces. In the following sections, work involved in developing the error estimator used for a layer media and modification for a layered pavement structure is described.

4.1 Error Estimator for Homogeneous Media

The accuracy of FE approximate solutions in pavement structures needs to be evaluated by error estimators. The error measurement due to FE spatial discretization can be characterized by the following normalized error norm:

$$\Delta e_{\sigma} = \sqrt{\int_V \left(\sum_{i=1}^{4} \left| \sigma_i^* - \sigma_i^h \right|^2 \right) dV} \Bigg/ \sqrt{\int_V \left(\sum_{i=1}^{4} \left| \sigma_i^* \right|^2 \right) dV} \tag{4.1}$$

where the single indexed stress components, σ_i, in axisymmetric analysis are defined in terms of their respective tensor components as follows:

$\sigma_1 = \sigma_r$ (radial stress), $\sigma_2 = \sigma_\theta$ (circumferential stress), $\sigma_3 = \sigma_z$ (axial stress), and $\sigma_4 = \tau_{zr}$ (shear stress). (4.2)

As shown in Fig. 4.1, the normalized error norm can be calculated at the integration (Gauss) points using the following steps:

1. The stress components σ_i^h at integration points are extrapolated to nodal points.
2. The discontinuous nodal stresses across element edges are averaged by taking into account the stress contribution from each element.
3. The recovered stresses σ_i^* at integration points can be determined by interpolating the averaged stresses at the nodal points into the integration points.
4. The normalized error norm in Eq. (4.1) can be estimated using the recovered stresses σ_i^* and the stresses σ_i^h of FE results at integration points as follows:

$$\Delta e_\sigma = \frac{\left[2\pi r \det(J) \sum_{n=1}^{2} \sum_{m=1}^{2} w_n w_m \left(\sum_{i=1}^{4} \left| \sigma_i^* - \sigma_i^h \right|^2 \right) \right]^{1/2}}{\left[2\pi r \det(J) \sum_{n=1}^{2} \sum_{m=1}^{2} w_n w_m \left(\sum_{i=1}^{4} \left| \sigma_i^* \right|^2 \right) \right]^{1/2}} \tag{4.3}$$

where w_n and w_m are weight factors. In the above, 2×2 Gauss quadrature is used for the purpose of numerical integration. If the estimate of an error at a nodal point is desired, the error can simply be averaged over the adjacent elements as follows:

$$\Delta e_\sigma = \frac{\sum_{e=1}^{4} \left(\sum_{i=1}^{4} \left| \sigma_i^* - \sigma_i^h \right|^2 \right)}{\sum_{e=1}^{4} \left(\sum_{i=1}^{4} \left| \sigma_i^* \right|^2 \right)}. \tag{4.4}$$

The above procedure is illustrated using finite element analysis of a plate-with-a-hole problem, as shown in Fig. 4.2. It can be clearly seen that the estimate of the error reduces as the mesh is refined.

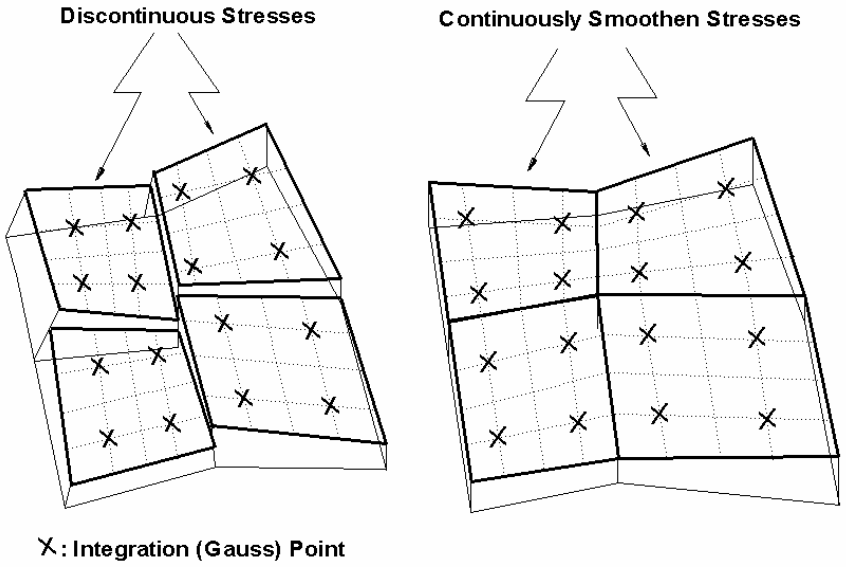

Figure 4.1 Illustration of Stress Recovery Technique

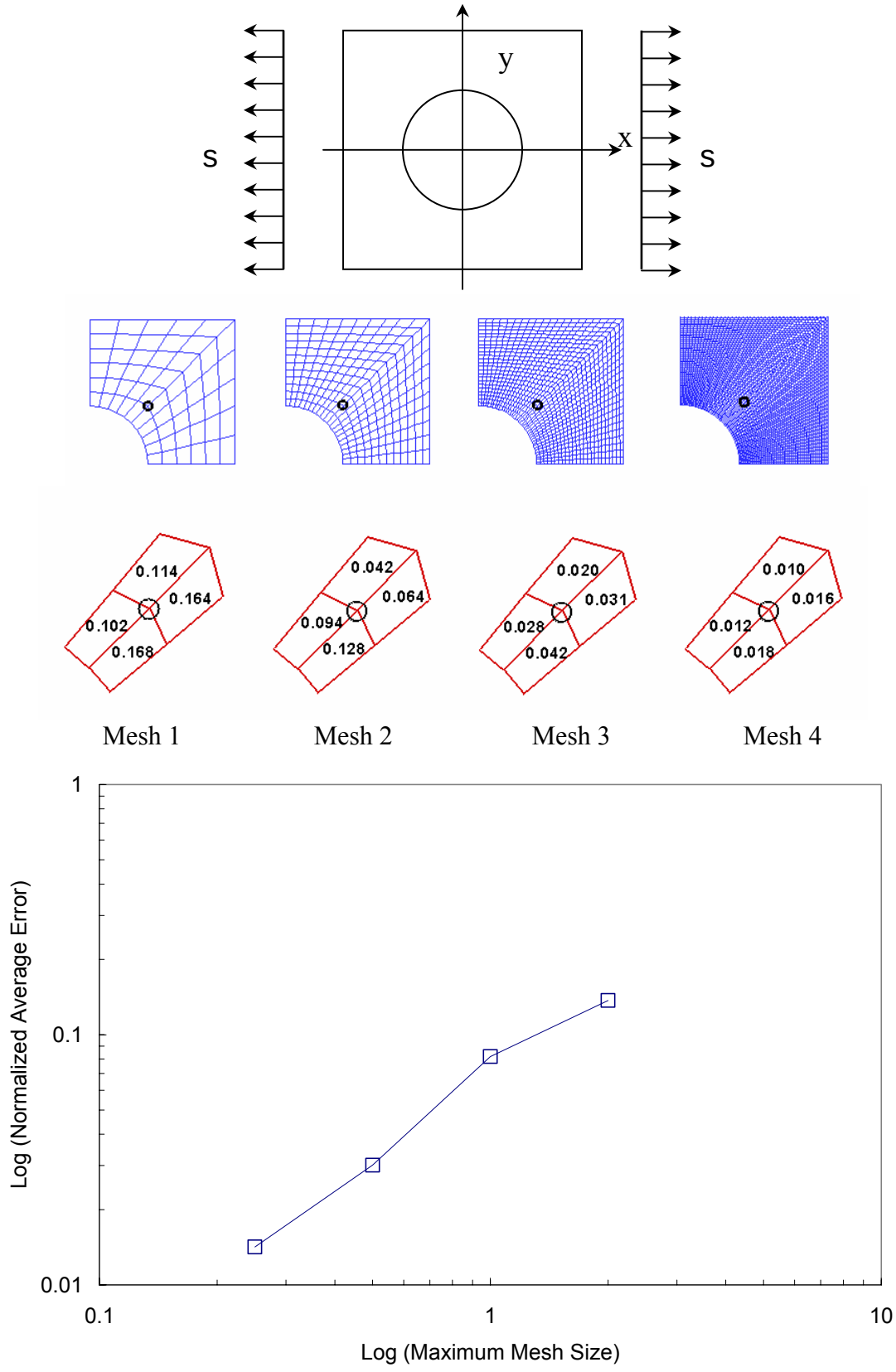

Figure 4.2 Finite Medium Example of Circular Hole in Uniaxial Tension

4.2 Error Estimator for Multi-layered Systems

Determining an error estimator for a multilayered (Fig. 4.2) pavement system needs additional care, which is required due to discontinuous material stiffnesses causing stress discontinuity at the interface between the layers. Fig. 4.3 shows the idealized problem of a typical loading function and a representative FEM grid. The axial and shear stresses (σ_3 and σ_4) are continuous across the interfaces, while the radial and circumferential stresses (σ_1 and σ_2) could be discontinuous. Instead, the strains (ε_1 and ε_2) are continuous. For this reason, we smoothen σ_3, σ_4, ε_1, and ε_2 to obtain σ_3^*, σ_4^*, ε_1^*, and ε_2^*. The error in the solution is then expressed in terms of the difference between original and smoothened solution as follows:

$$\Delta e_\sigma = 0.5\left(\frac{\sqrt{\sum_{i=3}^{4}\left|\sigma_i^* - \sigma_i^h\right|^2}}{\sqrt{\sum_{i=3}^{4}\left|\sigma_i^*\right|^2}} + \frac{\sqrt{\sum_{i=1}^{2}\left|\varepsilon_i^* - \varepsilon_i^h\right|^2}}{\sqrt{\sum_{i=1}^{2}\left|\varepsilon_i^*\right|^2}} \right) \tag{4.5}$$

In order to investigate the use of this error estimator, the responses of the pavement section shown in Fig. 4.3 under the applied time load of 40 kN are analyzed. Fig. 4.4 shows the discontinuity across material intersections. Fig. 4.5 shows continuity in axial and shear stresses that occur at each of the material boundary interfaces. Fig. 4.6 shows the actual grid used for analyzing the 24 locations chosen for investigating the error caused by the discontinuities. Points 1 to 8 are selected at the top and mid-depth AC layer and points 9 to 12 are chosen at the interface between the AC and base layers. Points 13 to 16 are mid-depth in the base layer and 17 to 20 are the interface between the base and subgrade layers. Finally, points 21 to 24 are located at the depth of 2m from the interface between base and subgrade.

Using the smoothing technique described in Section 4.1 and the error calculation scheme shown in Fig. 4.1, the normalized error according to Fig. 4.6 was calculated. Those values for each of the reference points are plotted as a function of mesh size in Figs. 4.7 to 4.9 for the AC, base and subgrade layer, respectively.

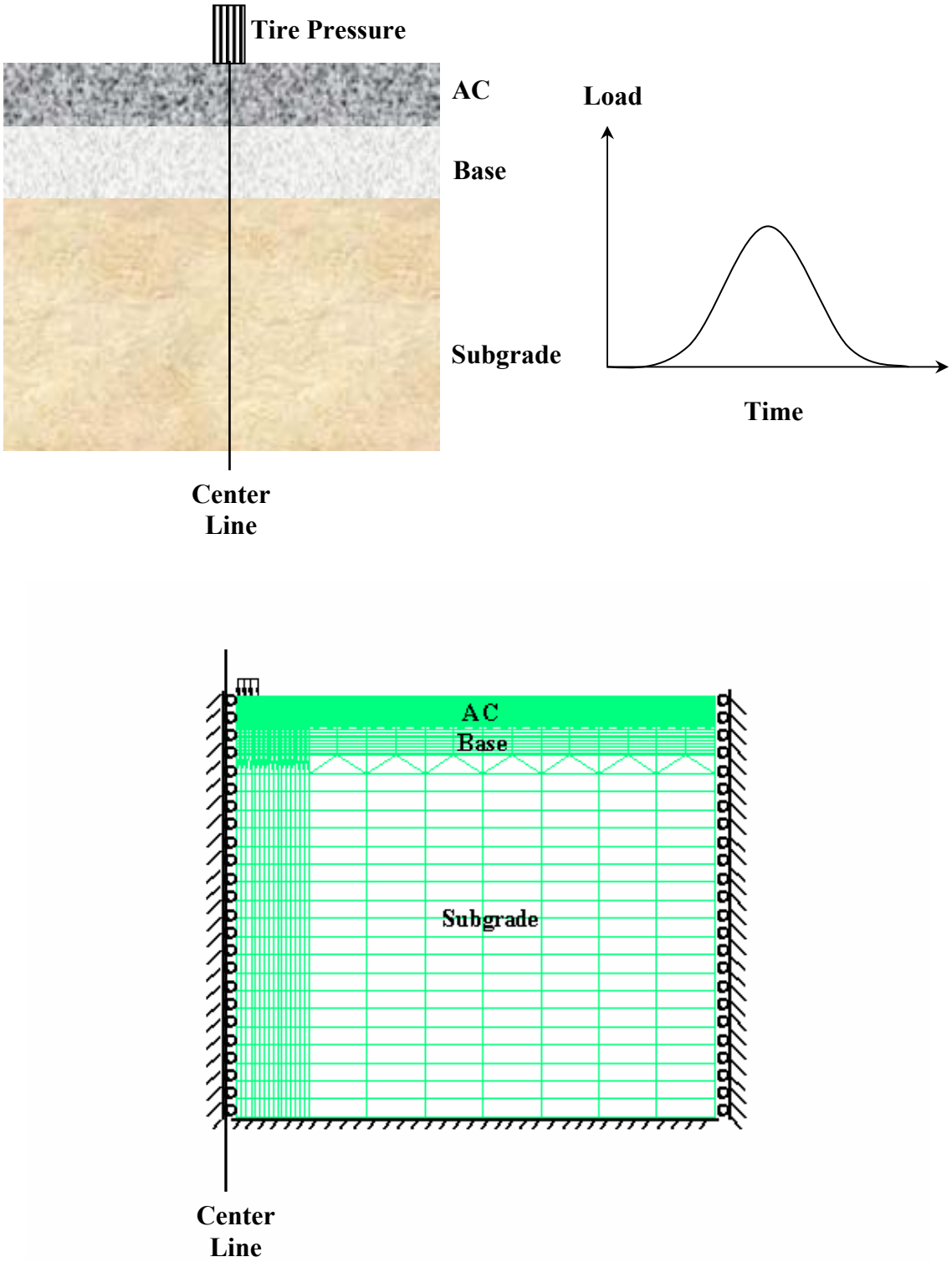

Figure 4.3 Axisymmetric Pavement Structure Modeling Subject to Cyclic Loadings

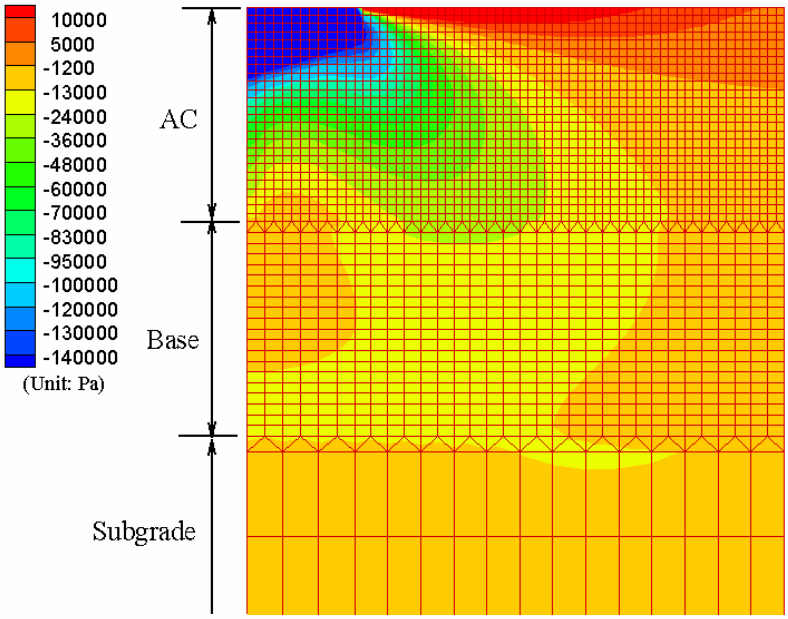

(a)

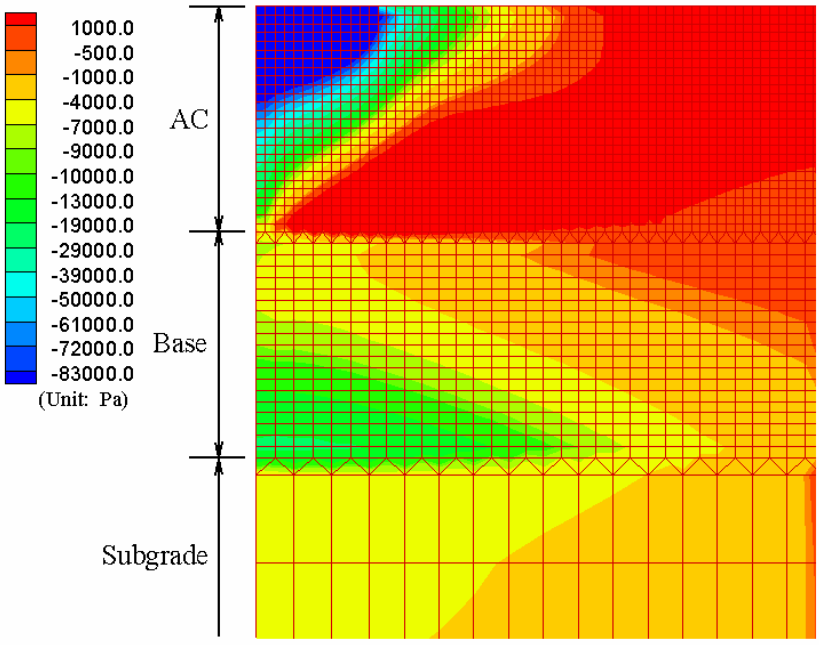

(b)

Figure 4.4 Stress Discontinuity: (a) Radial Stress; (b) Circumferential Stress

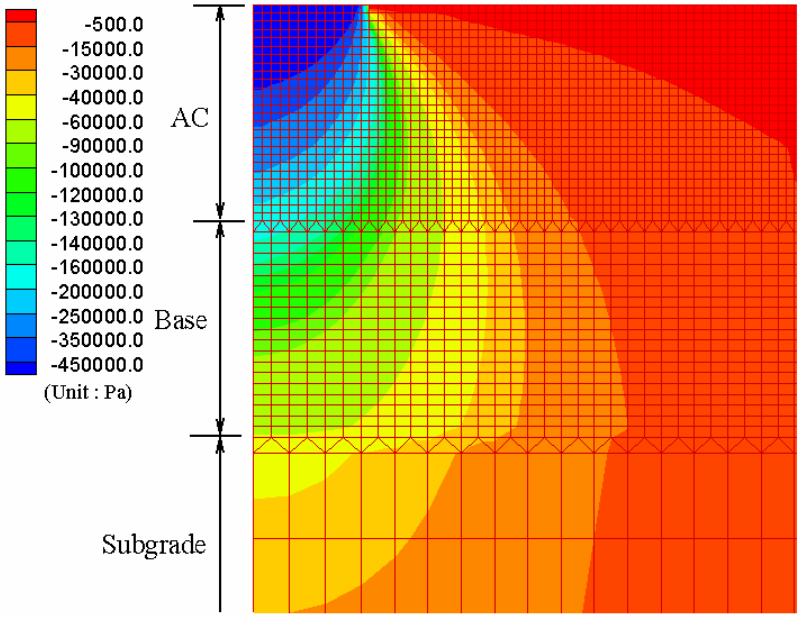

(a)

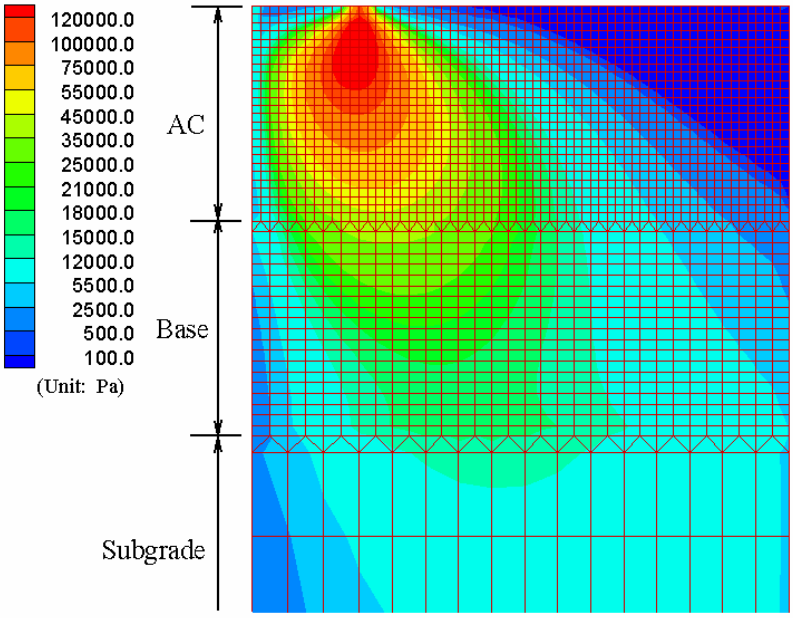

(b)

Figure 4.5 Stress Continuity: (a) Axial Stress; (b) Shear Stress

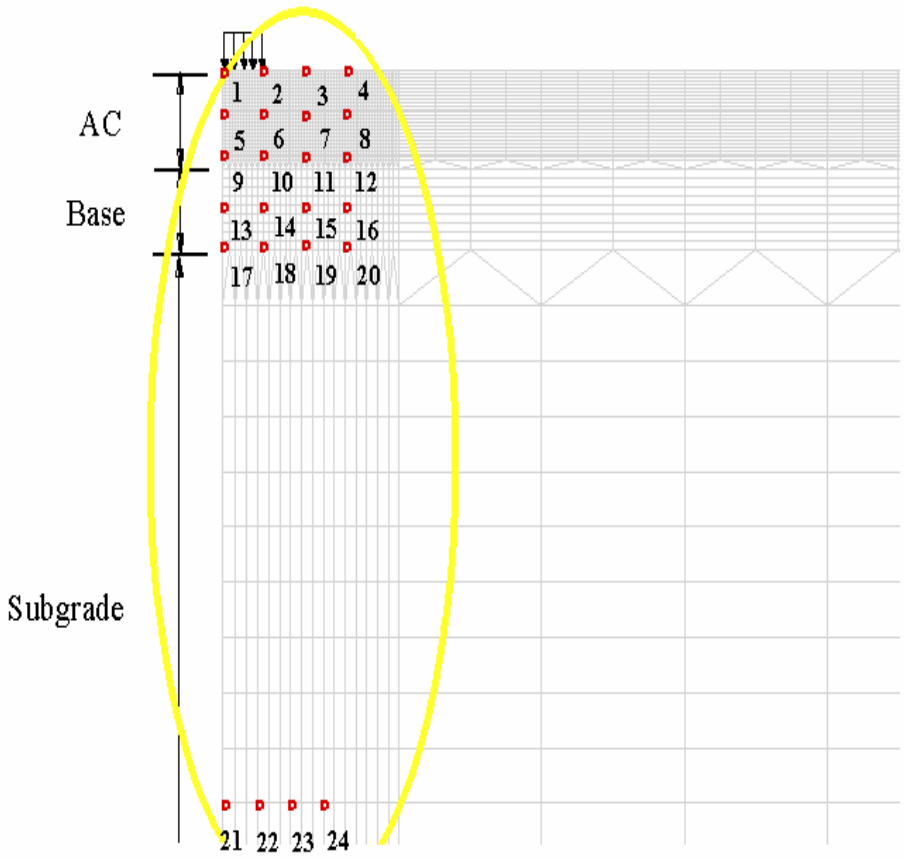

Figure 4.6 Chosen Locations for Checking the Normalized Error Norms

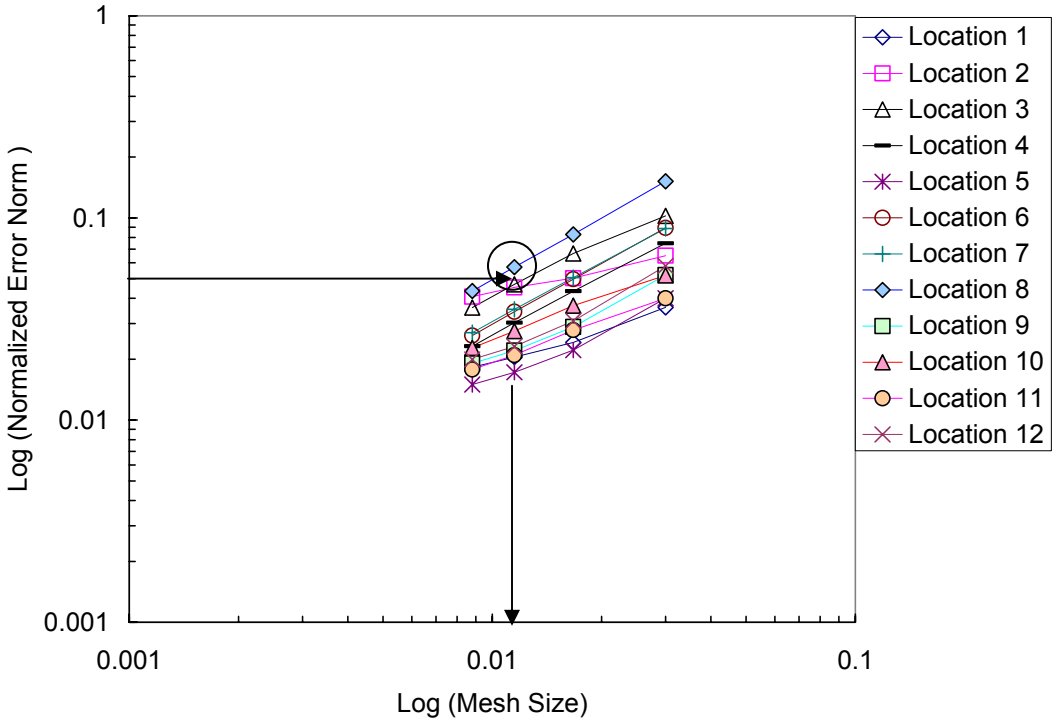

Figure 4.7 Convergence of the Normalized Error Norm in an AC Layer

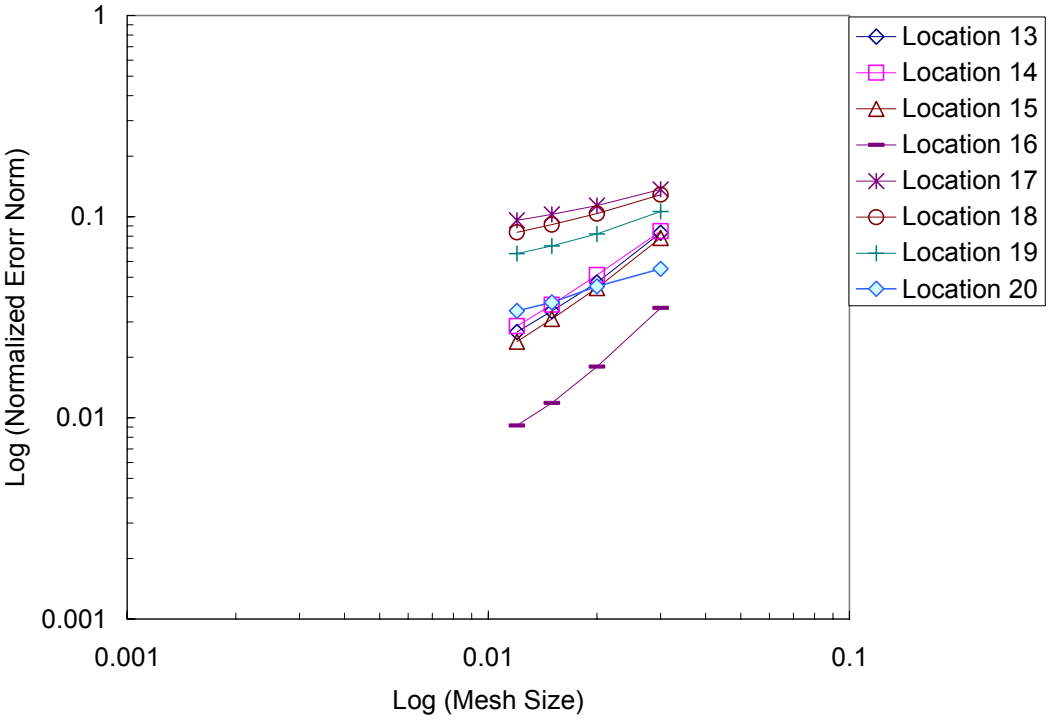

Figure 4.8 Convergence of the Normalized Error Norm in a Base Layer

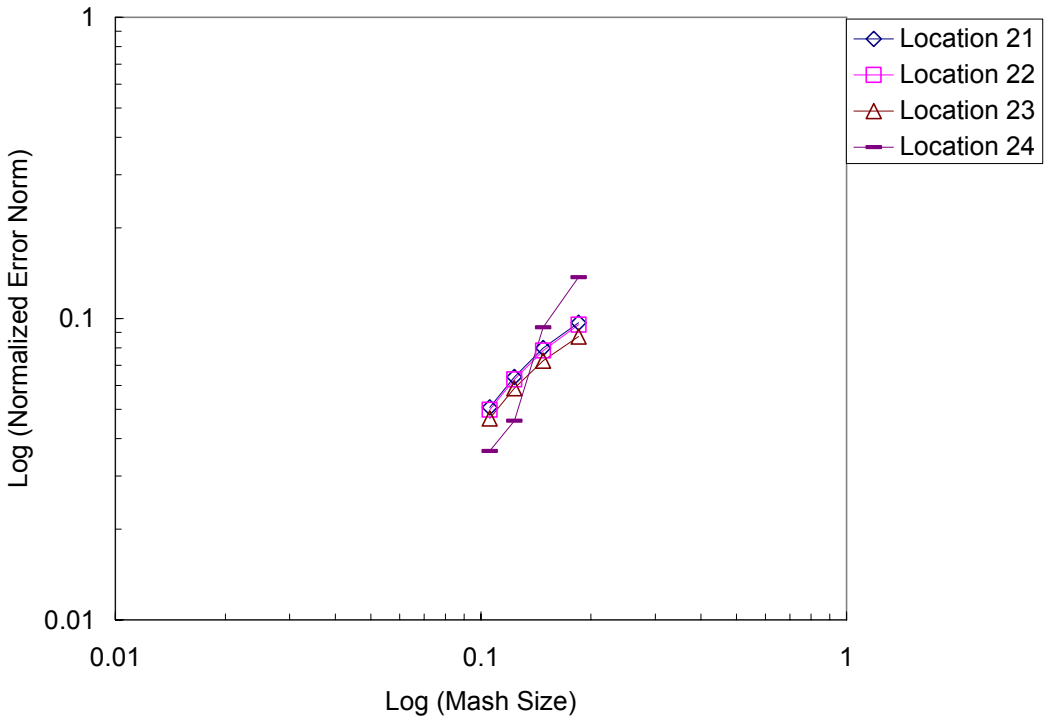

Figure 4.9 Convergence of the Normalized Error Norm in a Subgrade Layer

4.3 Summary

In this chapter, an error estimator based on stress-smoothing that can be used to define the mesh size to produce a given level of error has been presented. Considering the inexact nature of material properties and loading conditions, an error of 5% in the AC layer is assumed to be sufficient and the mesh is chosen according to this error tolerance. Thus the mesh size is selected from Fig. 4.7 when the error estimate is equal to 5% (0.05). The resulting mesh is used for further analysis of damage evolution in the next chapter.

CHAPTER 5

STUDY OF CRACK INITIATION MECHANISMS IN ASPHALT PAVEMENTS USING VECD-FEP++

This chapter documents the findings from the study of failure mechanisms of fatigue cracking in asphalt pavements using the finite element program that employs the viscoelastic continuum damage model for asphalt layer and a nonlinear elastic model for unbound layers. Both bottom-up and top-down cracks are investigated by taking several important variables into account, such as asphalt layer thickness, layer stiffnesses, pressure distribution under loading, and load levels applied on the pavement surface. The crack initiations in different pavement structures under different loading conditions are studied by monitoring a damage contour. The developed finite element code, called VECD-FEP++, employs the viscoelastic continuum damage model as the constitutive model of asphalt concrete and the universal model (or so-called Uzan-Witczak resilient modulus model) for unbound materials. The finite element analysis of various pavement-load combinations showed significantly different failure mechanisms. Details on the VECD-FEP++ and the findings are given in the following sections.

5.1 OVERVIEW

Fatigue cracking is one of the major distress modes affecting the performance of flexural pavements. A traditional approach to dealing with fatigue cracking is based on the assumption that cracks initiate at the bottom of the asphalt layer due to tensile stresses developed from the flexure of the layer and propagate to the pavement surface under repeated load applications (so-called bottom-up cracking). However, recent field studies

also suggest that fatigue cracks can also initiate at the pavement surface and propagate downward under traffic (so-called top-down cracking). Myers et al. (2001) used the linear elastic finite element analysis to conclude that the major cause of the top-down cracking is due to tensile stresses resulting from the interaction between truck tires and pavement surface.

In order to accurately determine the initiation location and cause of the fatigue cracking, it is imperative to use realistic constitutive models for different pavement layers because the cracking behavior of asphalt concrete is closely associated with the stress-strain response of the material. These constitutive models have to be fundamental in nature so that various conditions encountered during the pavement service life may be accounted for, including temperature, aging, rate of loading, loading time, and rest time. Well-established theories in the discipline of mechanics of materials are available for this task. Another requirement is a structural model (or pavement response model) that computes stresses and strains in pavement structures under varying boundary conditions and loading types.

In recent years, there has been some success in developing a mechanistic constitutive model of asphalt concrete. Kim et al. (1997) developed a uniaxial viscoelastic continuum damage model by applying the elastic-viscoelastic correspondence principle to separate out the effects of viscoelasticity and then employing internal state variables based on the work potential theory to account for the damage evolution under cyclic loading and the microdamage healing during rest periods. From the verification study, it was found that the constitutive model has the ability to accurately predict the stress-strain behavior of asphalt concrete under varying loading

rates, random rest durations, multiple stress/strain levels, and different modes of loading (controlled-stress versus controlled-strain). A continued effort in refining this model resulted in the work by Daniel and Kim (2002) in which a unique damage characteristic curve was discovered regardless of the applied loading conditions (cyclic versus monotonic, amplitude/rate, and frequency). This characteristic curve describes the reduction in material integrity as damage grows in the asphalt concrete specimen. In addition, Chehab et al. (2002) demonstrated that the time-temperature superposition is valid not only in the linear viscoelastic state, but also with growing damage. This finding allows the prediction of mixture responses at various temperatures from laboratory testing at a single temperature. The damage characteristic curve and the time-temperature superposition with growing damage are the foundation of the viscoelastic continuum damage (VECD) model employed in this study.

One of the most widely accepted constitutive model for unbound materials is the universal model (Witczak and Uzan, 1988). This model describes the nonlinear stress-strain characteristics of cohesive and granular soils by expressing the resilient modulus as a function of stress state. The universal model was implemented into VECD-FEP++ finite element program.

The resulting VECD-FEP++ finite element program is used in simulating various pavement structures under different loading conditions for the study of the fatigue failure modes in asphalt pavements. The findings from this parametric study are discussed in the following section.

5.2 STRUCTURES, MATERIAL PROPERTIES, AND LOADING CONDITIONS

In this study, flexible pavements comprised of asphalt layer, aggregate base, and subgrade are selected for the investigation. The pavement structures used in this study are summarized in Table 5.1. The layer thicknesses in this table are selected from the DataPave 3.0 such that a wide range of realistic pavement structures is covered. The base thickness was held constant at 50 cm and an infinite subgrade was selected.

Table 5.1 also shows the material properties used in this study. The Prony series constants and a damage function were obtained from the experimental study of Chehab et al. (2002) in which Maryland 12.5 mm Superpave mix was tested in uniaxial tension. The base and subgrade material parameters of the nonlinear universal model were found in Santha (1994) and Garg et al. (1998).

A moving load was represented by the haversine load with a peak magnitude of 40 kN and 20 kN to simulate a single and dual tire loads respectively. A loading duration of 0.03 second and a rest period of 0.97 second were selected. For a tire-pavement contact pressure distribution on pavement surface, both uniform and non-uniform contact pressure distributions were studied. The uniform contact pressure has been most widely used for pavement response evaluation. However, recent studies (Siddharthan et al., 2002) have revealed that the contact pressure is non-uniform and the effect of the non-uniform distribution of the contact pressure is important in accurate pavement response computation. For the non-uniform tire pressure, the tire pressure measured by Sebaaly and Tabatabaee (1993) was selected in this study.

5.3 Analysis of Crack Initiation Mechanisms

The research performed in this study focused on investigating the fatigue failure mechanism(s) of top-down and bottom-up crack modes by monitoring the state of stresses and structural damage traced by a damage parameter. Fig. 5.1 presents a stress-strain relationship and the characteristic damage curve obtained from a constant-crosshead-rate monotonic testing of the Maryland Superpave mixture (Chehab et al., 2002). In their study, it was found that soon after the peak of the stress-strain curve, localization occurs and macrocracks start to develop. After this point, the normal strain calculated from the displacements measured by the LVDTs is not meaningful any more and deviations from the characteristic damage curve start to appear.

The damage function shown in Table 5.1 represents the damage characteristic curve before significant localization. Therefore, the damage contours obtained from the VECD-FEP++ indicate mostly the damage accumulated during the crack initiation stage. This feature is quite different from typical finite element analysis based on fracture mechanics, such as the studies done by Jenq et al. (1993) and Myers et al. (2001). In their studies, a crack was introduced before the load was applied and critical stresses that contribute most to the crack propagation were identified. The approach taken in this study allows the investigation of location and mechanisms of microcracks during the macrocrack initiation stage without any artificial cracks in the pavement structure.

In this study, the pavement structure is modeled by an axisymmetric finite element model shown in Fig. 5.2. Fig. 5.3a shows radial stress-strain curves under the uniform contact pressure in cyclic mode. The hysteresis loops shifted to the right side demonstrating the accumulation of radial strains in tension. Fig. 5.3b presents the

damage contours at different number of cycles. It is noted that the intensity of damage increases as the number of cycles increases. Another observation to be made in this figure is that the pattern of damage contour (i.e., shape and relative intensities of damage at different locations) remains relatively the same at different cycles. This observation is important in this study because of the computing time required in simulating long-term fatigue behavior. Simulation of the cyclic behavior of asphalt pavements using the VECD-FEP++ takes between 5 and 7 seconds per cycle on a 1.8 MHz Pentium IV computer with 512 MB memory, and the simulation of 1000 cycles takes about 1.4 to 2 hours. Based on this rate, one million cycles will take about 1,400 to 2,000 hours. In this study, the stress and damage contours at the peak load of the 10^{th} cycle are used in the evaluation of the crack initiation mechanisms. Comparison of the contours at the 10^{th} cycle yields pretty much the same conclusions as those made from longer cycles.

Various pavement structures with changing layer thicknesses, layer stiffnesses, contact pressure distributions, and load levels were modeled using the VECD-FEP++ program. Combinations of these variables are selected such that effects of individual variables on stress and damage states can be evaluated effectively. Values selected for each variable are summarized below and in Table 5.1:

1. AC layer thickness: 7.6, 17.8, 30.5, and 43 cm (3, 7, 12, and 17 inches), referred as thin, medium, thick I, and thick II respectively;
2. AC stiffness: AC I for softer asphalt mix and AC II for stiffer asphalt mix;
3. Base and subgrade stiffnesses: full factorial combinations of stiff and weak base and stiff and weak subgrade, i.e., stiff base and stiff subgrade (referred as

MODULUS SS), stiff base and weak subgrade (MODULUS SW), weak base and stiff subgrade (MODULUS WS), and weak base and weak subgrade (MODULUS WW);

4. Uniform and non-uniform contract pressure distributions; and
5. Load levels of 20 and 40 kN.

Figs. 5.4 to 5.13 show the contours of damage and stresses that are computed at the peak load of the 10th cycle for all the pavement structures and loading conditions selected in this study. Figs. 5.4 to 5.12 are generated using the soft asphalt stiffness (i.e., AC I) only, and the effect of asphalt layer stiffness is separately shown in Fig. 5.13.

In all the figures, the following general observations can be made regarding the stresses:

1. The radial stress is in tension at the bottom of asphalt layer and in compression at the top of the AC layer;
2. The shear stress is the greatest between the one third and one quarter-depth of the AC layer right under the tire edge; and
3. Axial compressive stress contour shows the largest stress in the loading center with a decreasing magnitude as the depth increases.

In the following, detailed evaluation of the effects of the individual variables on stress and damage states is given.

5.3.1 Effect of AC Thicknesses

Other than the general observations on the stress state listed above, two additional conclusions can be made from Figs. 5.4 to 5.11. First, the location where the largest shear stress occurs moves from the mid-depth to shallower locations as the AC layer

thickness increases. It is noted that the maximum shear stress location is the mid-depth of the AC layer until the AC layer thickness reaches about 15 cm (6 inches). For the AC layer thicknesses greater than 15 cm (6 inches), the maximum shear stress occurs around 7.6 to 10 cm (3 to 4 inches) deep from the pavement surface regardless of the AC layer thickness. This observation supports findings from many field studies that the rutting in the AC layer, which is mainly caused by the shear flow in the mix, is originated from top 7.6 to 10 cm (3 to 4 inches) in the layer. Larger shear stresses and higher pavement temperatures during the daytime near the pavement surface may be the reason for greater permanent deformation in this region compared to deeper locations in the layer.

The other important observation is that the level and location of damage are greatly affected by the AC layer thickness. In Figs. 5.4 to 5.11, the damage values decrease significantly as the AC layer thickness increases. For example, the increase of the AC layer thickness from 3 inches to 7 inches (Figs. 5.4 and 5.5) results in the decrease in the damage level by about 70 times. Another important observation is the change in the location of crack initiation as a function of the AC layer thickness. When the thinnest layer is modeled in Figs. 5.4 and 5.8, all the damage is found at the bottom of the layer and there is comparatively less damage at the top of the AC layer. The large damage at the top of the AC layer shown in Figs. 5.4 and 5.8 is due to the fact that the work potential is insensitive to the sign of loading, i.e., it is the same in tension and in compression. Therefore, the large damage at the top of the AC layer in these figures should not be considered in our interpretation of the results. As the AC layer becomes thicker, damage right under the tire edge starts to show up. In the thickest AC layer of 43 cm, the intensity of damage under the tire edge is greater than that at the bottom of the

AC layer. This observation above supports the findings from the field studies regarding the top-down cracking (Gerritsen et al. (1987); Groenendijk et al. (1997a)); that is, the top-down cracks are found in asphalt pavements with an asphalt layer thicker than 25 to 30 cm (10 to 12 inches).

5.3.2 Effect of Base and Subgrade Moduli

The effect of base and subgrade moduli can be evaluated by comparing four sub-figures under each response parameter in each figure. First of all, it is found that the effect of subgrade modulus on stress and damage states is much less than the effect of base modulus. Also, the effect of base modulus becomes less as the AC layer becomes thicker. Regarding the crack initiation location, the weaker base increases the intensity of damage under the tire edge more than it does at the bottom of the AC layer and therefore increases the probability of top-down cracking. The comparison of the stress and damage contours presented in Figs. 5.4 to 5.11 yields the conclusion that the subgrade modulus has less effect on the stresses and damage in the AC layer than the base modulus. The stiffer base resulted in less damage, and this trend was more evident in the damage under the tire edge.

5.3.3 Effect of Contact Pressure Distributions

Sebaaly and Tabatabaee (1993) presented the non-uniform contact pressure distribution measured from a moving surface load. Figs. 5.4 to 5.7 are the results from the uniform contact pressure and Figs. 5.8 to 5.11 are from the non-uniform contact pressure distribution. One interesting observation that can be made from the comparison

of the figures is that the non-uniform pressure distribution results in larger stresses and greater amount of damage in all the conditions. For example, Fig. 5.9 with the non-uniform contact pressure shows much greater damage under the tire edge than Fig. 5.5 with the uniform contact pressure. This difference suggests that the pavement responses calculated from the traditional way of handling the tire pressure being uniform may underestimate the actual values in the field and therefore overestimate the pavement service life. Also, it needs to be noted that the contribution of top-down cracking to the overall cracking in the AC layer becomes greater under the non-uniform pressure than under the uniform pressure. Regarding the fact of underestimating the actual service life, Groenendijk et al. (1997a) presented that the non-uniform contact pressure could cause large horizontal tensile stresses at the pavement surface at the edge of the loading contact.

Another interesting phenomenon to be noted in Figs. 5.9 to 5.11 is the bi-modal pattern of cracking; that is, cracks initiate from both top and bottom of the AC layer. The conjoined damage contours from the top and bottom of the AC layer suggest that the through-the-thickness crack may develop as these bottom-up and top-down cracks propagate further and coalesce together. Gerritsen et al. (1987) reported from their study of field cores that they found cores with top-down cracking for about 10 cm (4 inches), about 5 cm (2 inches) with no cracking at all, and about 10 cm (4 inches) bottom-up cracking in the same core. The conjoined damage contours in Figs. 5.9 to 5.11 explains the reason behind this observation from field cores. This finding clearly demonstrates the problem associated with the traditional approach to fatigue performance prediction in which the tensile strain at the bottom of the AC layer is related to the fatigue life of the

pavement. This approach cannot account for the additional crack growth from the top of the pavement and therefore will overestimate the fatigue life of the pavement.

5.3.4 Effect of Load Levels

Damage contours under 20 kN loading are plotted in Fig. 5.12 for the uniform and non-uniform contract pressures, respectively. The magnitude of damage under 20 kN is dramatically reduced for thin pavements. Another observation is that the factor of two-reduction in the load level resulted in the damage reduction regardless of structures, contract pressure distribution, and layer properties.

One major use of the damage values calculated from different load levels is the development of Equivalent Axle Load Factor (EALF) or Load Equivalency Factor (LEF). EALF is defined as the damage per pass caused to a specific pavement system by the load in question relative to the damage per pass of an arbitrarily selected standard load moving on the same pavement system. Traditionally, the damage under a load was either represented by critical pavement responses or calculated by performance equations. Using the damage computed from the VECD-FEP++, one can directly determine the damage ratios of different load levels and therefore EALFs.

5.3.5 Effect of AC Stiffnesses

Fig. 5.13 presents the damage contours calculated using two AC layer stiffnesses (AC I and AC II in Table 5.1) under both uniform and non-uniform pressure distributions. It can be concluded from this figure that the damage under the tire edge becomes slightly greater as the stiffness of the AC layer increases. This observation may become important

when the aging of the AC layer is concerned. It is known that the aging occurs only at the top portion of the AC layer. The stiffening effect of aging therefore makes the top portion of the AC layer stiffer than the rest of the layer, which in turn increases the chance of top-down cracking.

5.4 SUMMARY

The findings in this chapter demonstrate how the VECD-FEP++ may be used in evaluating the effect of various pavement factors on pavement responses as well as damage. The most important conclusions from this parametric study can be summarized as follows:

1. The AC layer thickness has significant effects on the magnitude and location of damage. As the AC layer becomes thicker, the failure mechanism shifts from the bottom-up cracking with most damage at the bottom of the AC layer to the bi-modal mechanism where both bottom-up and top-down cracking occurs, or to the dominant top-down cracking in the case of the thickest AC layer in this study.
2. The damage contour is more affected by the base stiffness than by the subgrade and AC stiffnesses.
3. The non-uniform pressure causes larger stresses and greater damage than the uniform pressure does.
4. The contribution of top-down cracking to the overall cracking in the AC layer becomes greater under the non-uniform pressure than under the uniform pressure.
5. The conjoined damage contours in thicker pavements suggest that the through-the-thickness crack may develop as these bottom-up and top-down cracks propagate

simultaneously and coalesce together. This finding is supported by Gerritsen et al. (1987) and Groenendijk et al.'s (1997b) observation from field cores in which both top-down and bottom-up cracks were found with no cracking in the middle of the core. This observation raises a serious question on the validity of the traditional fatigue performance prediction approach in which only the tensile strain at the bottom of the AC layer is considered in predicting the fatigue life of the asphalt pavements.

6. The damage level computed by the VECD-FEP++ provides a direct and more reliable way of determining Equivalent Axle Load Factor of different load levels.

Table 5.1 Layer Thicknesses and Properties Selected in This Study

Pavement Layer	Thickness (cm) (Poisson Ratio)	Material Parameter			
		AC I		AC II	
		Relaxation Time	Prony Coefficients (kPa)	Relaxation Time	Prony Coefficients (kPa)
Asphalt Concrete	7.6, 17.8, 30.5, 43 (0.30)	0.02	4908141.9	0.02	1258989.3
		0.2	5735749.4	0.2	2214693.3
		2	4955029.9	2	3621321.1
		20	2956638.2	20	5136030.7
		200	1261172.2	200	5729228.2
		2000	446992.8	2000	4459729.9
		20000	157584.1	20000	2317303.2
		E_∞: 58269.0 kPa		E_∞: 155243.0 kPa	
		Damage Function: $C(S) = \exp(-0.00228 \cdot S^{0.506})$			

Base	50 (0.35)	Type	k_1	k_2	k_3
		Stiff	5764.0	0.420	-0.240
		Weak	354.0	0.484	-0.403

Subgrade	Infinite (0.40)	Type	k_1	k_3
		Stiff	474.0	-0.366
		Weak	771.0	-0.169

Combination	Type of Base	Type of Subgrade
MODULUS SS	Stiff	Stiff
MODULUS SW	Stiff	Weak
MODULUS WS	Weak	Stiff
MODULUS WW	Weak	Weak

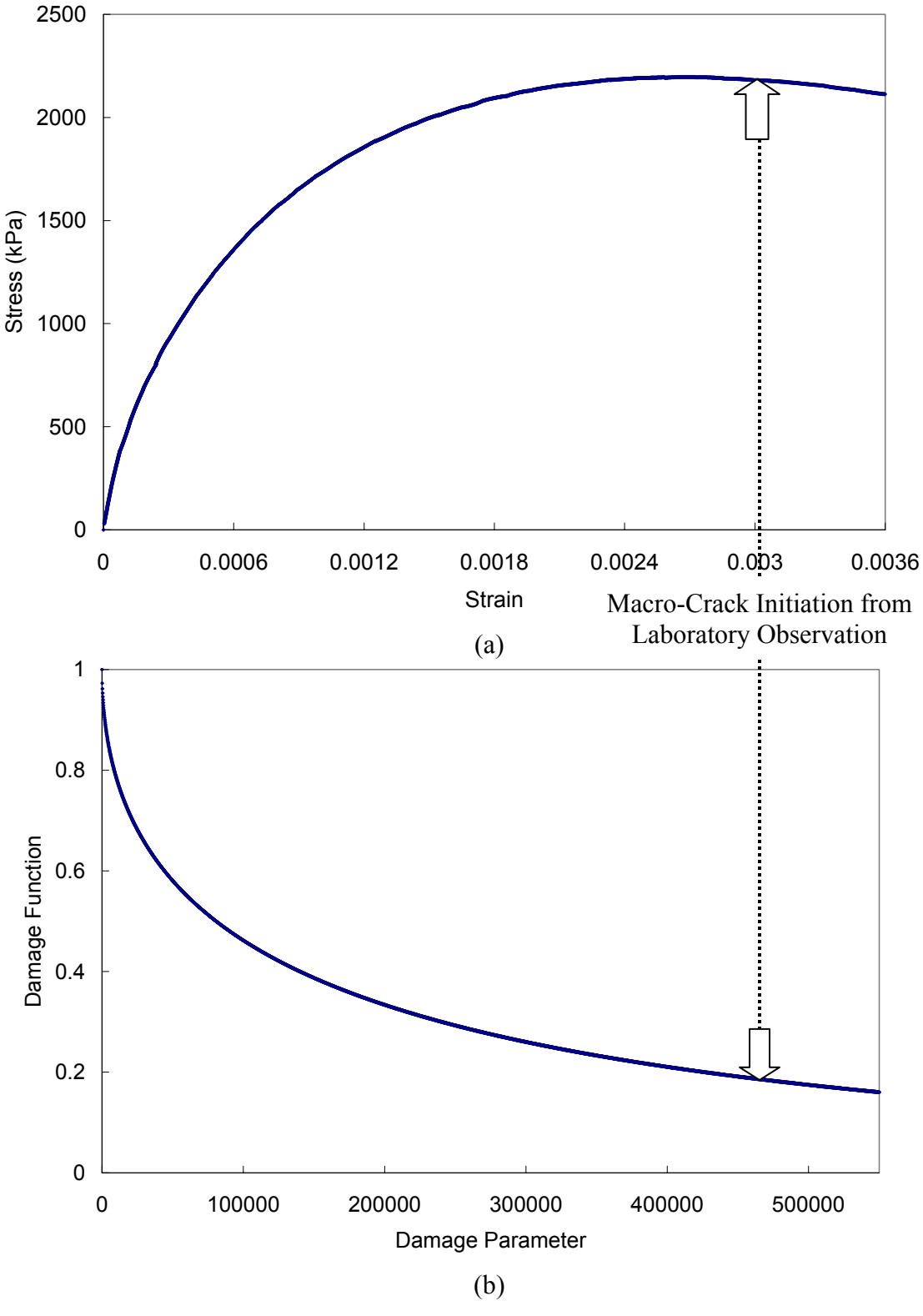

Figure 5.1 Uniaxial Monotonic Tension Lab Test Results: (a) Stress/Strain Behavior and (b) Characteristic Damage Function (Chehab, 2002)

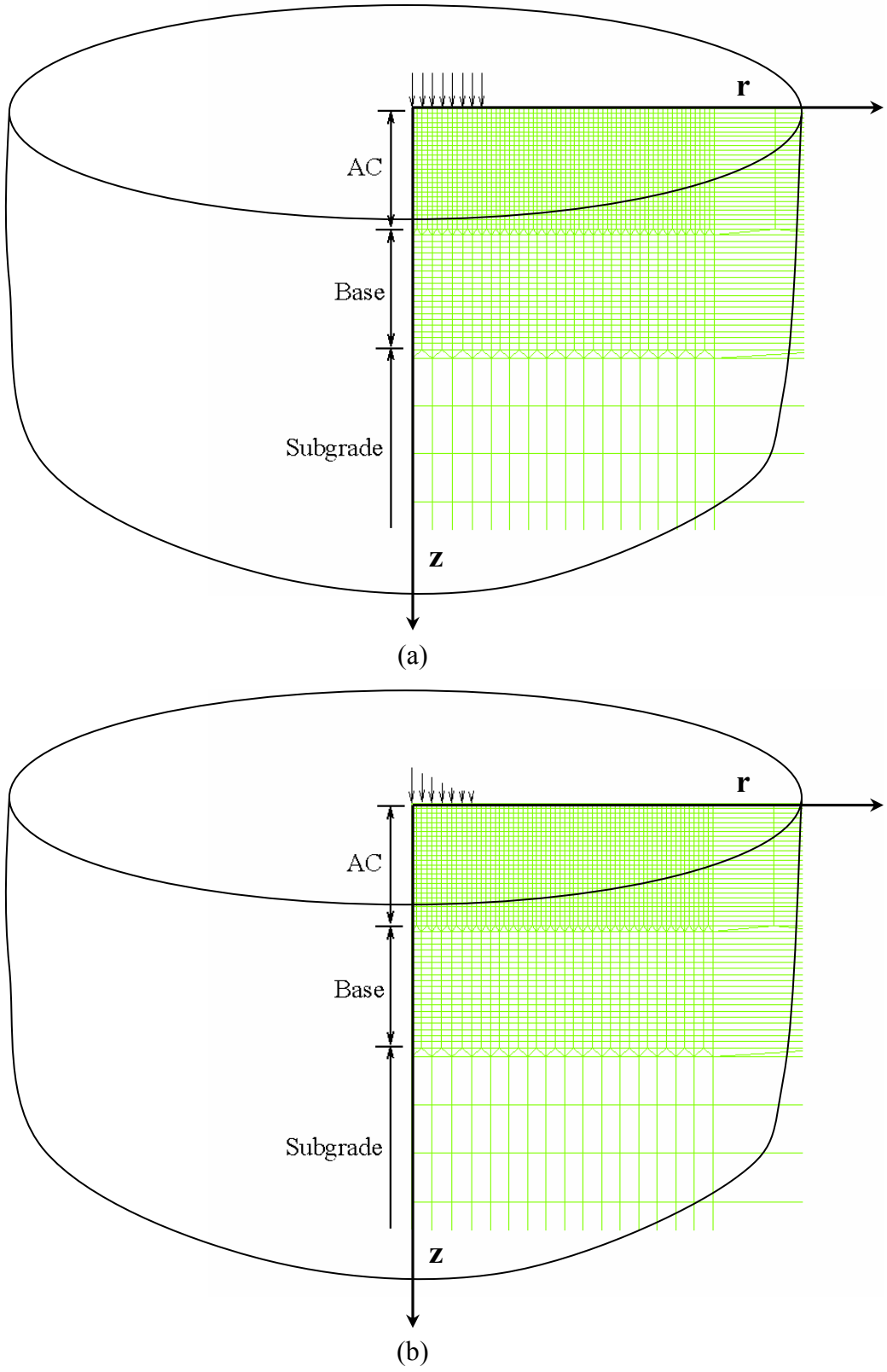

Figure 5.2 Axisymmetric FE Model: (a) Uniform Pressure; (b) Non-uniform Pressure

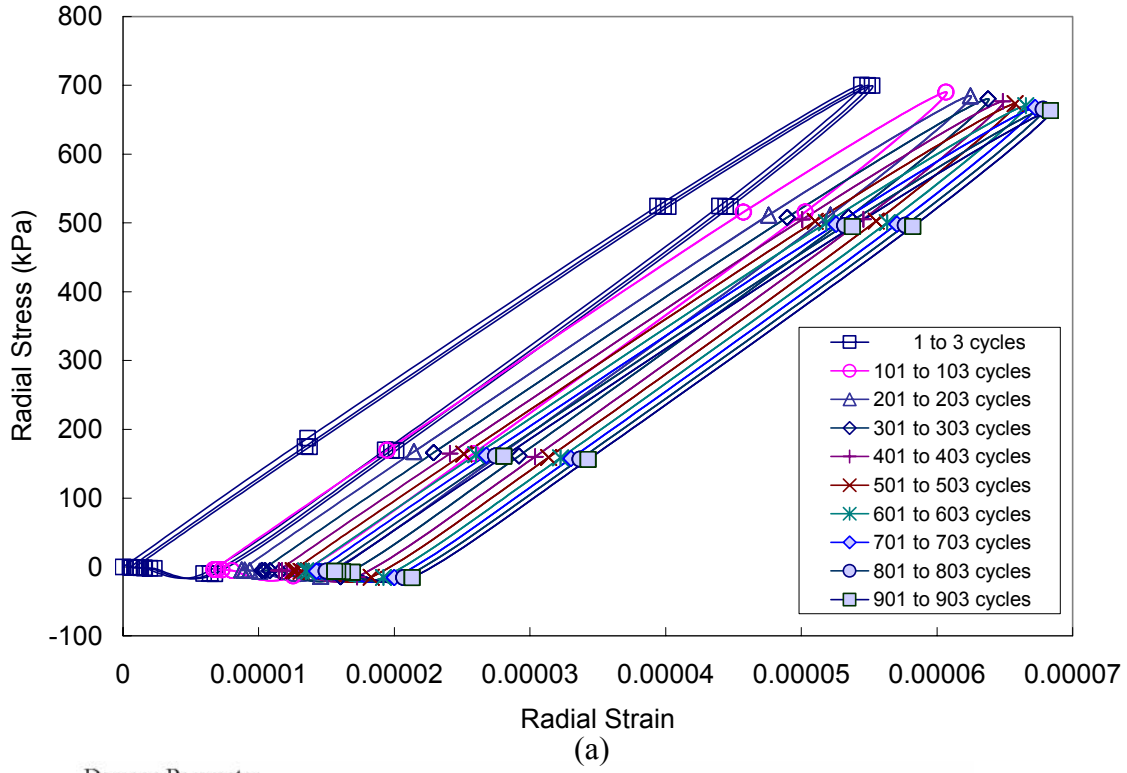

(a)

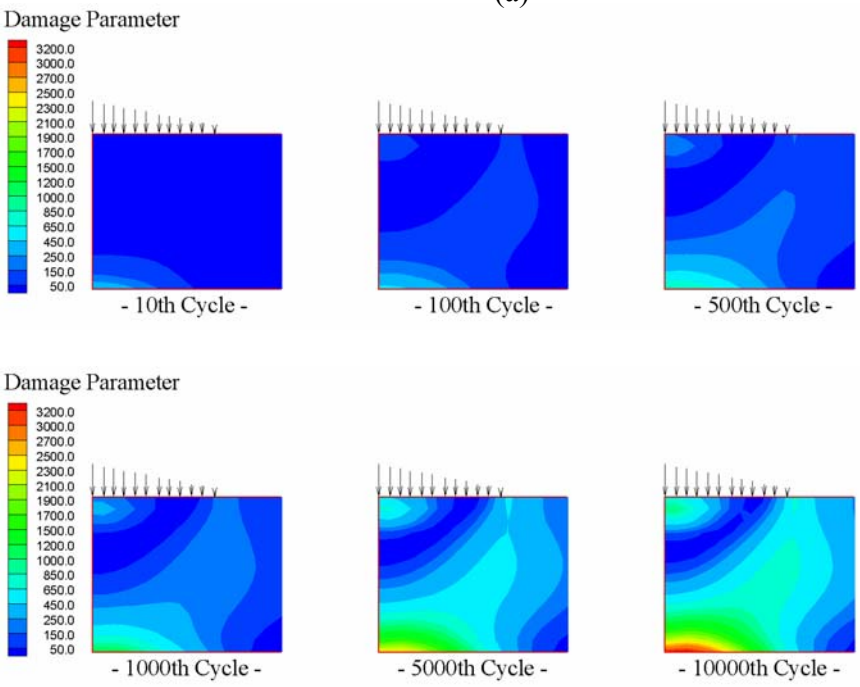

(b)

Figure 5.3 Asphalt Concrete Pavement Structure Simulated by the VECD-FEP++: (a) Cyclic Hysteresis Behavior and (b) Damage Contours at Different Cycles

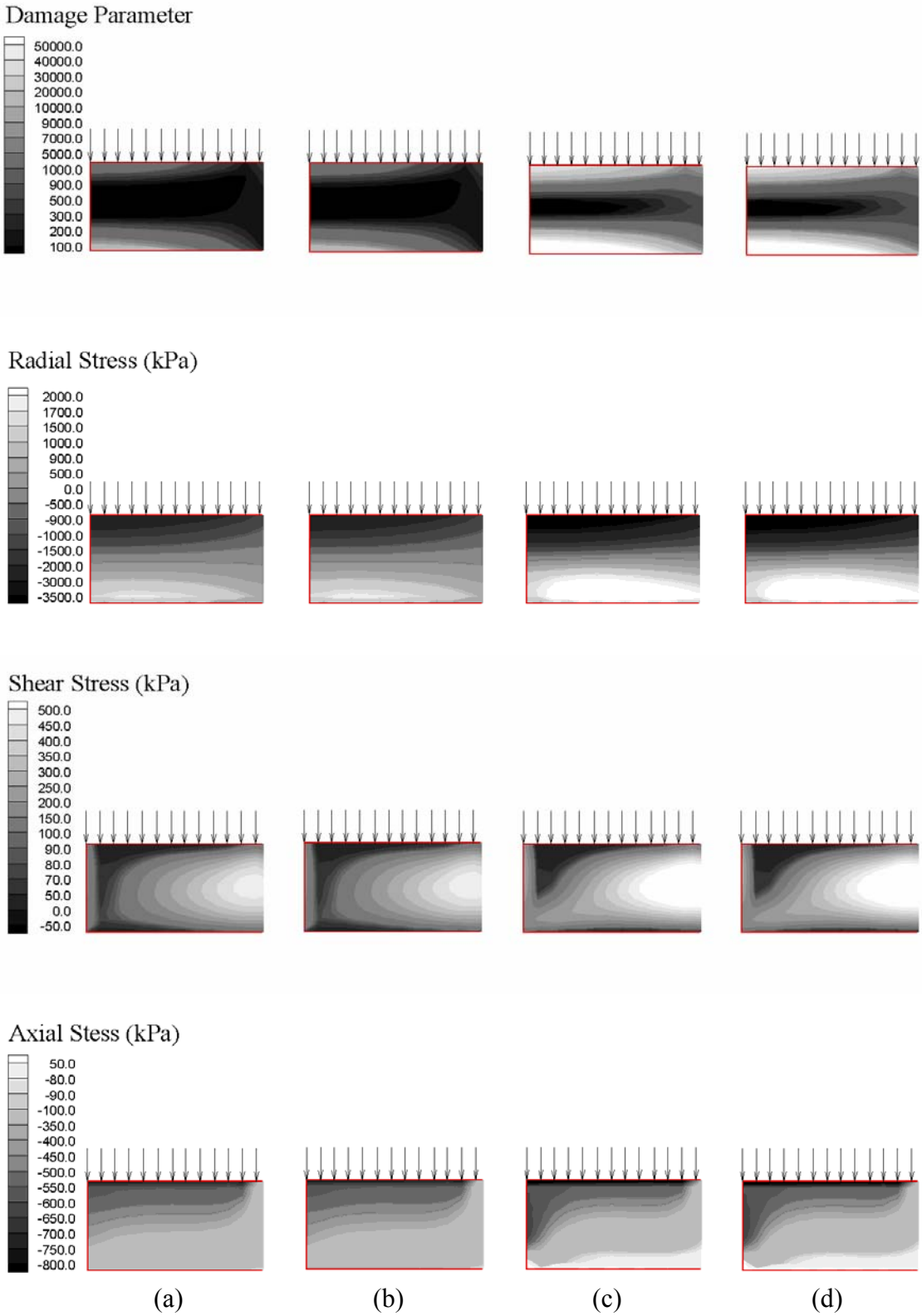

Figure 5.4 Thin AC Cases under Uniform 40 kN Load for: (a) MODULUS SS, (b) MODULUS SW, (c) MODULUS WS, and (d) MODULUS WW

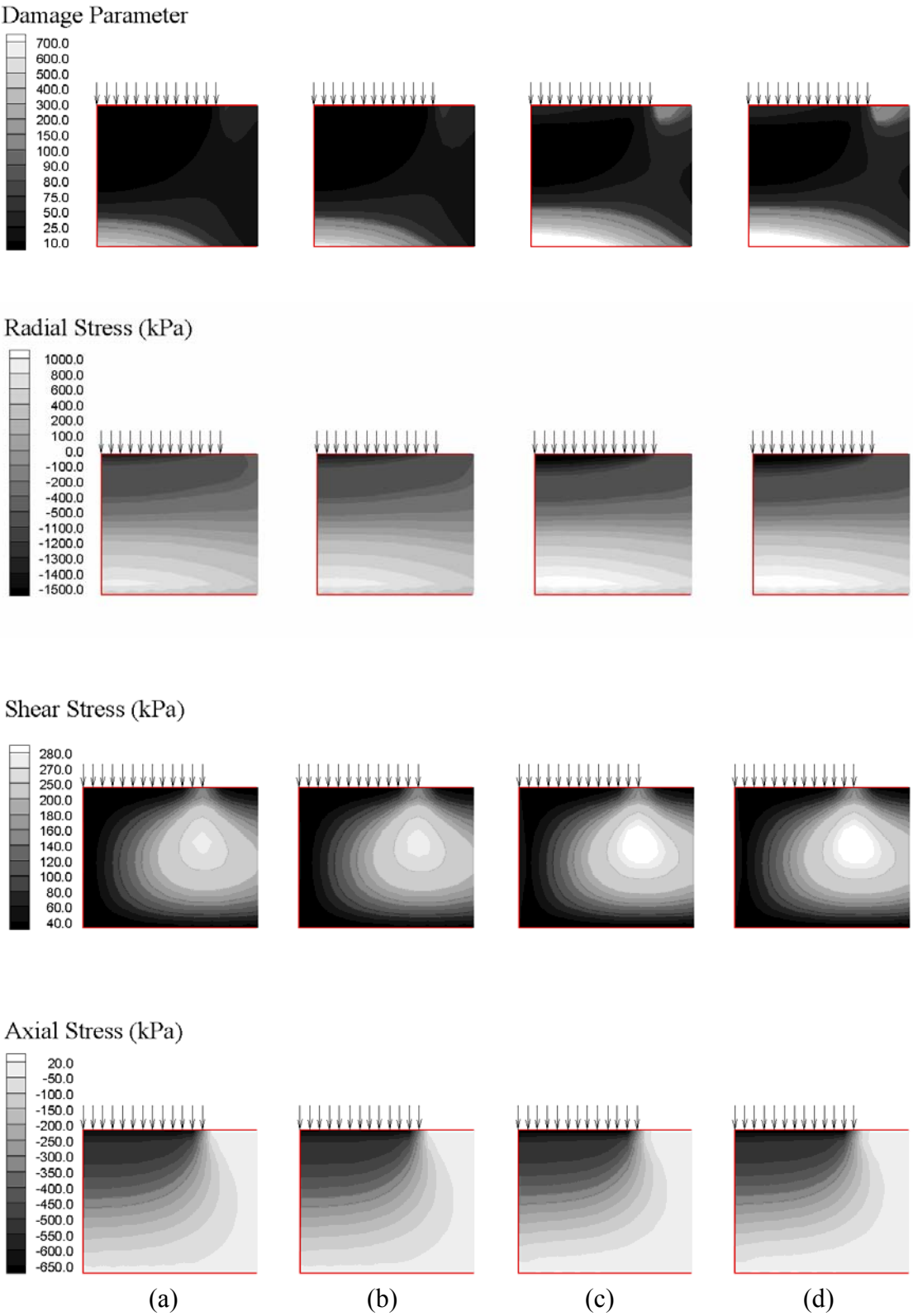

Figure 5.5 Medium AC Cases under Uniform 40 kN Load for: (a) MODULUS SS, (b) MODULUS SW, (c) MODULUS WS, and (d) MODULUS WW

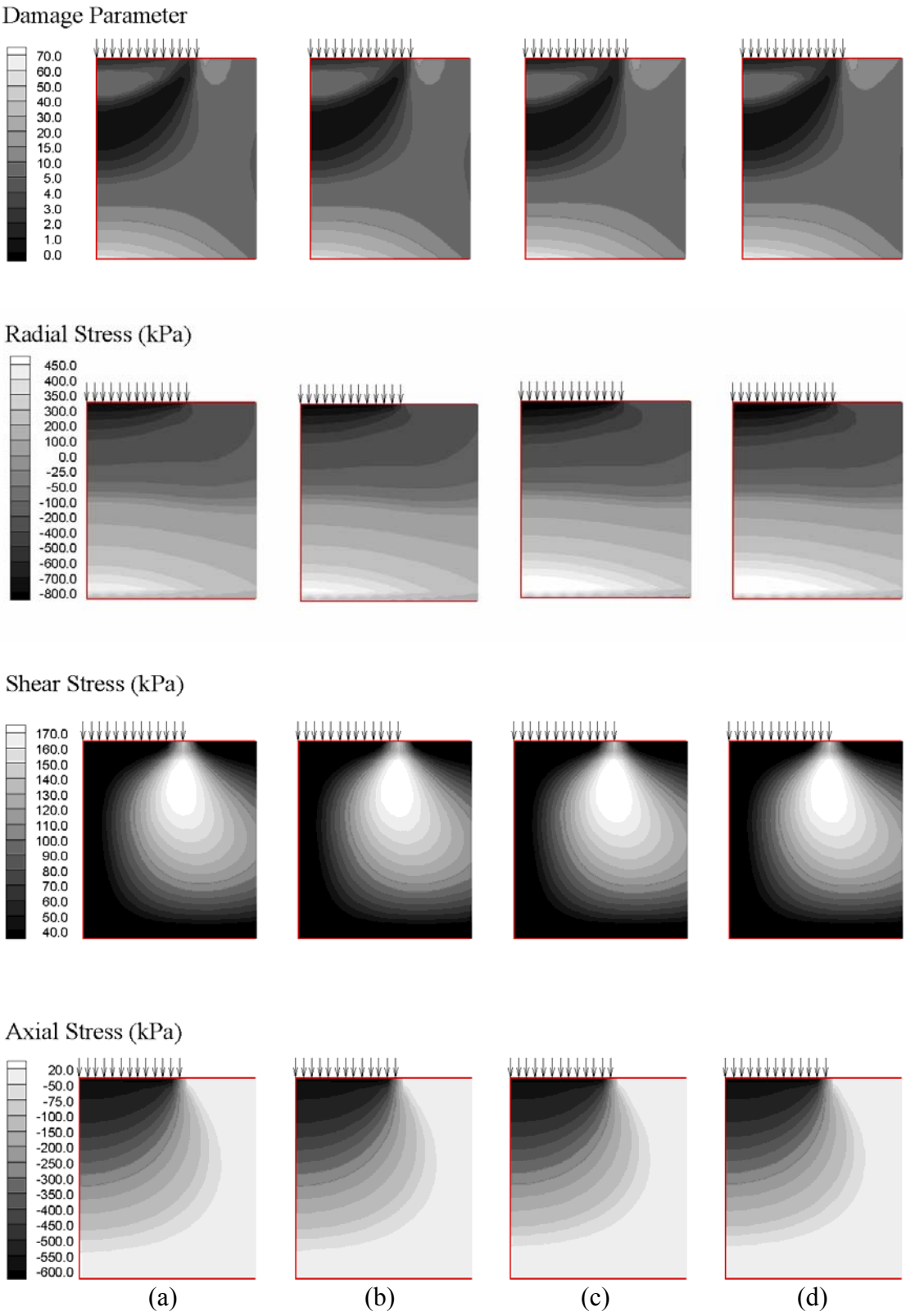

Figure 5.6 Thick I AC Cases under Uniform 40 kN Load for: (a) MODULUS SS, (b) MODULUS SW, (c) MODULUS WS, and (d) MODULUS WW

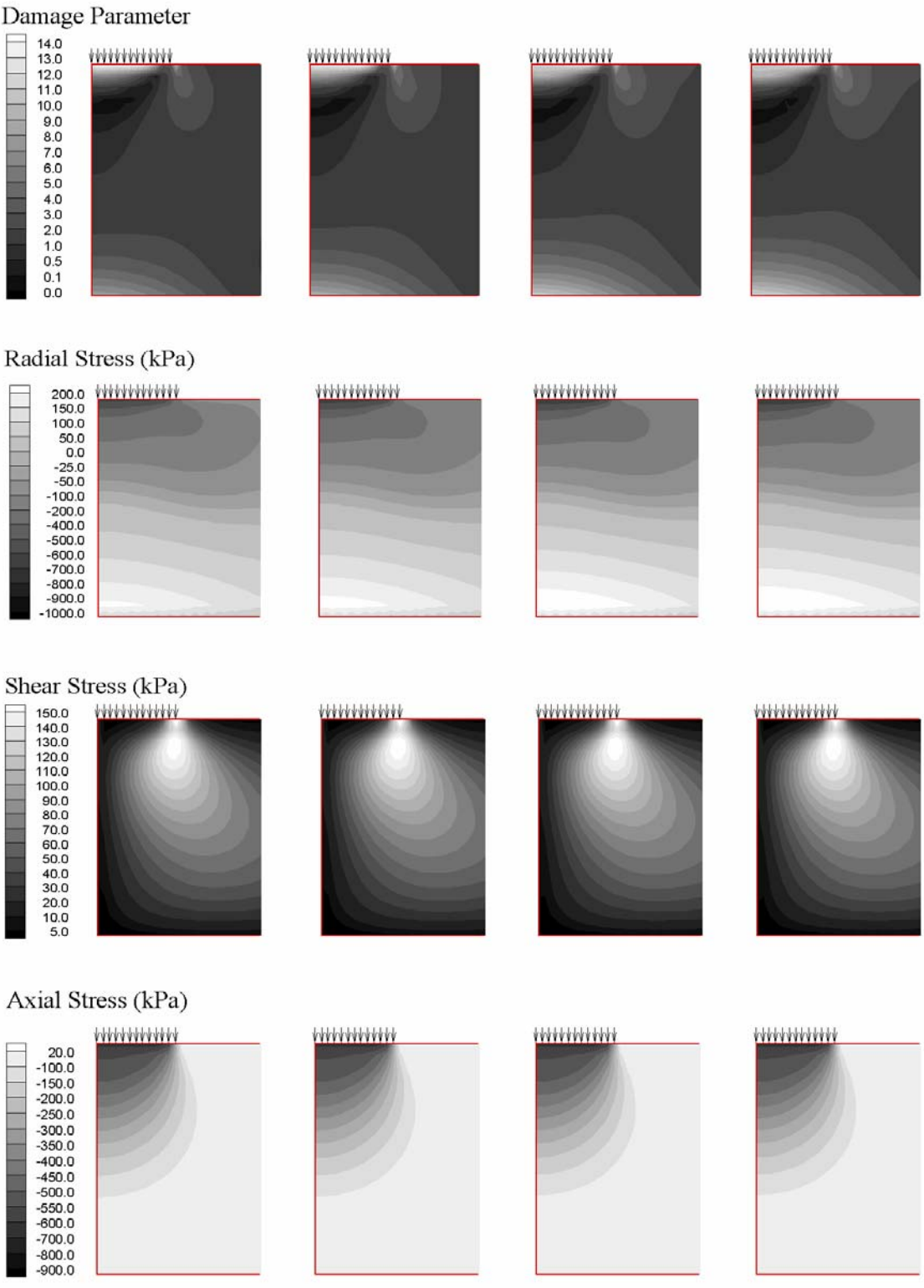

Figure 5.7 Thick II AC Cases under Uniform 40 kN Load for: (a) MODULUS SS, (b) MODULUS SW, (c) MODULUS WS, and (d) MODULUS WW

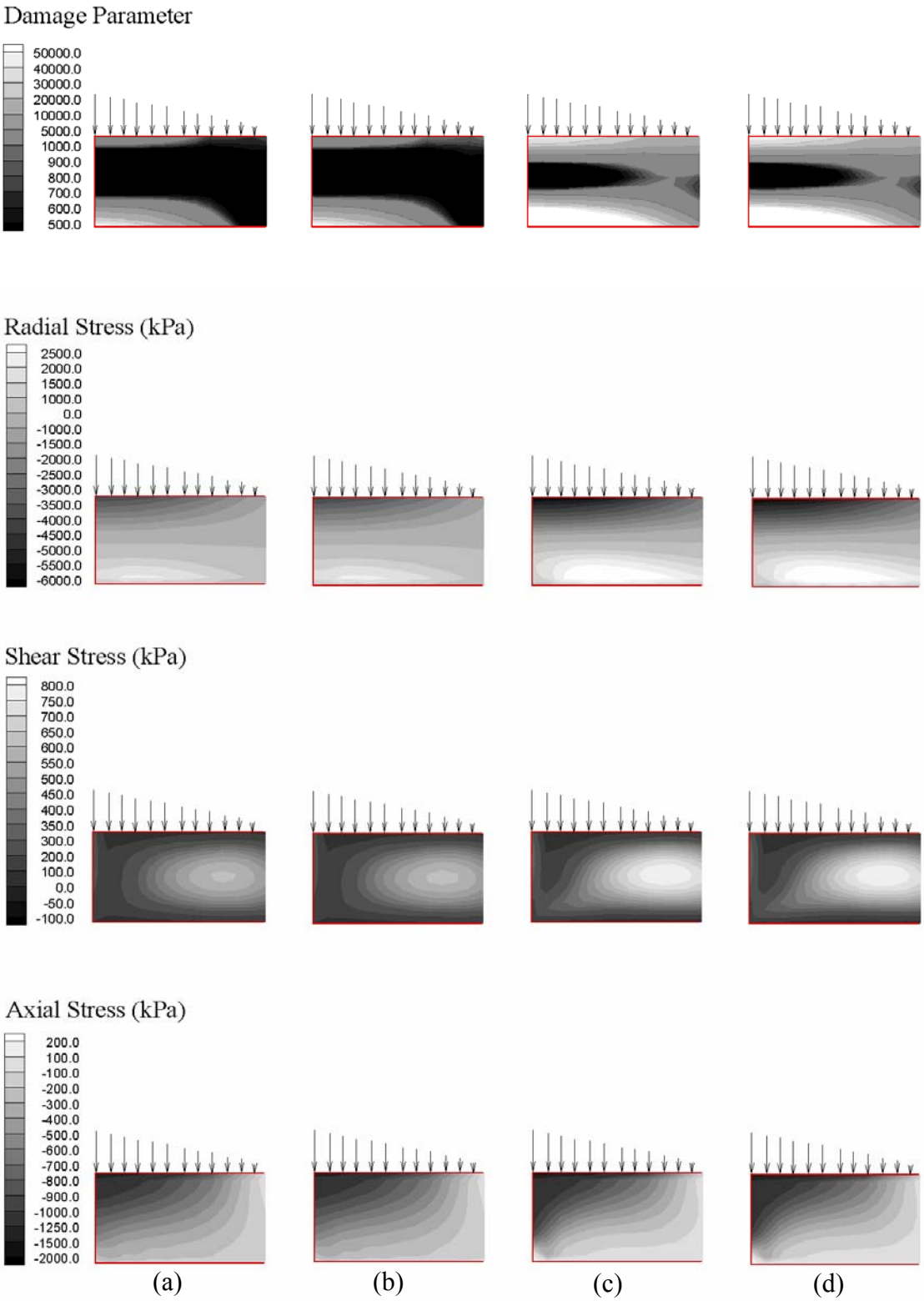

Figure 5.8 Thin AC Cases under Non-uniform 40 kN Load for: (a) MODULUS SS, (b) MODULUS SW, (c) MODULUS WS, and (d) MODULUS WW

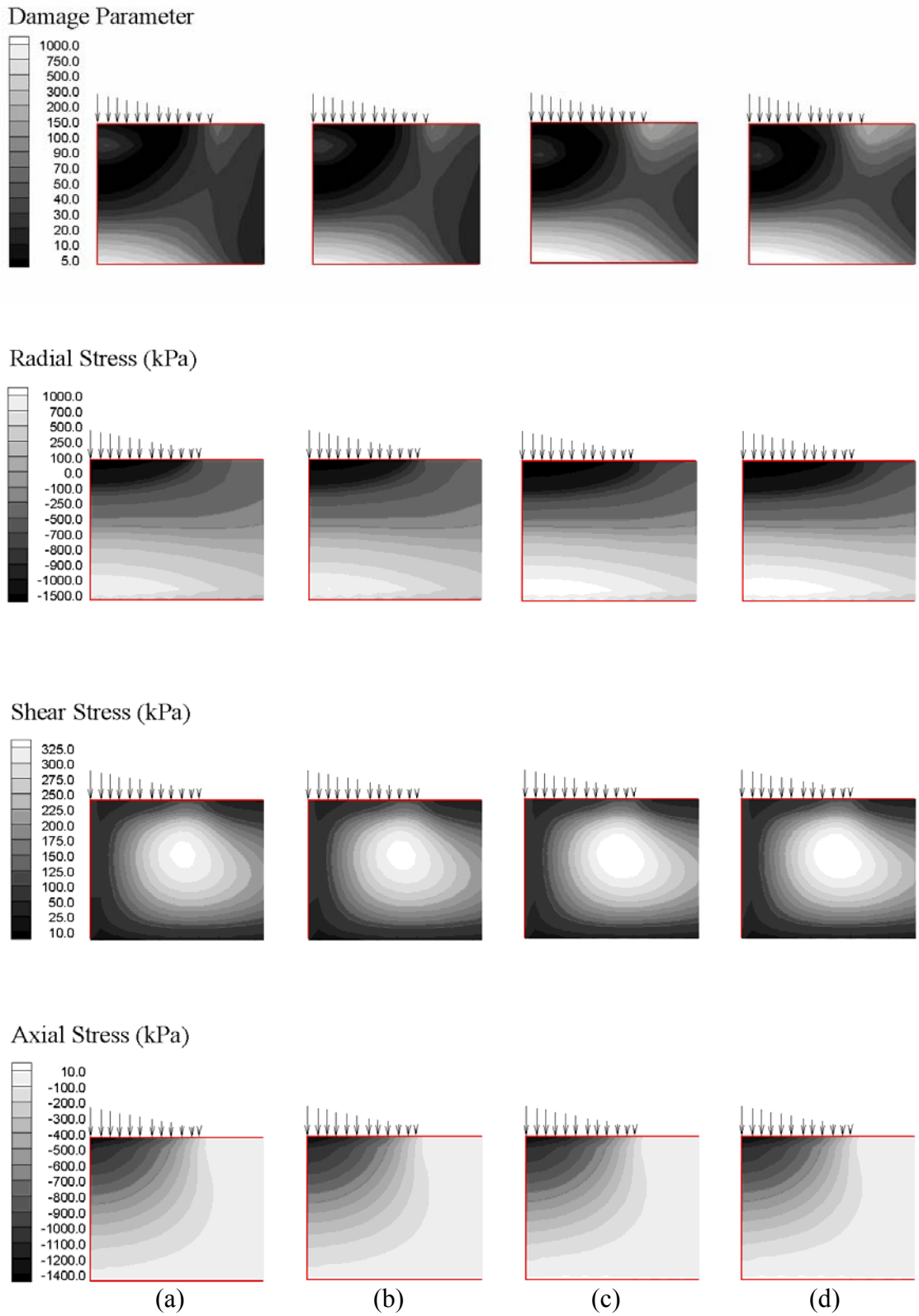

Figure 5.9 Medium AC Cases under Non-uniform 40 kN Load for: (a) MODULUS SS, (b) MODULUS SW, (c) MODULUS WS, and (d) MODULUS WW

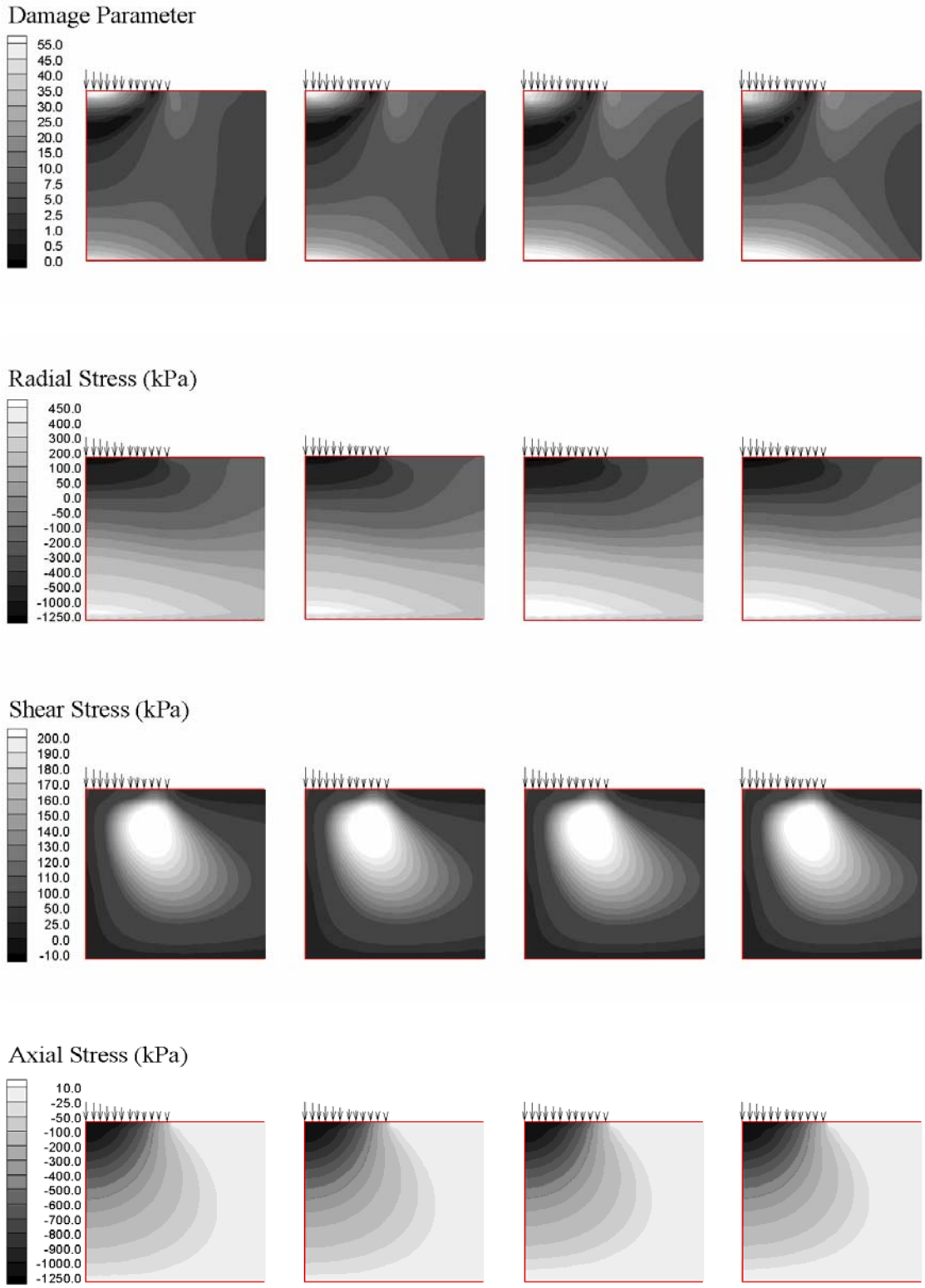

Figure 5.10 Thick I AC Cases under Non-uniform 40 kN Load for: (a) MODULUS SS, (b) MODULUS SW, (c) MODULUS WS, and (d) MODULUS WW

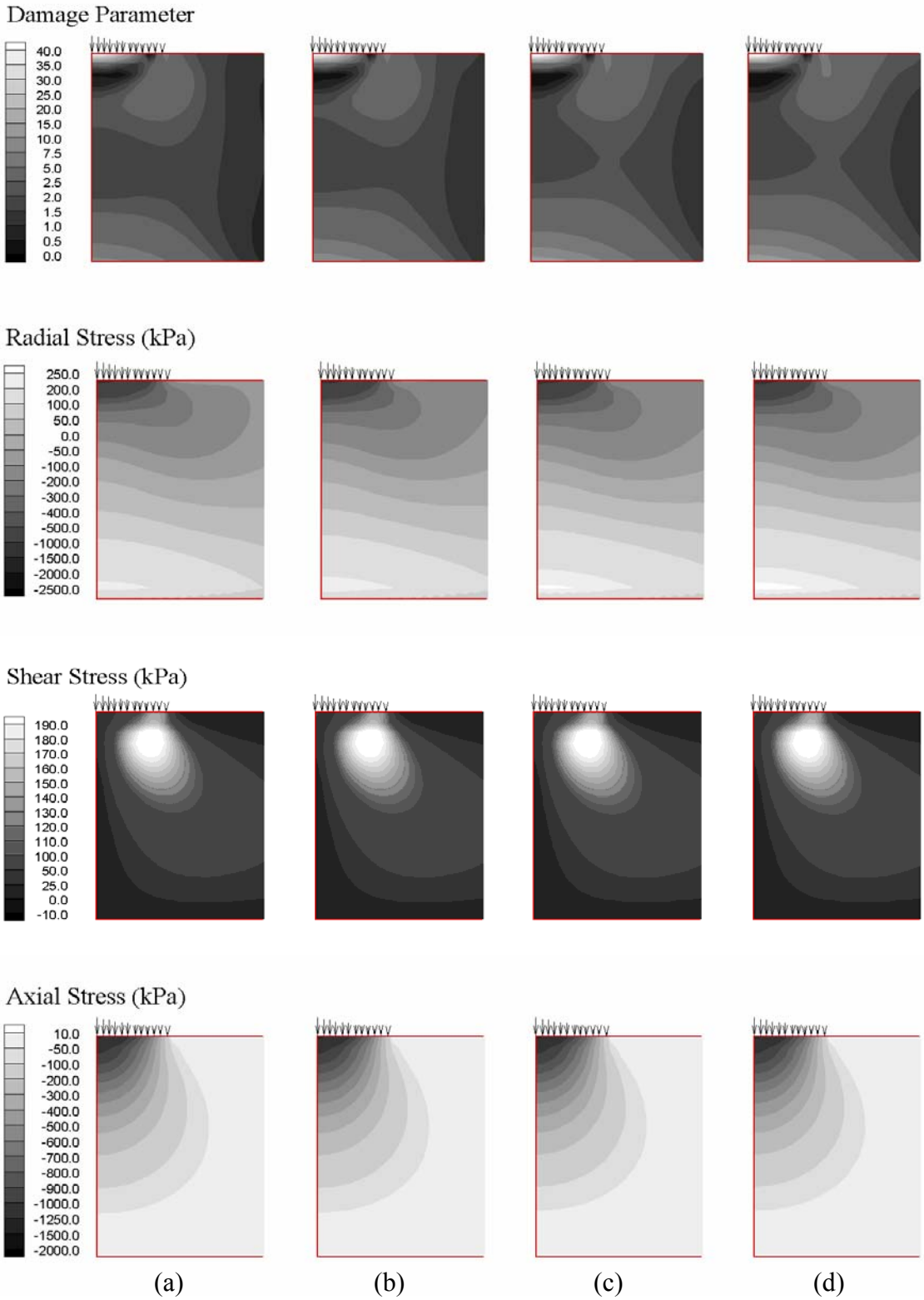

Figure 5.11 Thick II AC Cases under Non-uniform 40 kN Load for: (a) MODULUS SS, (b) MODULUS SW, (c) MODULUS WS, and (d) MODULUS WW

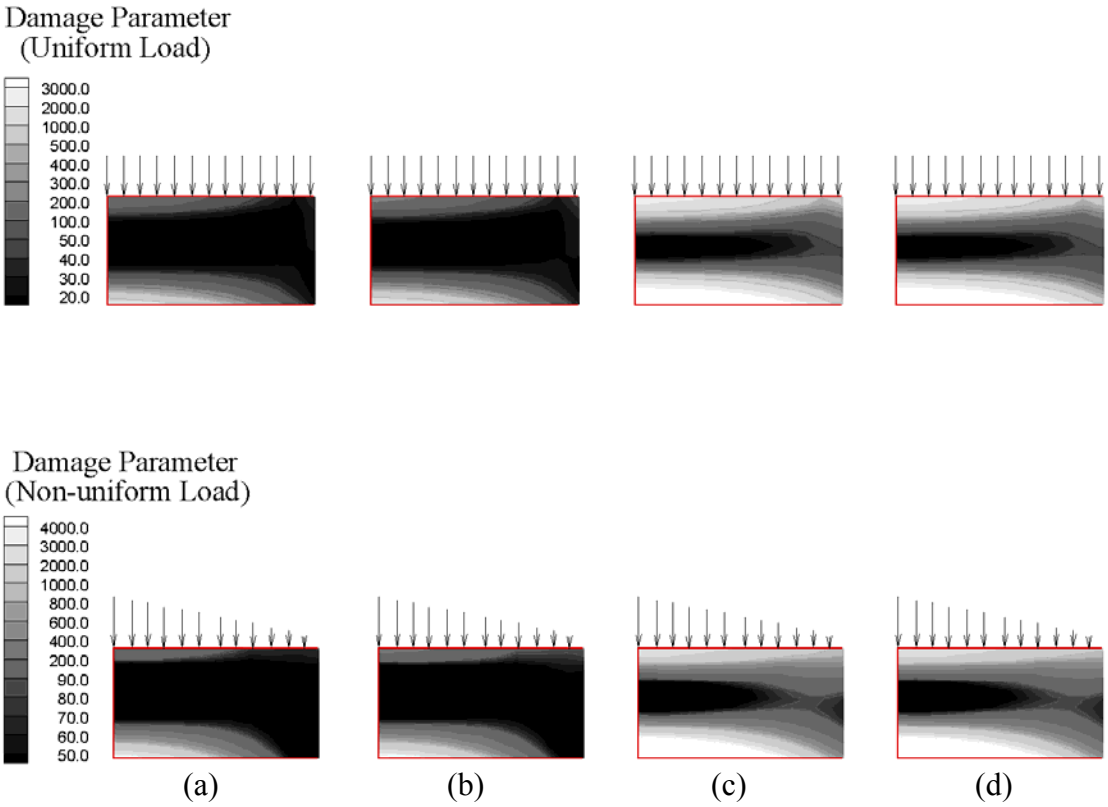

Figure 5.12 Thin AC Damage Contours under Uniform and Non-uniform 20 kN Load for: (a) MODULUS SS, (b) MODULUS SW, (c) MODULUS WS, and (d) MODULUS WW

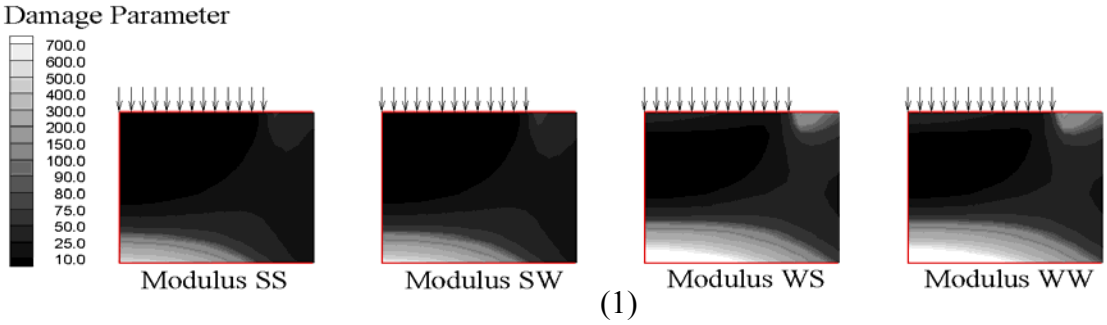

(1)

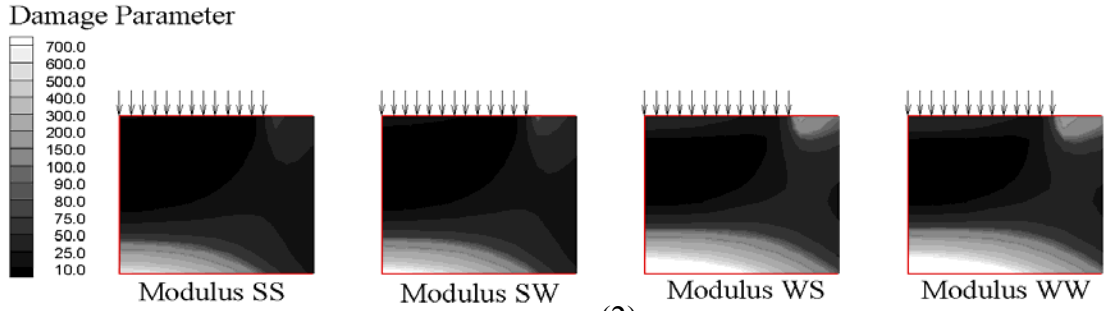

(2)

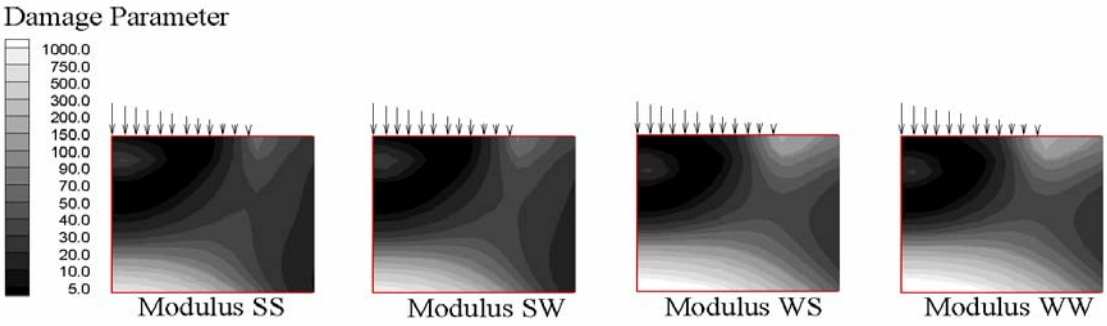

(3)

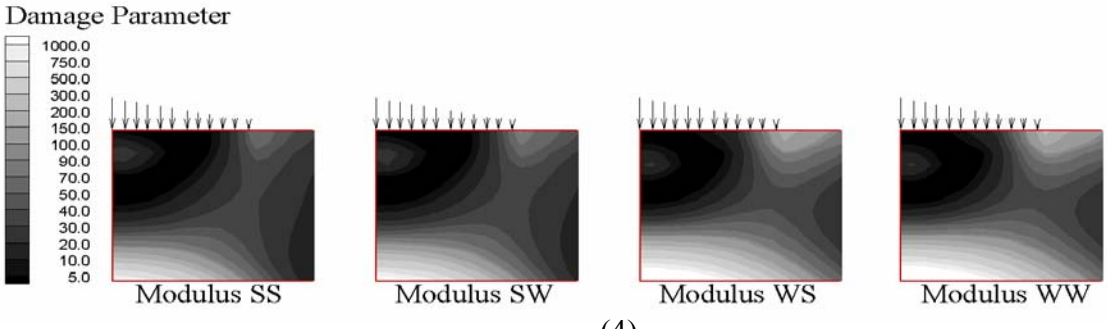

(4)

Figure 5.13 Medium AC Damage Contours for Base/Subgrade Modulus Combinations: (1) Uniform Pressure and AC I Stiffness; (2) Uniform Pressure and AC II Stiffness; (3) Non-uniform Pressure and AC I Stiffness; (4) Non-uniform Pressure and AC II Stiffness

CHAPTER 6

CONCLUSIONS AND RECOMMENDATIONS FOR FUTURE RESEARCH

A finite element program employing the viscoelastic continuum damage (VECD) model for asphalt layers and the stress-state dependent nonlinear elastic model for unbound layers is developed in this study. Several different verification studies were successfully conducted using the laboratory test data and analytical solutions. The laboratory test methods used in the verification study of the finite element program with the VECD are constant-crosshead-rate monotonic tests in uniaxial tension at varying temperatures and loading rates. For the verification of the finite element program with the stress-dependent nonlinear elastic model, results from the triaxial tests of fine-grained and granular soils were used.

The following conclusions were obtained from this study:

- The verification study of the finite element program with the VECD model revealed that the model is accurate for reduced strain rates greater than approximately 0.000012/sec. At the reduced strain rate slower than this rate, viscoplasticity becomes significant in the asphalt concrete behavior and causes errors in prediction.
- Using the data from the laboratory triaxial tests of fine-grained and granular soils, the implemented finite element model was found to be useful for characterizing the soil stiffness.
- The VECD-FEP++ program developed in this study demonstrates a great potential in evaluating the crack initiation mechanisms by directly calculating the intensity of damage at different locations (i.e., damage contours). The parametric study of various

pavement and load factors using the VECD-FEP++ program resulted in the following conclusions:

- The AC layer thickness has significant effects on the magnitude and location of damage. As the AC layer becomes thicker, the failure mechanism shifts from the bottom-up cracking with most damage at the bottom of the AC layer to the bi-modal mechanism where both bottom-up and top-down cracking occurs, or to the dominant top-down cracking in the case of the thickest AC layer in this study.
- The damage contour is more affected by the base stiffness than by the subgrade and AC stiffnesses.
- The non-uniform pressure causes larger stresses and greater damage than the uniform pressure does.
- The contribution of top-down cracking to the overall cracking in the AC layer becomes greater under the non-uniform pressure than under the uniform pressure.
- The conjoined damage contours in thicker pavements suggest that the through-the-thickness crack may develop as these bottom-up and top-down cracks propagate simultaneously and coalesce together. This finding is supported by Gerritsen et al.'s (1987) observation from field cores in which both top-down and bottom-up cracks were found with no cracking in the middle of the core. This observation raises a serious question on the validity of the traditional fatigue performance prediction approach in

which only the tensile strain at the bottom of the AC layer is considered in predicting the fatigue life of the asphalt pavements.

- The damage level computed by the VECD-FEP++ provides a direct and more reliable way of determining Equivalent Axle Load Factor of different load levels.

Although the developed VECD-FEP++ program is an excellent means of modeling pavement responses and performance by directly calculating the cracking damage in asphalt pavements, some improvements could be made to make this program more accurate and efficient. The areas for the future research are:

- More efficient numerical algorithms: In order to evaluate the stress and damage contours during the entire fatigue life of the asphalt pavement, a more efficient numerical algorithm is required. As new and more efficient algorithms are developed, they need to be incorporated into the VECD-FEP++ program to make the computation faster.
- Incorporation of viscoplasticity: The VECD-FEP++ program is only applicable when elasticity and viscoelasticity are dominant in the asphalt concrete behavior, i.e., low temperature and/or fast rate of loading. To account for the plastic and viscoelastic flow at high temperatures and/or slow loading rates and its effect on crack initiation, viscoplasticity needs to be incorporated into the current model.
- Multiaxial VECD model: The current VECD model is developed from a set of uniaxial tension tests. It is known that the confining pressure has a significant effect on the behavior of asphalt concrete. Multiaxial VECD model characterized by triaxial tests will result in more realistic and accurate stress and damage contours.

CHAPTER 7

LIST OF REFERENCES

Biot, M. A. Linear Thermodynamics and the Mechanics of Solids. Proc. 3rd U.S. Nat. Congr. Appl. Mech., 1, 1958, pp. 1-18.

Bradshaw, R. D., and L. C. A Sign Control Method for Fitting and Interconverting Material Functions for Linearly Viscoelastic Solids. *Mechanics of Time-Dependent Materials 1*, 1997, pp 85-108.

Brown, S. F. and J. W. Pappin. Analysis of Pavements with Granular Bases. In *Transportation Research Record 810*, TRB, National Research Council, Washington, D.C., 1981, pp. 17-23.

Chehab, R. G. *Characterization of Asphalt Concrete in Tension Using a viscoelastoplastic Model*. Dissertation, North Carolina State University, 2002.

Chehab, G.R., Y.R. Kim, R.A. Schapery, M.W. Witczak, R. Bonaquist, Time-Temperature Superposition Principle for Asphalt Concrete Mixtures with Growing Damage in Tension, Paper to be published at the *Journal of Association of Asphalt Paving Technologists*, 2002.

Christensen, R.M., *Theory of Viscoelasticity: An Introduction*. Academic Press, Inc., London, 1982.

Daniel, J.S. and Y.R. Kim, Development of a Simplified Fatigue Test and Analysis Procedure Using a Viscoelastic Continuum Damage Model, Paper to be published at the *Journal of Association of Asphalt Paving Technologists*, 2002.

Elliot, R. P., and L. David. Improved Characterization Model for Granular Bases. In *Transportation Research Record 1227*, TRB, National Research Council, Washington, D.C., 1989, pp. 128-133.

Emri, I., and N. W. Tschoegl. Generating Line Spectra from Experimental Responses. Part I: Relaxation Modulus and Creep Compliance. *Rheol. Acta 32*, 1993, pp. 311-321.

Emri, I., and N. W. Tschoegl. Generating Line Spectra from Experimental Responses. Part IV: Application to Experimental Data. *Rheol. Acta 33*, 1994, pp. 60-70.

Emri, I., and N. W. Tshoegl. Determination of Mechanical Spectra from Experimental Responses. *Int. J. Solids and Structures*, 32, 1995, pp. 817-826.

Ferry, J. D. *Viscoelastic Properties of Polymers*. 3rd ed., Wiley, New York, 1980.

Fletcher, R. *Practical Methods of Optimization*. 2nd ed., Wiley, New York, 1987.

Garg, N., and M. R. Thompson. Mechanistic-Empirical Evaluation of the Mn/ROAD Low Volume Road Test Sections, Illinois Cooperative Highway and Transportation Research Program Report FHWA-IL-UI-262, Urbana, IL, 1998.

Gerritsen, A. H., C. A. P. M. Van Gurp, J. P. J. Van der Heide, A. A. A. Molenaar, and A. C. Pronk. Prediction and Prevention of Surface Cracking in Asphalt Pavements. *6th International Conference on Structural Design and Asphalt Pavements*, The University of Michican, Ann Arbor, Michigan, 1987, pp. 378-391.

Groenendijk, J., C. H. Vogelzang, A. A. A. Molenaar, B. R. Mante, and L. J. M. Dohmen. Linear Tracking Response Measurments: Determining Effects of Wheel-Liad Configuration. In *Transportation Research Record 1570*, TRB, National Research Council, Washington, D.C., 1997a, pp. 1-9.

Groenendijk, J., C. H. Vogelzang, A. Miradi, A. A. A. Molenaar, and L. J. M. Dohman. Linear Tracking Performance Tests on Full-Depth Asphalt Pavement. In *Transportation Research Record 1570*, TRB, National Research Council, Washington, D.C., 1997b, pp. 39-47.

Guddati, M. N. *FEP++: A Finite Element Program in C++*, Input Manual, Department of Civil, Construction, and Environmental Engineering, North Carolina State University, 2001.

Ha, K., and R. A. Schapery. A Three-Dimensional Viscoelastic Constitutive Model for Particulate Composites with Growing Damage and Its Experimental Validation. *International Journal of Solids and Structures*, 35, 1998, pp. 3497-3517.

Harichandran, R. S., G. Y. Baladi, and M. S. Yeh. *Development of a Computer Program for Design of Pavement Systems Consisting of Bound and Unbound Materials*. Department of Civil and Environmental Engineering, Michigan State University, 1989.

Hibbit, Karlsson and Sorenson, Inc. *ABAQUS User's Manual*, Hibbit, Karlsson and Sorenson, Inc, 2001.

Hinterhoelzl, R. *Implementation of an Umat for Solid Propellant in the FEM Program Abaqus According to the Constitutive Law*. Research Report, University of Texas at Austin, 2000.

Hjelmstad, K. D., and E. Taciroglu. Analysis and Implementation of Resilient Modulus Models for Granular Solids. *Journal of Engineering Mechanics*, Vol. 126, No. 8, ASCE, 2000, pp. 821-830.

Huang, Y. H. *Pavement Analysis and Design*. Prentice-Hall, Inc., Englewood Cliffs, New Jersey, 1993.

Hughes, T.J.R., *The Finite Element Method: Linear Static and Dynamic Finite Element Analysis*. Dover Publications, 2000.

Jenq, Y-S., and J-D. Perng. Analysis of Crack Propagation in Asphalt Concrete Using Cohesive Crack Model. *In Transportation Research Record 1317*, TRB, National Research Council, Washington, D.C., 1991, pp. 90-99.

Jenq, Y-S., C-J. Liaw, and P. Liu. Analysis of Crack Resistance of Asphalt Concrete Overlays- A Fracture Mechanics Approach. *In Transportation Research Record 1388*, TRB, National Research Council, Washington, D.C., 1993, pp. 160-166.

Kaliske, M., and H. Rothert. Formulation and Implementation of Three-Dimensional Viscoelasticity at Small and Finite Strains. *Computational Mechanics*, 19, 1997, pp. 228-239.

Kim, Y.R., H.J. Lee, and D.N. Little, Fatigue Characterization of Asphalt Concrete Using Viscoelasticity and Continuum Damage Theory, *Journal of the Association of Asphalt Paving Technologists*, Vol. 66, 1997, pp. 520-569.

Kim, Y. R. and Y-C. Lee. *Condition Assessment of Flexible Pavements Using FWD Deflections*. Final Report, NCDOT Project, 1997.

Kim, Y. R., J. S. Daniel, and H. Wen. *Fatigue Performance Evaluation of Westrack Asphalt Mixtures Using Viscoelastic Continuum Damage Approach*. Report HWY-0678. NCDOT, 2001.

Lackner R., and H. A. Mang. Adaptive FE Analysis of RC Shells. I: Theory. *Journal of Engineering Mechanics*, Vol. 127, No, 12, ASCE, 2001, pp. 1203-1212.

Lee, S., and W. G. Knauss. A Note on the Determination of Relaxation and Creep Data from Ramp Tests. *Mechanics of Time-Dependent Materials 4*, 2000, pp. 1-7.
Linz, P., *Analytical and Numerical Methods for Volterra Equations*, Siam, Philadelphia, 1985.

Linz, P. *Analytical and Numerical Methods for Volterra Equations*, Siam, Philadelphia, 1985.

Myers, L. A., R. Roque, and B. Birgisson. Propagation Mechanisms for Surface-initiated Longitudinal Wheel Path Cracks. *In Transportation Research Record 1778*, TRB, National Research Council, Washington, D.C., 2001, pp. 113-122.

Park, S. W., Y. R. Kim, and R. A. Schapery. A Viscoelastic Continuum Damage Model and Its Application to Uniaxial Behavior of Asphalt Concrete. *Mechanics of Material*, 24, 1996, pp. 241-255.

Park, S. W., and R. A. Schapery. A Viscoelastic Constitutive Model for Particulate Composite with Growing Damage. *International Journal of Solids and Structures*, 34, 1997, pp. 931-947.

Park, S. W., and Y. R. Kim. Interconversion between Relaxation Modulus and Creep Compliance for Viscoelastic Solids. *Journal of Materials in Civil Engineering*, Vol. 11, No. 1, ASCE, 1999, pp. 70-82.

Park, S. W., and R. A. Schapery. Methods of Interconversion between Linear Viscoelastic Material Functions. Part 1 – A Numerical Method Based on Prony Series. *Int. J. Solids and Structures*, 36(11), 1999, pp 1653-1675.

Park, S. W., and Y. R. Kim. Fitting Prony-Series Viscoelastic Models with Power-Law Presmoothing. *Journal of Materials in Civil Engineering*, Vol. 13, No. 1, ASCE, 2001, pp. 26-32.

Poon, H., and M. F. Ahmad. A Material Point Time Integration Procedure for Anisotropic, Thermo Rheologically Simple, Viscoelastic Solids. *Computational Mechanics*, 21, 1998, pp. 236-242.

Raad, L., and J. L. Figueroa. Load Response of Transportation Support Systems. *Transportation Engineer Journal*, Vol. 106, No. 1, 1980, pp. 111-128.

Ramkumar, D. H. S., J. M. Caruthers, H. Mavridis, and R. Shroff. Computation of the Linear Viscoelastic Relaxation Spectrum from Experimental Data. *J. Appl. Polymer Sci*., 64, 1997, pp. 2177-2189.

Santha, B. L. Resilient Modulus of Subgrade Soils: Comparison of Two Constitiutive Equations. In *Transportation Research Board 1462*, TRB, National Research Council, Washington D.C., 1994, pp. 79-90.

Schapery, R. A. *A Simple Collocation Method for Fitting Viscoelastic Models to Experimental Data*. Report GALCIT SM 61-23A. California Institute of Technology, Pasadena, Calif., 1961.
Schapery, R.A. *Viscoelastic Behavior and Analysis of Composite Materials*. Chapter 4 in Composite Materials 2. (ed. Sendeckjy, G. P.), Academic Press, 1974.

Schapery, R. A. Correspondence Principles and a Generalized J Integral for Large Deformation and Fracture Analysis of Viscoelastic Media. *International Journal of Fracture*, 25, 1984, pp. 195-223.

Schapery, R. A. A Theory of Mechanical Behavior of Elastic Media with Growing Damage and Other Changes in Structure. *Journal of the Mechanics and Physics of Solids*, 38, 1990, pp. 215-253.

Schapery, R. A. Analysis of Damage Growth in Particulate Composites Using a Work Potential. *Composite Engineering*, 60, 1991, pp. 153-173.

Schapery, R. A., and S. W. Park. Methods of Interconversion between Linear Viscoelastic Material Functions. Part 2 – An Approximate Analytical Method. *Int. J. Solids and Structures*, 36(11), 1999, pp 1677-1699.

Sebaaly, P. E., and N. Tabatabaee. Influence of Vehicle Speed on Dynamic Loads and Pavement Response. In *Transportation Research Board 1410*, TRB, National Research Council, Washington D.C., 1993, pp. 107-114.

Siddharthan, R. V., N. Krishnamenon, M. El-Mously, and P. E. Sebaaly. Investigation of Tire Contact Stress Distributions on Pavement Response. *Journal of Transportation Engineering*, Vol. 128, No. 2, ASCE, 2002, pp. 136-144.

Simo, J. C., and T.J.R. Hughes. *Computational Inelasticity*. Springer-Verlag, New York, 1998.

Stewart, J. R., and T.J.R. Hughes. A tutorial in Elementary Finite Element Error Analysis: A Systematic Presentation of a Priori and a Posteriori Error Estimates. *Comput. Methods Appl. Mech. Engrg.* 158, 1-22, 1998.

Taylor, R. L., K. S. Pister, and G. L. Goudrequ. Thermomechanical Analysis of Viscoelastic Solids. *International Journal for Numerical Methods in Engineering*, 2, 1970, pp. 45-59.

Thompson, M. R., and R. P. Elliot. ILLI-PAVE-Based Response Algorithms for Design of Conventional Flexible Pavements. In *Transportation Research Board 1043*, TRB, National Research Council, Washington D.C., 1985, pp. 50-57.

Tschoegl, N.W., The Phenomenological Theory of Linear Viscoelastic Behavior. Springer, Berlin, 1989.

Tschoegl, N. W. Time Dependence in Material Properties: An Overview. *Mechanics of Time-Dependent Materials 1*, 1997, pp. 3-31.

Witczak M. W., and J. Uzan. *Universal Airport Pavement Design System*, *Report I of IV: Granular Material Characterization.* Department of Civil Engineering, University of Maryland, College Park, 1988.

Zienkiewicz, O., and J. Zhu. A Simple Error Estimator and Adaptive Procedure for Practical Engineering Analysis. *Int. J. Numer. Methods Eng*., 24, 1987, pp. 337-357.

Zienkiewicz, O., and J. Zhu. The Superconvergent Patch Recovery and a Posteriori Estimates. Part I: The Recovery Technique. *Int. J. Numer. Methods in Engrg.*, 33, 1992, pp. 1331-1364.

Zienkiewicz, O. C., and J. Z. Zhu. Superconvergence and the Superconvergent Patch Recovery. *Finite Elements in Analysis and Design*, 19, 1995, pp. 11-23.

Zocher, M. A., S. E. Groves, and D. H. Allen. A Three-Dimensional Finite Element Formulation for Thermoviscoelastic Orthotropic Media. *International Journal for Numerical Methods in Engineering*, 40, 1997, pp. 2267-2288.